Fluorogenic DNA Probes for Single-Molecule Fluorescence Imaging *in vitro* and *in vivo*

Mirjam Kümmerlin

Balliol College

University of Oxford

A thesis submitted for the degree of

Doctor of Philosophy

Trinity 2024

Science is Magic that works

—a helpful soul in the castle in the roundabout—

Abstract

The "high concentration barrier", describing the maximum concentration of fluorescent species tolerable, is one of the main limitations of single-molecule fluorescence (SMF) measurements. Addressing this fundamental limit can enable and expand several *in vitro* and *in vivo* single-molecule applications, including tracking in crowded environments, fast super-resolution imaging, and single-molecule fluorescence resonance energy transfer (smFRET) experiments.

In this thesis, we develop fluorogenic probes (which become fluorescent upon binding to a target) to address the high-concentration barrier in several SMF applications. The design is based on short ssDNAs fluorescing only upon hybridising to their complementary target sequence. We engineer the quenching efficiency and fluorescence enhancement upon duplex formation through screening several fluorophore-quencher combinations, label lengths, and sequence motifs, which serve as tuning screws to adopt our labels to different experimental designs. With these fluorogenic labels, we can perform SMF experiments at concentrations in excess of 10 µM fluorescent labels – an improvement of two orders of magnitude compared to standard TIRF experiments, without the need for any special optics or nano-fabrication.

We present several experimental applications of our probes, each showcasing a specific feature fluorogenic probes can provide: We demonstrate the ease of implementing these probes into existing protocols by performing super-resolution imaging with DNA-PAINT, employing a fluorogenic 6nt-long imager. Importantly, we did not perform any sequence engineering ourselves, but simply "plugged in" the fluorogenicity feature and reduced the imager length. Through the faster acquisition rate of binding events, the imaging of viral genome segments could be sped up significantly, now only requiring approx. 150 s of imaging to extract physical features in the 20 nm range.

To highlight new experimental paths only possible with fluorogenic labelling species, we performed smFRET measurements where photobleaching is circumvented through a constant exchange of donor- and acceptor- dyes, supplied by fluorogenic ssDNAs (REFRESH-FRET). This process is facilitated by fast the exchange kinetics at probe concentrations far exceeding 100 nM, and allows for observation of smFRET for hours.

Thirdly, we applied our probes in live-cell tracking of individual ribosomes by labelling their 16S rRNA with a complementary probe. The increased signal-specificity that fluorogenicity provides allows for a great signal-to-noise ratio within the cellular environment. Our probes directly hybridise to the rRNA target, so do not require any genetic engineering.

In summary, we characterised the fluorogenic properties of dye-quencher labelled ssDNA probes, and demonstrate several single-molecule applications *in vitro* and *in vivo*. Through their tuneability and simple implementation, we envision our probes to be widely applicable, beyond what we could demonstrate here.

Acknowledgements

Institutional

None of the work in this thesis would have been possible without the following institutions supporting this endeavour:

- EPSRC for covering my tuition fees.
- The Boehringer Ingelheim Fonds for awarding me one of their Doctoral Fellowships - in particular to Dr. Jan Kullmann for cheering me on even before either of us knew whether the interview was a success.
- The Kavli Institute for providing a cheerful, productive and friendly environment, especially after the dreadful years of the pandemic.

Personal

When writing these lines, the major block of this work is done, the thesis has been written (at least once), and I feel like I am on the final stretch of this PhD. Time to reflect on all the wonderful people, who were part of this journey:

My first big 'Thank you!' goes to Achilles, who over all these years and through the pandemic was a great supervisor and mentor. The great freedom you gave me in this PhD was intimidating at first, has remained challenging throughout, but turned out to be the greatest gift about it. Thanks for keeping an eye on the human aspects of the sometimes all too big scientific apparatus - (lab) life is all the better for it.

It takes a village to raise a child and at least one great lab to make a PhD - and so it needed the wonderful bunch of people that is and was the Kapanidis Lab to get to this stage. Thank you to Ed, Rasched, Andrew, Anna, Jacob, and Oli for being part of it. Thank you also to all those who taught me a great deal of scientific skills along the way, you all are part of the achievements of this thesis in one way or another: There would be no FRET analysis without Abhishek, no live-cell experiments without Hafez, no analysed data without Piers, no painted viruses without Christof, no micromolar assay without Jagadish, no hour-long time trace without Stelios.

I was very lucky to also share my time in this lab with some wonderful women: Qing was invaluable to the DNA-PAINT data analysis, Alison was key to envisioning the ribosome tracking project, Emma helped a great deal with my *in*

vivo experience, and Sammi - despite only very recently joining us - has already made my lab day so much more colourful. Aida - without your visit, we might have never seen the solution to the main issue of the project. Thanks to all of you for being such strong, inspiring women in science!

There is one more woman I want to mention: You are guiding me as a great example of how enthusiasm, empathy, and a brilliant mind can navigate this academic world - as a woman who is not giving up on her values, and who is not ready to sacrifice herself to the sometimes very shallow measures of success academia can offer. When I look at this thesis, I see so much of you in it - what I learned from working with you in Munich (and beyond) is deeply woven into it. Thanks, Viki for everything - you are a wonderful friend and I wish you all the best for the journey ahead!

Speaking of friends: Thanks to the Catlovers, who are (not only!) academically inspiring, sometimes challenging, but always there for everyone with lots of love, laughter, support, and energy for fun activities.

Cindy - It's amazing how we did the last 10 years side by side. Taking different paths here and there, but what started with our first ever lab project has now led to PhDs that would be overlapping were they any closer. It's time for that joint paper!

Ali - Everyone (especially living in the UK) needs a second sun that they can rely on brightening up their day when the world wouldn't do it. Thanks for being that to me!

And then there is the vegane Hippie-WG, turned Bademantelgang: We are definitely all total versch(r)oben, but incredibly good at that. Lisa, Julia, Michi, Matthias, Toni, Tobi, and Jenny, thanks for being such a wonderful bunch - you made the castle in the roundabout a home. Jenny and Tobi, our UK journey began a long time ago - and as always, you have been the best travel companions!

And I couldn't finish off without thanking Mr Beißer of the Stiftung Maximilianeum. I wouldn't be where I am today without the Stiftung: It truly were the most worry-free years I could have hoped for. More than that, I met many true friends, got to grow into and beyond myself and was given incredible opportunities, that ultimately were the reason I first came to Oxford.

The reason I came back and stayed was you, James. I love you.

Contents

Statement of Authorship

I hereby declare that I have performed the work in this thesis alone, except where indicated in the text, and as described below. The use of the pronoun "we" in the following is an expression of the collaborative nature of all scientific work.

- The analysis pipeline of DNA-PAINT data in chapter 3 was developed by Qing Zhao in discussion with myself and Dr. Christof Hepp. Qing performed the final analysis, all graphs were plotted and interpreted by myself. Qing also provided the description of the analysis in the Appendix.
- The experiments in fixed cells presented in section 5.3.1 were performed and analysed by Alison Farrar. All graphs were plotted and interpreted by myself.
- Electro-competent cells used in chapter 5 were prepared in part by Dr. Hafez El Sayyed, Edward Wheeler, and me.
- All manuscripts published from this work were contributed to by the listed co-authors, as outlined in the published statement of contributions. Achillefs Kapanidis read and edited all manuscripts.

Presentations

- **Talk**: Boehringer Ingelheim Fonds North America Meeting, 2021, online.
- **Poster**: Hour-long single molecule fluorescence and FRET - a new tool for structural dynamics and reaction kinetics, UK RNA Polymerase Workshop, 2022, Newcastle, UK.
- **Poster and Talk**: REFRESH - Bleaching free sm fluorescence and FRET, PicoQuant Single Molecule Workshop, 2022, Berlin, Germany.
- **Talk**: REFRESH - Bleaching free sm fluorescence and FRET, Biophysics Seminar, 2022, Oxford, UK.
- **Talk & Student Scholarship**: REFRESH - Bleaching free sm fluorescence and FRET, European Workshop on Advanced Concepts in Fluorescence Imaging and Spectroscopy Techniques, 2022, Munich, Germany.
- **Poster**: Overcoming the High-Concentration-Barrier in Single-Molecule Fluorescence through Adaptable Fluorogenic ssDNA Labels, EBSA Meeting, 2023, Stockholm, Sweden.
- **Invited Talk**: REFRESH - Bleaching free single-molecule fluorescence and FRET, Micrographia Bio, 2023, London, UK.
- **Talk**: Breaking the Concentration Barrier in Single-Molecule Fluorescence with Fluorogenic Probes- a Universal Approach, Biophysics Seminar, 2024, Oxford, UK.
- **Talk**: Breaking the Concentration Barrier in Single-Molecule Fluorescence with Fluorogenic Probes- a Universal Approach, Nucleic Acids Group Forum, 2024, London, UK.
- **Talk**: Probing cellular processes on a single-molecule level with fluorogenic ssDNAs, Boehringer Ingelheim Fonds Summer Seminar, 2024, Hirschegg, Austria.

Publications

- **Bleaching-resistant, Near-continuous Single-molecule Fluorescence and FRET Based on Fluorogenic and Transient DNA Binding**, M. Kümmerlin, A. Mazumder, A. N. Kapanidis, ChemPhysChem 2023, 24, e202300175. This publication was selected for a cover feature.
- **Tunable fluorogenic DNA probes drive fast and high-resolution single-molecule fluorescence imaging**, Mirjam Kümmerlin, Qing Zhao, Jagadish Hazra, Christof Hepp, Alison Farrar, Piers Turner, Achillefs N. Kapanidis, bioRxiv 2025.01.21.634148.
- **DNA nanosensors: How to unlock the full potential of DNA nanotechnology for biosensing?**, Manuscript in preparation, S. Driesen, K. Leirs, C. Van Leemput, M. Kümmerlin, A.N. Kapanidis, C. Pinheiro, A. Hendrix, J. Lammertyn
- **Single-molecule imaging for unravelling the functional diversity of 10-13 DNAzymes**, Manuscript in submission, A. Montserrat Pagès, M. Kümmerlin, R. Andrews, A. N. Kapanidis, D. Spasic, J. Lammertyn

1

Introduction

Contents

1.1 Revolutionising science molecule by molecule

The understanding of structure, dynamics, and function of biological systems has been transformed by the unique insights gathered from single-molecule experiments both *in vitro* and *in vivo*.[1]

In the traditional ensemble measurements used for decades (e.g. fluorometry, any form of gel electrophoresis analysis, or general fluorescence imaging of cells), critical information about different structural and functional subpopulations in a complex milieu of molecules is lost due to ensemble averaging (as illustrated in Figure 1.1A by averaging the colour averaging of different molecules). In addition to this population averaging, there is temporal averaging as most processes do not occur and cannot be synchronised on a molecular level to the extent required to study molecular processes (see illustration in Figure 1.1B), this is specifically true for systems in thermodynamic equilibrium. The timing of observations offered by single-molecule techniques, however, allows for the identification of individual steps, and, most importantly, the sequence and kinetics of each step in a specific process can be identified and analysed separately for individual molecules.

The emergence of single-molecule techniques in the late 1990s led to an avalanche of new single-molecule studies on assembly and folding of proteins, mechanism of protein function, structure-function relationships of molecular assemblies, and coupling of large macromolecular machines *in vitro* and *in vivo*.

Their versatility and sensitivity have made especially single-molecule fluorescence (SMF) spectroscopy and microscopy studies very popular, specifically when compatibility with living cells is required.[2,3] The detection of a fluorescing molecule, its emission properties, and its precise location enable measurements of molecular stoichiometries, as well as super-resolution imaging and single-molecule tracking.[4–10]

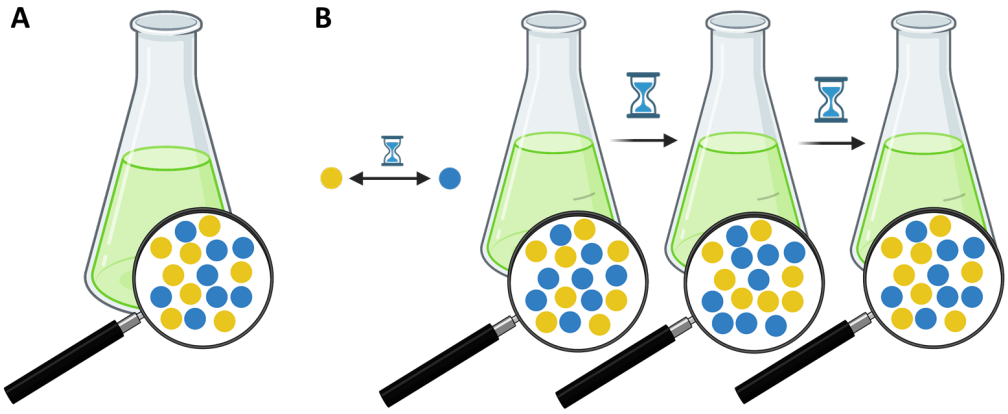

Figure 1.1: The principle of single-molecule experiments. A: An ensemble observation of the molecular property "colour" would report "green", not resolving the different populations of yellow and blue molecules, and in the complete absence of any green molecules. B: An ensemble observation of a process in equilibrium would not report a colour change upon molecules switching colours from yellow to blue or vice versa. Observations on the single-molecule level can observe the individual molecules transitioning and can report on kinetics of the process.

All SMF techniques rely on the specific detection of (most commonly) individual fluorophores, which operate as reporters for the target molecule. These exhibit certain characteristic phenomena, which are both used to select true single-molecule signals (but at the same time present challenges when interpreting data): Firstly, photobleaching (the permanent destruction of the chromophore due to photochemical processes and reactions) occurs as a discrete process, with one bleaching step per fluorophore. Secondly, photo-blinking i.e. oscillations in emission intensity can be observed due to molecules switching into different emission states (unless prevented by specific buffer compositions). Thirdly, anti-bunching, i.e. a delay between the emission of two photons (as detectable in the autocorrelation function), can only be observed for single emitters, which require a discrete time to cycle another electron into the excited state and de-excite *via* fluorescence emission of another photon. These specific properties - single-step photo-bleaching, blinking, and anti-bunching - are lost when many fluorophores are observed at the same time.

There are several single-molecule techniques or aspects of these worth a brief introduction, the following is by no means intended to be a complete list. Some techniques will be discussed more thoroughly in the following chapters, where appropriate.

SMF has enabled super-resolution microscopy (SRM) by leveraging the ability to detect and localise single molecules with great precision. Conventional microscopy is limited by diffraction, which does not allow the spatial separation of two emitters spaced by less than $\approx$ 250 nm (for visible light microscopy, Figure 1.2B). Many molecular interactions occur at scales much below the diffraction limit, as are the structures of viruses or proteins, which can thus not be resolved from diffraction-limited images acquired using conventional microscopy. By imaging a subset of all emitters in single images, which later become super-imposed to reconstruct the complete image, SMF localisation microscopy techniques like photo-activated localisation microscopy (PALM), stochastic optical reconstruction microscopy (STORM), and DNA-points accumulation for imaging in nanoscale topography (PAINT) achieve resolutions well below the diffraction limit (Figure 1.2).[7,11–13] Using localisation-based SRM has provided significant insight into fundamental cellular processes, and it has found its place amongst the tools commonly employed to assess dynamics and spatial distributions of proteins and nucleic acids in cells, as well as in nanoscale structures (e.g., viruses or the cytoskeleton).[14,15] A specific introduction to DNA-PAINT microscopy will be given in chapter 3.

For the single-molecule localisation microscopy (SMLM) methods, target molecules have to be immobilised, since the imaging process requires time. However, individual fluorescent molecules can also be observed when diffusing, where their path ("track") and diffusion speed can be subsequently analysed to give further insight into e.g. the processes the target molecule is involved in, the

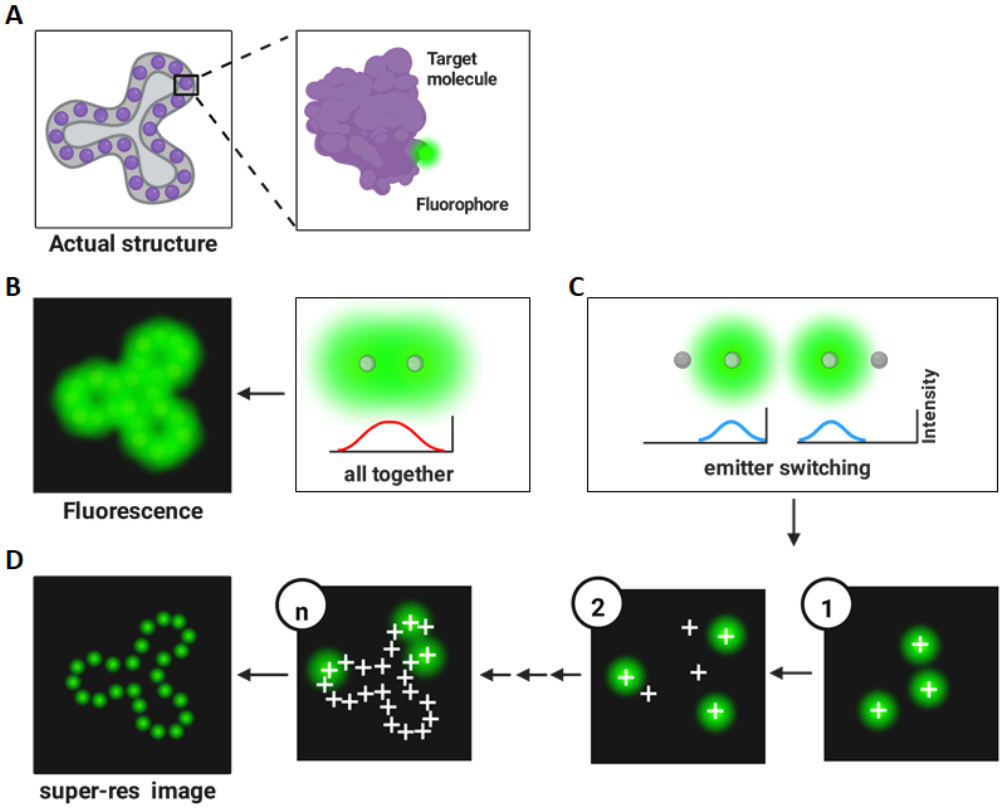

Figure 1.2: The principle of single-molecule localisation microscopy. A: The target structure, formed by several units of a particular target molecule which is labelled with an emitter. B: If distances between the different emitters are below the diffraction limit, they cannot be resolved individually with conventional light microscopy. C: Temporal separation of the emitters by selectively activating only a subset of them allows localising each one with great precision. D: In subsequent frames, different sets of emitters get activated and their position localised. Reconstruction images of all accumulated localisations reveal the target structure, as in panel A.

composition of the environment, or subcellular organisation patterns. Due to the great precision which is achievable when localising individual fluorophores, this can resolve movements well below the diffraction limit. These ideas form the basis for the study of ribosomes in chapter 5.

One further methods allows collecting spatial information on an even smaller scale: single-molecule fluorescence resonance energy transfer (smFRET) , can be used as a molecular ruler, sensitive to distances in the 2-10 nm range. Studies

involving smFRET monitor the kinetics of processes such as conformational changes or relative movements of two interacting species and have been widely employed in elucidating sequences of events of important biological processes, such as transcription, translation, and protein folding.[16] A more detailed theoretical introduction to FRET is given in section 1.4.1 of this chapter.

1.2 The concentration barrier in SMF

In many SMF experiments, a critical limitation known as the "high concentration barrier" prevents single-molecule analysis when the concentration of fluorescent species exceeds a certain concentration (1-10 nM in general wide-field microscopy, 100 nM for total internal reflection (TIRF) microscopy, and much lower for solution-based confocal microscopy).[17–19] At higher concentrations of fluorescent molecules, the signal-to-noise ratio (SNR) deteriorates too much to allow reliable analysis of the data (see Figure 1.3, Note: These images were acquired in TIRF mode, so observations are possible up to about 100 nM. The phenomena of SNR deterioration is comparable across techniques, though.). This limitation introduces the need to remove any unbound or non-specifically bound fluorophores (e.g. in immuno-histochemistry- or Halo-Tag-based labelling approaches) and to limit experimental designs with correctly labelled species to relatively low concentrations, which are often far below biologically relevant affinities.[18,19]

Strategies to address the "concentration barrier" have focused both on limiting the excitation of or the emission from (unbound or otherwise diffusing) fluorescent molecules in the background, and on enhancing the fluorescence of molecules involved in the process or bound to the structures of interest. Background suppression can be achieved by suitably modified instruments, such as in zero-mode-waveguides or using the evanescent excitation field in a TIRF microscope. In stimulated emission depletion (STED) microscopy, a second laser inducing

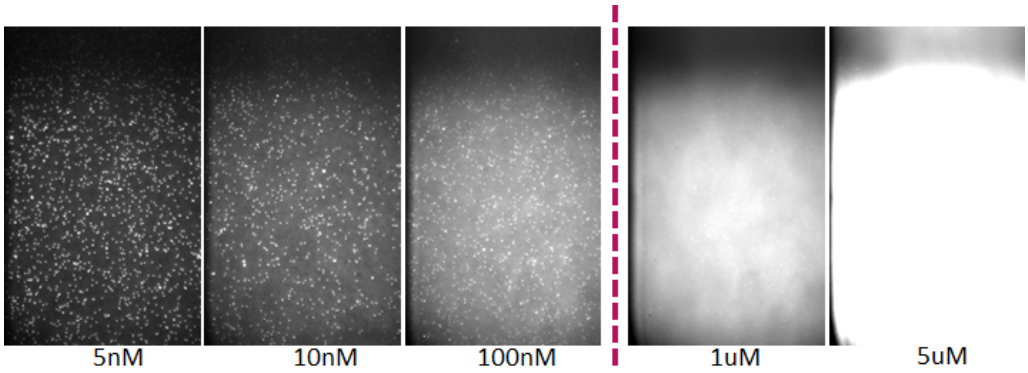

Figure 1.3: The single-molecule concentration barrier in TIRF experiments. Individual, labelled ssDNA molecules hybridising to complementary ssDNA molecules on the surface can be resolved and observed on these field of views (FOVs) up until a concentration of approx. 100 nM. For higher concentrations, the background fluorescence by unbound molecules deteriorates the SNR too far to allow for detection of the individual molecule on the surface.

stimulated-emission depletion reduces the *de facto* excited volume. The standard for surface-based SMF experiments, the TIRF microscope, however, still cannot allow detection of single immobilised molecules in the presence of >100 nM of fluorescent species (Figure 1.3).[18,20–22]

Fluorescent enhancement of only those molecules which are under observation using plasmonic effects can improve the SNR of a measurement by several orders of magnitude,[23] but require the experimental protocol to be compatible with the stability, accessibility, and functionality offered by the specific nanostructure employed in the experiment. As such, nanostructures facilitating plasmonic enhancement are so far unsuitable for imaging or tracking experiments.

A third approach focuses on using fluorogenic molecules which exhibit a significant increase in quantum yield/fluorescence brightness upon interacting with their target structure. Examples of this include fluorogenic dyes (e.g. nile red in PAINT microscopy[24]) or molecular structures in which a conformational change upon binding displaces a quencher to recover fluorescence of a fluorophore. In contrast to other approaches, the employment of these fluorogenic labels or

components does not require any specialised optics or nanofabrication, but is compatible with either.[25]

In particular, DNAs have a long-standing history of being used as fluorogenic sensors. A main focus of the development has been on polymerase chain reaction (PCR) probes, allowing detection and quantification of PCR products without further post-processing:[26,27] In early days, the read-out relied on either nuclease digest of a ssDNA to remove a quencher from the proximity of a fluorophore or to free the fluorophore into solution.[26–28]

Fluorogenicity upon hybridisation of these single-stranded DNAs (ssDNAs) was first used in molecular beacons, which use a self-complementary stem region to facilitate interactions between terminally attached fluorophore and quencher.[28,29] Later on, this secondary structure was found not to be required for fluorogenicity of ssDNAs.[30] The quenchers utilised have been diverse (both fluorescent and dark quenchers), further the quenching abilities of DNA bases themselves and of metal nanoparticles have been utilised.[26–28,30–32]

The quenching process in certain short, doubly-labelled ssDNAs (with dye and quencher) was characterised to contain FRET-quenching and contact-quenching components, which both show different spectral and molecular dependencies.[30,33,34] Many studies, in particularly in the context of PCR probe development, primarily focused on generating high quenching efficiencies in these constructs, but paid little attention to the brightness of the de-quenched construct after hybridisation (or at least did not explicitly analyse it). Yet, when translating the concept from ensemble into the single-molecule setting, the de-quenched state is particularly important, since a single emitter has to be bright enough to be detected and/or localised.

In an early SMF example, Zhang *et al.* used 19 nt long ssDNA probes, labelled with dye and quencher, which hybridised to complementary mRNA. The fluorogenicity allowed for high operational concentrations for fast hybridisation of the probes to freshly synthesised mRNA.[35] The 19 nt length arouse from considerations of sequence specificity and hybridisation rates, but also allowed for good fluorogenicity, in particular high emission levels upon hybridisation.

The deployment of fluorogenic probes in localisation-based super-resolution microscopy has been a particular inspiration for the work in this thesis, highlighting some of the key challenges the field faced when developing well-performing, fluorogenic SMF probes, in particular where short sequences are required. A more in-depth review of the particular publications is given in chapter 3, but the following developments in DNA-PAINT microscopy illustrate the extensive effort that experimental designs require in the absence of a general and easily adoptable strategy to implement fluorogenicity into SMF assays:

Based on the assumption (and observation) that a certain minimum distance was required for efficient de-quenching (around 6 nm), fluorogenic imagers were first introduced to DNA-PAINT microscopy using two optimised 15 nt imager sequences with internal mismatches (which had to be carefully engineered).[36] The mismatches reduced the duplex stability and in combination with a higher imager concentration allowed for faster imager turnover - and an overall faster imaging process.

FLASH-PAINT later addressed the multiplexing limitations of this approach by implementing removable adapter strands to selectively activate and deactivate docking sites, allowing the re-use of imagers for different targets.[37]

Another approach by Kessler *et al.* utilised self-quenching of two terminal ATTO655 dyes for fluorogenicity, but this approach is spectrally limited and has

a lower enhancement compared to dye-quencher combinations we will discuss in this thesis.[38] While these strategies all successfully employ fluorogenic imagers and improve DNA-PAINT acquisition speed, the solutions they provide are either very specialised (ATTO655 self-quenching) or require significant engineering of experimental protocols, highlighting the necessity for a more universally adoptable strategy to implement fluorogenicity in SMF.

1.3 Objectives of this thesis

Here, we present a universally translatable strategy for the design of fluorogenic ssDNA-based probes based on terminal labelling with fluorophore and quencher, which can be employed in a wide range of experimental set-ups to label and visualise biological processes and structures at high operational concentrations. We specifically focus on the compatibility with SMF experiments, the ease of implementation into existing technologies, and the doors that higher concentrations can open into so far unexplored experimental domains.

This chapter gives an overview of the main theoretical considerations in the quenching and de-quenching process. Further information on the specific background to each application is given in the relevant chapters to allow for a more coherent and comfortable read.

Chapter two provides a careful characterisation of the probe design and the effects of the main parameters in the design of such probes (fluorophore-quencher pairing, probe length, and sequence effects). We can in particular address previous limitations for short probes (5-15 nt) and demonstrate a SMF assay using the newly designed probes at micromolar concentrations.

Chapter three focuses on the "plug and play" character of our fluorogenic probes by adding fluorogenicity into existing experimental protocols, which we demonstrate in DNA-PAINT imaging using a 6nt fluorogenic imager. The shorter interaction of this 6nt imager used at high concentrations allows for a much faster data acquisition and can speed up the otherwise lengthy DNA-PAINT imaging process substantially.

In chapter four, fluorogenic probes are used to facilitate a completely new experimental approach to overcome photobleaching: Through a constant exchange of the fluorescent "unit", individual molecules of interest can be studied over

pre-longed time spans. The kinetics of this exchange need to be fast, which is facilitated by very high operational concentrations of fluorogenic probes.

Chapter five introduces an additional characteristic of fluorogenic probes and explores their use in *in vivo* settings: The fluorogenic property allows generating very specific signals in settings where imaging or tracking would usually require the removal of unbound probes. We explore the performance of fluorogenic probes targeting the ribosome inside live *E. coli* cells, particularly focusing on characterising uptake, signal specificity and probe stability inside the considerably more crowded and heterogeneous environment that is a living cell.

Chapter six summarises the main developments and findings of this thesis, putting them into context with one another. This is concluded with a brief outlook onto possible further expansions of the techniques presented here is given, focusing mainly on labelling proteins or mRNA both *in vitro* and *in vivo*.

1.4 Theoretical background

1.4.1 Förster resonance energy transfer

FRET is the process of a radiation-less transfer of energy between two molecules *via* dipole-dipole interactions and was first discovered in polarisation measurements of dye solutions: Upon shining polarised light into a sufficiently concentrated dye solution, internal transfer processes would reduce polarisation of emitted photons with rising dye concentration.[39,40] First explanations interpreted the effect as a secondary fluorescence process after absorption of the primary fluorescence photon. They were, however, not consistent with the experimentally obtained concentration dependence. T. Förster was the first to give a quantum mechanical theory to describe these processes accurately as an energy transfer between an excited dye molecule (donor) and a not yet excited molecule (acceptor) *via* dipole-dipole interactions.[41] This process does not involve the exchange of a particle *i.e.* a photon and relies on two quasi-simultaneous processes: The energy transfer from donor to acceptor molecule and the emission of the transferred energy from the acceptor molecule *via* fluorescence.

The energy transfer can not only be observed in a highly concentrated dye solution, but also between two different dyes - providing that the emission spectrum of one dye (donor) overlaps sufficiently with the absorption spectrum of the second dye (acceptor) and both dye molecules can be found in close proximity (commonly $\sim$ 2-10 nm). Additionally, their dipole moments must share a parallel component to allow for coupling. What was first discovered in homogeneous solutions of only one fluorophore, is nowadays a widely used technique to study biological systems and resolve distances far below the diffraction limit. In the context of this thesis, it is important to mention that the acceptor dye does not need to be fluorescent, many dark quenchers serve as FRET-acceptors and de-excite in the far red or infra-red.

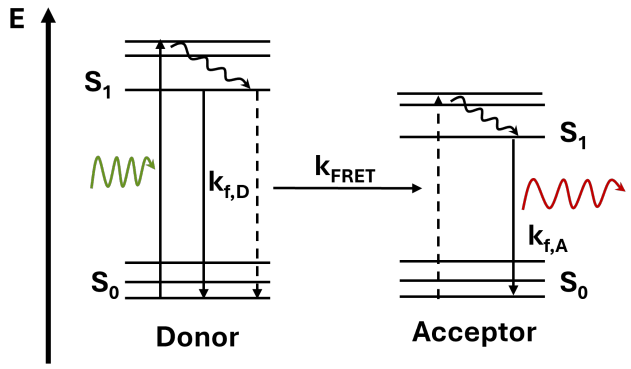

Figure 1.4: Jablonski-diagram of the FRET process. Upon donor excitation, which is followed by internal conversion processes, the energy is non-radiatively transferred to excite the acceptor molecule. The acceptor can emit a fluorescence photon or remain dark and dissipate the energy in heat, as is common for many dark quenchers.

Upon exciting the donor, several competing processes take place (see Figure 1.4): There is direct fluorescence emission, but also various non-radiative transitions, including transitions to triplet states and quenching in chemical reactions (the latter have been omitted in the figure for clarity). Providing above conditions (spectral overlap, distance, parallel dipole component) for FRET are fulfilled, there is also the possibility of direct energy transfer to a second dye molecule. This, in turn, can now de-excite *via* any of the above-mentioned pathways.

The proportion of FRET emission among the total amount of processes leading to the relaxation of the donor, called the FRET efficiency E_{FRET}, can be expressed by the following equation 1.1 relating the rates at which the different processes occur:

$$E_{FRET} = \frac{k_{FRET}}{k_{FRET} + k_F + k_{NR}} \tag{1.1}$$

k_{FRET} is the rate of FRET, k_F the rate of fluorescence and k_{NR} sums up the rates of all other possible, non-radiative relaxation pathways. The energy transfer rate from the donor to the acceptor k_{FRET} in dependence of the intermolecular distance r can be given by:[42]

$$k_{FRET}(r) = \frac{9000\ ln(10)\kappa^2\Phi_D}{128\pi^5 N_A r^6 \tau_D} \int_0^\infty \frac{F_D(\nu)\epsilon_A(\nu)}{\nu^4} d\nu \tag{1.2}$$

where κ is an orientation factor, Φ_D is the donor quantum yield, N_A is Avogadro's constant, r is the distance between both dye molecules, τ_D is the donor fluorescence lifetime, $F_D(\nu)$ represents the normalised donor emission spectrum, and $\epsilon_A(\nu)$ is the molar extinction coefficient of the acceptor at frequency ν. This formula unites information about the spectral overlap of donor emission and acceptor absorption spectrum (the overlap integral), the relative dipole moment orientation of both molecules (κ), and the donor quantum yield which are all assumed to be constant and known for a specific dye pair.* These constants are summarised as the so-called Förster-radius R_0, at which a transfer efficiency of 0.5 is observed, so equation 1.2 can be simplified to:

$$k_{FRET}(r) = \frac{1}{\tau_D}(\frac{R_0}{r})^6 \tag{1.3}$$

E_{FRET} can then also be written as:

$$E_{FRET} = \frac{R_0^6}{R_0^6 + r^6} \tag{1.4}$$

This, in theory, provides an easy way to determine the distance between donor and acceptor (r) by measuring E_{FRET}, providing R_0 is known in the given setting. As values of R_0 typically lie within the low nano-meter range, the method is sensitive to distances in the range between 2 - 10 nm, which cannot be resolved using conventional microscopy techniques.[44] Varying R_0 of the FRET-pairs allows tuning the distance range over which FRET is a sensitive sensor, a fact we have exploited to tune the properties of our fluorogenic labels.

*Whether κ^2 can be averaged and seen as constant is still subject to discussions. A constant κ^2 is often assumed because of molecule rotation times are thought to be much quicker than fluorescence lifetimes, so that all orientations are covered within the lifetime of the excited state. Averaging over time then yields $\kappa = \frac{2}{3}$. This assumption is, however, not true for all cases and needs adjustment for specific situations. A recent benchmark study confirmed the accuracy of absolute distance measurements for freely rotating dyes on DNA, however steric constraints might interfere with the measurement.[43]

1.4.2 Fluorescence quenching

Quenching describes a process or an interaction between a fluorophore and another molecule (a quencher) which results in a reduced fluorescence emission. The quencher can be the same type of molecule as the fluorophore (sometimes referred to as self-quenching e.g. in Kessler *et al.*[38]), or it can be a different molecule altogether (fluorescent or not). Mechanistically there are two broad classes of quenching processes: So-called static quenching occurs due to interactions of the fluorophore and quenching molecule(s) in the ground state, resulting in a ground-state complex which can no longer be excited (or only with significantly altered excitation parameters). The second type, dynamic quenching, occurs by interaction of the fluorophore in the excited state with surrounding molecules, which prevent fluorescence emission. Both types will be briefly discussed in the following.

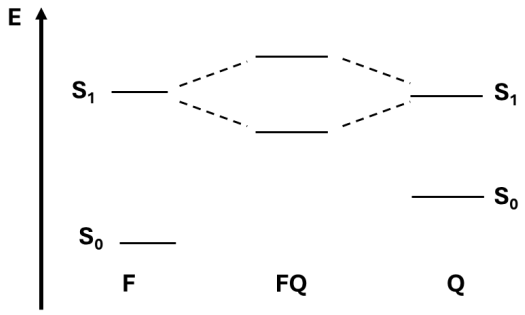

Figure 1.5: Jablonski-diagram of the contact-quenching interactions. In the ground state, two molecules found a complex with altered energy levels, which can no longer be excited as efficiently by the original excitation light.

Firstly, static quenching describes an encounter of two molecules (at least one of them is the fluorophore of interest), which undergo complex formation in such a way that energy levels of the new complex differ significantly from those of the original fluorophore (Figure 1.5). In the case of homo-dimer formation (or between different molecules of very similar energy levels), the molecular orbitals formed from the S_1 states are split into levels higher and lower than the original S_1 energy levels.[45] The effect is strongest the closer the original energy levels were, for spectrally very distant molecules it eventually becomes negligible.[46,47]

These changes, as an immediate consequence, reduce the extinction coefficient of the complex to the wavelength which would be best absorbed by the uncomplexed fluorophore and results in a changed absorption spectrum.[48] The transition dipole arrangement now decides which excitation transitions are quantum-mechanically allowed (and therefore occur readily). Quenching occurs primarily when this new set of states are such that, after excitation and internal conversion processes, only triplet transitions to long-lived states are allowed and only very red-shifted phosphorescence can be observed, if at all. This is, in the context of the work here, especially observed upon stacking of planar aromatic molecules.[47] Residual fluorescence thus occurs primarily from uncomplexed fluorophore molecules at the standard fluorescence lifetime of fluorophore (since the excited state of those un-complexed molecules is unaffected).[47] In addition to the spectral/energetic conditions, molecular contact is required for these ground-state complexes to occur.

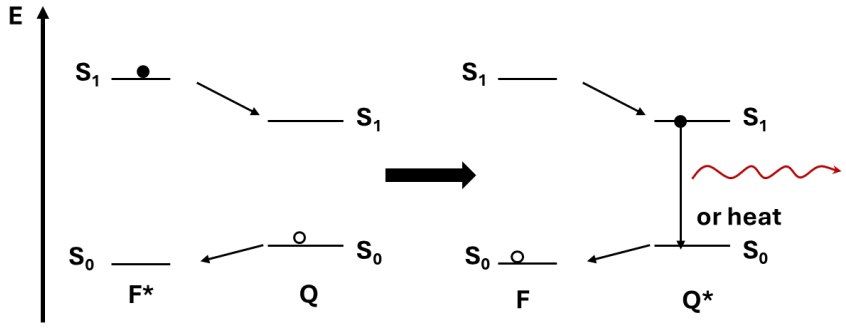

Figure 1.6: Jablonski-diagram of the electron exchange process (Dexter energy transfer). The excited electron in the F* (solid circle) is transferred onto a quencher molecule and, either simultaneously or subsequently, an electron (hollow circle) is transferred from the quencher back to the fluorophore. The Q* molecule created will relax in subsequent steps, often dissipating heat.

Dynamic quenching processes involve interactions of the excited state fluorophore molecule (F*) with the quenching molecule. For the purpose of this overview here, we will summarise also resonance energy transfer processes such as FRET

into this category (because they originate from F*), although the literature does not agree on whether it should be included in the same category.[47,49]

In general, there are several mechanisms which all lead to fluorescence quenching of an already excited F*: Firstly there are so-called collisional processes, where a diffusing molecule comes into molecular contact with F* and undergoes a reaction which results in depopulating the F* state without fluorescence emission. This can happen by various processes, one of which is electron exchange processes (Dexter energy transfer, Figure 1.6), often observed in solvent interactions (as very high concentrations are required).[48–50]

A second de-excitation process involves the photo-induced transfer of electrons (PET, i.e. redox reactions) between F* and quencher, resulting in two ionic radicals, which can then be subject to further redox reactions, either restoring the ground state fluorophore or resulting in a permanently altered molecule, one mechanism of photo-bleaching (Figure 1.7, see chapter 4 for more details on photobleaching).

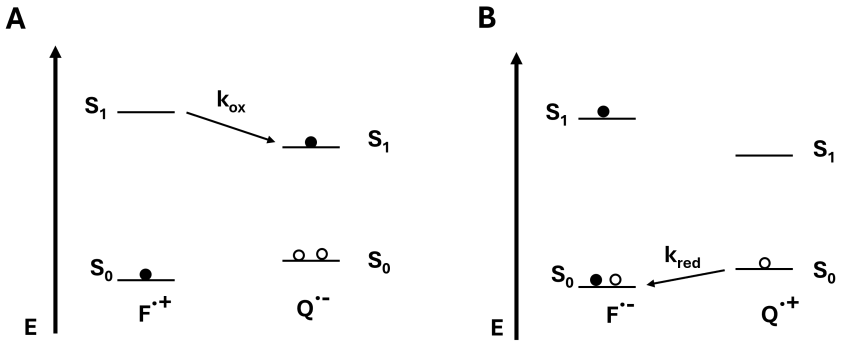

Figure 1.7: Jablonski-diagram of the photo-induced electron transfer (PET) process. Depending on the redox potentials, F* partake in oxidative (A) or reductive (B) reactions, yielding charged radicals. A: The oxidative transfer of an electron (solid circle) from the excited F* onto a Q molecule. B: The reduction of the excited molecule by electron transfer from the Q molecule (hollow circle). Further reactions are required to restore the original F (in S_0).

Thirdly, inter-system crossing (ISC) into the triplet state, as often caused in interactions with molecular Oxygen (Figure 1.8). The triplet state then is depopulated *via* one or several of the mechanisms already described: It emits either in a slow and red-shifted phosphorescence process (the transition is spin-forbidden), relaxes *via* further redox reactions (see PET, the molecule can get destroyed in the process) or electron exchange.[49]

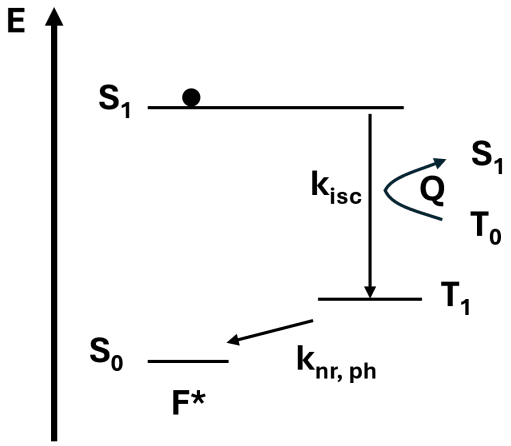

Figure 1.8: Jablonski-diagram of the quenching process *via* ISC. F* undergoes ISC in reaction with Q, which leaves it in a triplet state T_1. Relaxation from T_1 is only possible *via* slow phosphorescence or non-radiative processes. nr: non-radiative, ph: phosphorescence

Lastly, there are the non-collisional interactions occurring, e.g. during FRET processes (see previous section), during which only the excited state energy is transferred onto the quencher (or in this context more often called acceptor). FRET processes can occur over much larger ranges than the collisional mechanisms outlined above (1Å vs. 10s of Å), since FRET does not require orbital contact.[49] Dynamic quenching processes do not alter the absorption spectrum, but change the excited state lifetime, and so will result in a changed fluorescence lifetime measurement.

In the context of the labelled DNA probes in this thesis, we did not perform a detailed analysis of the precise quenching mechanisms at play within the constructs. Due to the distances in the hybridised state, only FRET quenching can and will occur once the probe is bound to a target. In the ssDNA state, we cannot exclude contributions from other quenching mechanisms, particularly for

the red construct in chapter 4 we strongly assume static quenching effects are at play.

2

Tuning fluorogenicity in ssDNA probes for SMF experiments

Contents

The work presented in this chapter is part of the preprint:

Tunable fluorogenic DNA probes drive fast and high-resolution single-molecule fluorescence imaging, Mirjam Kümmerlin, Qing Zhao, Jagadish Hazra, Christof Hepp, Alison Farrar, Piers Turner, Achillefs N. Kapanidis, bioRxiv 2025.01.21.634148; doi: https://doi.org/10.1101/2025.01.21.634148

2.1 Motivation

For the creation of fluorogenic probes, we focus on doubly-labelled ssDNAs, which are well suited for labelling in a lab environment for a variety of reasons: The sequence allows for specific interactions even at very short lengths (DNA-PAINT applications commonly using only 7-9 nt long ssDNAs[51]) and provides very extensive options for multiplexing.[52–54] Further, the strength of interaction and consequently the kinetics of hybridisation can be tuned across a wide range of time scales (from very transient interactions in DNA-PAINT microscopy (100 to 300 ms[11,54]) to fluorescent labelling of origami structures which can be stable for weeks[55,56]). ssDNA oligos are widely available from a range of commercial suppliers, making the technology available to and affordable for researchers outside expert synthesis laboratories. The spectral properties of the probe can simply be changed by exchanging the conjugated fluorophore, of which a huge variety is commercially available. ssDNAs are compatible with live-cell experiments (especially once protected by chemical modifications), and through their potentially very small size little impairing on e.g. diffusing properties of a labelled protein complex.

The generation of fluorogenicity in our probes follows a simple principle: A ssDNA is labelled terminally with a fluorescent fluorophore on the 5' and a dark quencher on the 3' terminus. When in solution, the low persistence length of ssDNA ($\approx$ 1 nm) allows it to collapse into a random coil, whereby fluorophore and quencher are kept in close enough proximity to allow for contact-mediated or high-efficiency FRET quenching of the fluorophore's fluorescence (see Figure 2.1A). Upon hybridisation, the double-stranded DNA (dsDNA) duplex with its higher persistence length ($\approx$ 50 nm) separates fluorophore and quencher and therefore leads to de-quenching of the probe and an increased fluorescence emission. This concept has been adopted in variety of applications,[36,38,57] but it

was so far assumed that a useful contrast between dark and bright state would require the DNA to be chosen from a very limited range of lengths (of $\approx$ 15 nt) with little possibility to apply the same fluorogenic strategy to shorter or longer constructs with an equally good performance. The underlying assumptions were that in a shorter probe, the remaining FRET quenching would not allow for bright enough fluorescence in the bound state (we did indeed observe this for one of the constructs discussed in chapter 4), while for longer constructs the quenching in the unbound state would not be efficient enough to allow for significant fluorogenicity, unless hairpin structures were designed into the probes (e.g. in molecular beacons). Those structures, however, come with kinetic barriers which slows down hybridisation (in a 17nt beacon, a 5bp stem reduced on-rates by 2 orders of magnitude, from $10^4 M{-}1 s{-}1$ without stem to $10^2 M{-}1 s{-}1$)[58] and can render probes unusable for certain applications.

Here we show that by controlling and tuning the emission of the probes in the quenched and de-quenched state, we can generate fluorogenic probes that overcome the previous design limitations and push boundaries in a wide range of applications, including but not limited to super-resolution imaging, SMF assays, single-molecule tracking, and *in vivo* experiments.

2.2 The design of fluorogenic ssDNA probes

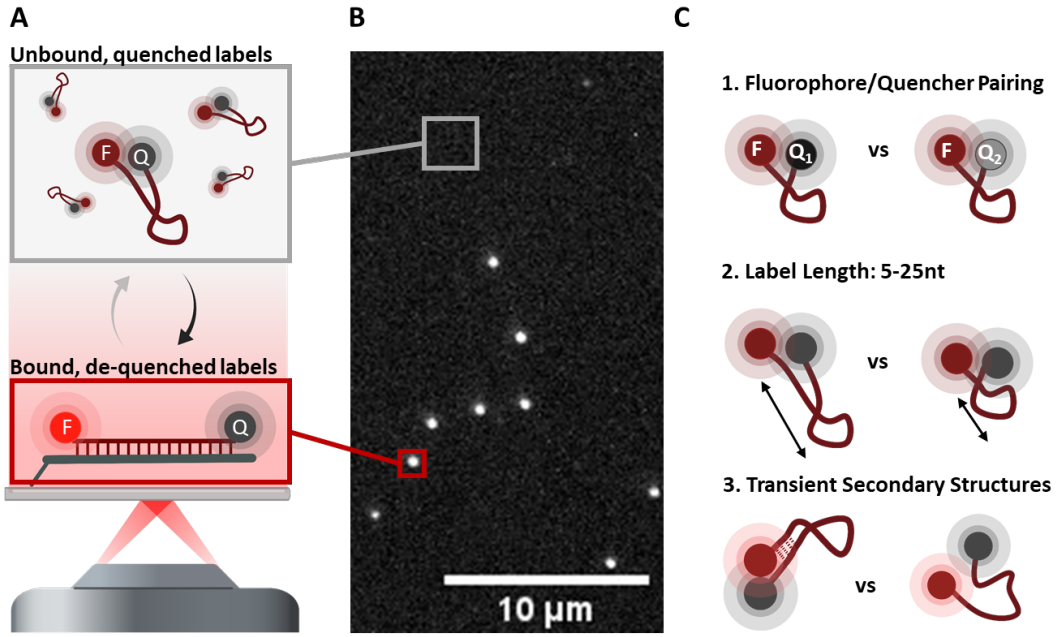

Figure 2.1: Experimental set-up for characterisation experiments. A: ssDNA probes carry a fluorophore and a quencher on the 5' and 3' ends, respectively. In the single-stranded state in solution, the fluorescence emission is quenched. Upon binding their complementary docking strand immobilised on a surface, the fluorescence emission increases because of the increased distance between fluorophore and quencher. B: The measured intensity of spots ('signal') and the background is extracted from the raw video and compared to values of probes only carrying the fluorophore. C: We evaluate three main parameters of the probes, the R_0 of the fluorophore/quencher pairing, the length of the label, and the effect of transient secondary structures.

In the design of our fluorogenic probes, we focused on three key parameters (Figure 2.1C):

- Firstly, the choice of fluorophore and quencher, which through their FRET interaction (and potentially contact-mediated quenching in the single-stranded state) will form the basis for the fluorogenicity.

- Secondly, the length of the ssDNA will determine the distance changes between fluorophore and quencher upon hybridisation.

- Thirdly, the DNA sequence determines the specificity of target binding and influences the hybridisation kinetics. Internal stabilisation of conformations with small fluorophore-quencher distances through transient secondary structures can be an important factor in quenching background fluorescence of unbound probes. Whilst some applications might demand a certain sequence, others will more crucially rely on favourable kinetics of probe binding (e.g. DNA-PAINT imaging). For the latter, it is crucial to eliminate secondary structures and internal interactions between bases by reducing the number of bases to two non-complementary ones.

In order to systematically assess the influences of these parameters, we specifically look at the performance of a set of test or reference probes. These probes were designed to conserve the immediate environment of the fluorophore throughout the different scenarios and to be free of any internal complementarity (by only consisting of two non-complementary bases, G and T). For the purpose of the following experiments, we were not concerned with possible non-canonical interactions (e.g. non-Watson-Crick base-pairings or G-quadruplex structures).

The following measurements were all performed to determine the fluorescence increase upon hybridisation of our probes. We first measured the molar emission of unbound probes ('background' or B, Figure 2.1A-B), extracted from the brightness of the areas in videos which do not contain molecules across a wide range of concentrations. We then fitted with a linear regression to extract the molar background $B_{FQ,mol}$. Since the background is concentration dependent, we thought it best to use the molar quantity when comparing different constructs. Secondly, we extracted the fluorescence intensity of probes that bind to surface-immobilised complementary ssDNAs ('signal' S_{FQ}, Figure 2.1A-B), which is the brightness of spots in our videos at 10 nM. For comparison, we normalised all values to the B and S levels of probes carrying only the fluorophore but no

quencher (B_F and S_F). Both values can be then used to calculate the fluorogenic factor (FF), which is the fold change in emission intensity upon hybridisation:

$$normalised\ S = S_N = \frac{S_{FQ}}{S_F} \tag{2.1}$$

$$normalised\ B = B_{N,mol} = \frac{B_{FQ,mol}}{B_{F,mol}} \tag{2.2}$$

$$\mathrm{FF} = \frac{S_N}{B_{N,mol}} \tag{2.3}$$

This normalisation makes the FF independent of any fluorescence increase upon binding of fluorophore-only probes, which could be dye- or sequence-specific. To keep our assessment as general as possible, we would like to be agnostic to these effects. Any FF>1 in this work reports on a fluorogenicity greater than what could be observed in the fluorophore-only constructs (observed for example by Chung *et al.*).[36]

A full description of all experimental procedures can be found in the A.

2.3 The tuning screws for fluorogenicity

2.3.1 The Förster radius of the fluorophore-quencher pair

In the quenched state, the probe design is relying on contact-quenching or very high-efficiency FRET quenching of the fluorescence emission of the fluorophore. Both require close proximity, and a certain spectral overlap.[59] Upon target binding, the increased distance between fluorophore and quencher allows for de-quenching and recovery of the fluorescence signal. The remaining quenching is due to FRET at distances which exceed the range of any contact quenching (which is assumed to be the case for all tested probes here).

For the FRET component, the spectral overlap between fluorophore emission and quencher absorption is one of the defining factors in determining the Förster radius R_0. We envisioned that changing out the quencher and modifying the R_0, would allow us to modify the emission of a given label and what distance changes are required for high fluorogenicity. Here, we tested the same 15 nt long construct labelled with a 5' fluorophore (ATTO647N) and several quenchers on the 3' end (BHQ1, BHQ2, BBQ650, Figure 2.2A). We used the absorption spectra of the three quenchers, in conjunction with the emission spectra of the fluorophore to calculate the R_0 between fluorophore and quencher based on an assumed $\kappa^2 = \frac{2}{3}$ (Figure 2.2A). We estimated their Förster Radii to be 3.5 nm, 5.2 nm, and 6.2 nm for BHQ1, BHQ2, and BBQ650, respectively, when paired with Atto647N as donor. We chose 15 nt as probe length to allow for reliable detection of both signal and background fluorescence (at end-to-end distances of 3-4 nm in the ssDNA state and approx 5-6 nm in the dsDNA state, calculated using worm-like chain model (WLC) and data from SMF studies)[60,61] both well above instrument noise levels in all cases). All quenchers were chosen to have similar molecular structures, in an attempt to minimise effects of structure-based changes in quenching behaviour.

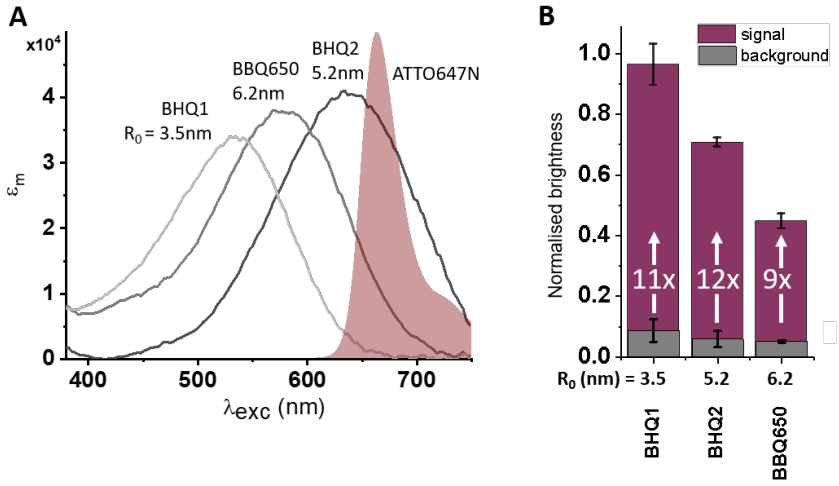

Figure 2.2: The effect of varying spectral properties of the quencher on Fluorogenicity. A: Absorption and emission spectra of the Qs and F, respectively. B: Fluorogenicity characterisation. Red: Signal intensity in the hybridised state, normalised to the fluorophore-only reference construct. With increasing R_0 of the fluorophore/quencher pair, the recovered signal from hybridised probes decreases. Grey: Background emission by unbound probes, normalised to the fluorophore-only reference construct. The background emission is efficiently quenched in all tested constructs, and higher for fluorophore/quencher pairs with large R_0. The FF as the measure for overall performance is similar for all constructs, with the BBQ650 performing worse (FF= 8.8 ± 0.2) than both BHQs (FF= 11.9 ± 0.4 and FF= 11.1 ± 0.9). Mean values and standard deviation from three independent experiments.

In the quenched, single-stranded state, we find the background decreasing with increasing R_0 of the fluorophore/quencher pair, consistent with a higher degree of FRET quenching (Figure 2.2B, 'background' in grey). However, even in the case of the lowest R_0 (3.5 nm, ATTO647N and BHQ1), we find very efficient quenching with a background of below 10 % of the fluorophore-only reference construct. Especially for the BHQ1-construct, quenching is more efficient than we would expect for a purely FRET-based quenching mechanism at a distance of 3-4 nm separation between dye and quencher (where we would expect only about 50% quenching).

The fluorescence signal upon probe hybridisation follows the same trend (Figure 2.2B, 'signal' in red): A large R_0 correlates with low signal from the de-quenched

probe. With the ATTO647N-BHQ1 construct, the full signal can be recovered, whereas with for the high spectral overlap construct (ATTO-647N-BBQ650), we recover ≈45 % of the signal of the fluorophore-only reference. The observed signal levels align well with expected FRET-efficiencies at dye-quencher distances of approx. 5-6 nm. For a given design of label, it is important to choose the quencher that most efficiently quenches the fluorescence in the unbound form, while ensuring significant de-quenching upon hybridisation.

Our results highlight the quencher choice has to be carefully balanced for an optimal fluorogenic probe: In the unbound state, a quencher with large spectral overlap (e.g. BBQ650 for Atto647N) is most desirable; in contrast, for the bound and de-quenched state, probes with a small spectral overlap between fluorophore and quencher have the brightest signal.

Upon calculation of the FF, we can see that the constructs with BHQ2 and BHQ1 seem to perform overall best (FF= 11.9 ± 0.4 and FF = 11.1 ± 0.9, respectively), with BBQ650 achieving a slightly lower FF of 8.8 ± 0.2. The comparably small differences suggest, however, that high FFs can be achieved with a range of quenchers and that the choice of quencher allows to dim or brighten a specific probe in both states. We hypothesise, that the FF of a particular label depends much on how exactly the distance changes align with steep parts of the distance-vs-FRET-Efficiency curve and might thus be of more significant effect in probes of different length (shorter or longer than 15 nt).

Overall, R_0 is a good (and quantitative) predictor for signal levels which can be expected after hybridisation. In the single-stranded state, R_0 allows predicting the trends which the background follows, but quantitatively underestimates the quenching we observe (and we find a similar effect in section 2.3.2). This could be due to either an underestimation of the actual dye-quencher distance or because of further quenching processes.

For design purposes, the R_0 thus serves as a "tuning screw" based on other parameters and requirements of the experimental design: an assay which requires a very short probe (such as the DNA-PAINT imaging we are performing), i.e. where even in the de-quenched state fluorophore and quencher are very close, a low spectral overlap can help to recover enough signal to perform insightful measurements. On the other end of the length spectrum, probes where hybridisation allows for a large separation of fluorophore and quencher, the background can be more efficiently suppressed than with a fluorophore-quencher pair with a high R_0. The ideal quencher thus always depends on the specific requirements of the experiment and the choice should be made taking those into account.

2.3.2 Probe length and separation between fluorophore and quencher

In a distance-sensitive process such as FRET, the probe length has a profound impact on the fluorogenicity. We characterised a series of probe lengths spanning across the range of 5 to 25 nt, with 5 nt being the shortest we were able to observe hybridisation to surface-immobilised complementary DNA. We chose a fluorophore-quencher pair with low spectral overlap (ATTO647N and BHQ1) to allow for sufficient de-quenching of the very short probes to be able to reliably detect them.

Figure 2.3 shows the observed signal and quenched background emission (Figure 2.3B) for probes of different lengths, from which we calculated the FF (shown in Figure 2.3A). Overall, the quenched state emission (background) increases with increasing length, from the 5 nt probe which is emitting only 1 % of the de-quenched probe to the 25 nt probe at approx. 27 % (Figure 2.3B). However, for lengths between 6 and 20 nt, the background shows no significant increase, suggesting that the dynamics of the structure allow for a similar

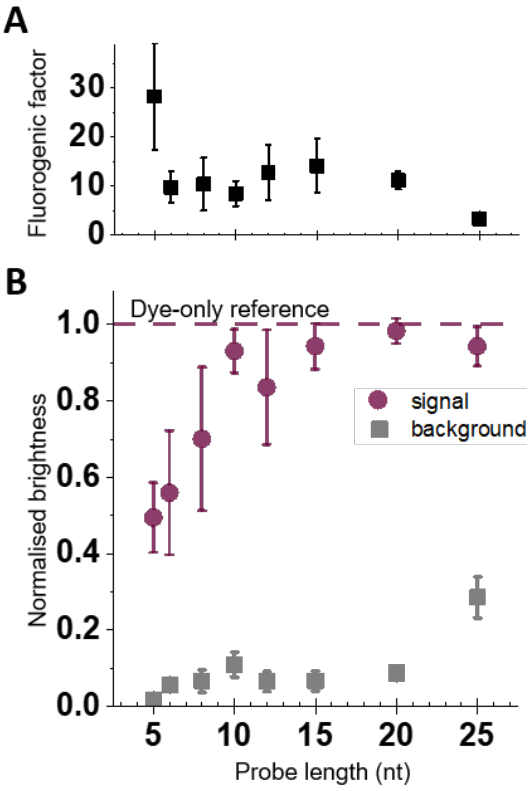

Figure 2.3: Length dependency of Fluorogenicity. A: The fluorogenic factor (FF) calculated as the ratio of values in panel A and B. The 5 nt probe showed the highest fluorescence enhancement upon hybridisation, between 6 and 20 nt, the FF was constant, it then decreases for even longer probes. B: Red: Signal intensity in the hybridised state, normalised to the fluorophore-only reference construct. With increasing length, the signal increases and saturates from 10 nt onwards at the intensity which is expected for a case without any residual FRET-quenching. Grey: Background emission by unbound probes, normalised to the fluorophore-only reference construct. The background emission is efficiently quenched in all tested constructs, with the lowest background level observed with the 5 nt probe. Background in general increases with label length, with a stable level for intermediate lengths between 8 and 20 nt. Mean values and standard deviation from three independent experiments.

level of quenching across these lengths. Even in the 25 nt probe length, the background is only 27 %, so presumably collapses into a random coil which puts the fluorophore and quencher at distances on average well below the R_0 of the fluorophore/quencher pair (3.5 nm).

In the de-quenched state, the signal intensity follows a more typical FRET-efficiency curve shape for FRET-based quenching at the distances set by the probe length. Most promisingly, the short probes (5-8 nt) already show an emission of 50-70 % of the saturation fluorescence signal (Figure 2.3B). Using a FRET pair with a small R_0, as in this case, has allowed us to recover sufficient fluorescence emission in the de-quenched state for single-molecule measurements, despite the very short distance in the dsDNA state formed upon hybridisation.

With increasing length, the signal further increases, until it saturates at the full fluorescence level from 10-12 nt onwards.

When comparing our experimentally obtained quenching efficiencies to theoretical predictions (dye-quencher-distances were estimated using the WLC, with a correction for the helical nature of dsDNA), we see that there is a stark deviation from predicted behaviour in the ssDNA probes, with the dye-quencher-distances being much lower than predicted by the WLC model (Figure 2.4A). It suggests that there are further interactions involved in the overall process which could either bring fluorophore and quencher into much closer proximity (e.g. by stacking of the chromophores) and/or the fluorophore is affected by further, non-FRET based quenching mechanisms, further lowering the emission below what would be expected in a FRET-only system. For our purposes of the label design, this is very advantageous, as it keep background levels low even for labels where the dye-quencher-distances were predicted to exceed the R_0 by far.

For the hybridised probes, the WLC predictions are more consistent with the experimentally observed values, but suggest a smaller R_0 than we have calculated (Figure 2.4B). Since our WLC predictions were made with very rough parameter estimates (in particular of linker lengths and without accounting for major- vs. minor-groove distances) combined with the assumptions made when originally calculating the R_0 values (constant quantum yield of the fluorophore, and complete rotational freedom of both fluorophore and quencher), these deviations lie within the accuracy of our predictions.

For evaluating the fluorogenicity, we calculated the FF (Figure 2.3A). Very short probes have the highest FF - It seems this is mainly caused by very low levels of background emission and could hint at additional quenching processes beyond the ones seen in longer probes – or the average distance of fluorophore and

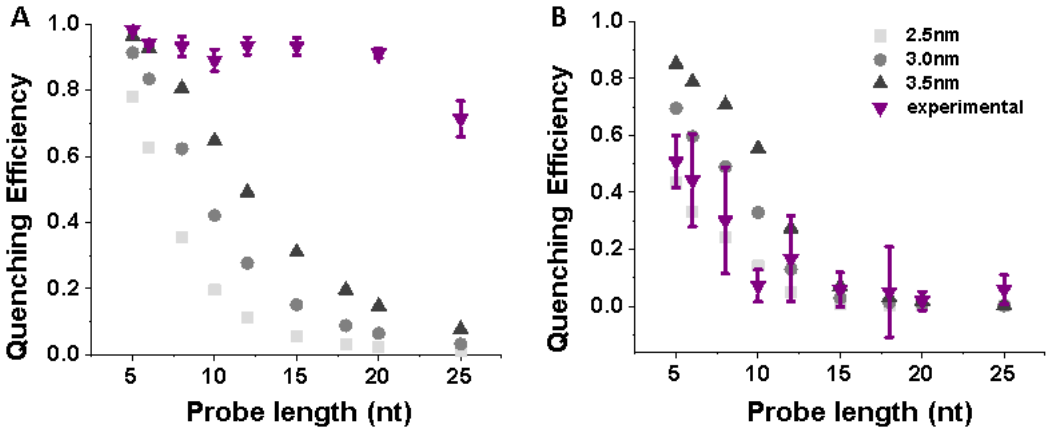

Figure 2.4: Comparison of experimental data (purple) and predictions for the quenching efficiency at different R_0 from 2.5-3.5 nm (grey). A: Unbound, ssDNA probes: Quenching is much more efficient than predicted by the WLC model. B: hybridised, dsDNA probes: The experimental values follow the expected trend of the quenching efficiency, albeit more consistent with a lower R_0 of between 2.5-3.0 nm. Error bars are standard deviations of three independent experiments.

quencher is much lower than in longer probes – resulting in very efficient FRET-quenching. There is a length window between 10 and 20 nt, where (almost) the full signal is recovered and there is still efficient background suppression, leading to a FF of $\geq$ 10 for all lengths. For the 25 nt label, the increased background reduces the FF and we would thus expect to see even lower level of fluorogenicity from this fluorophore/quencher pair for probes exceeding lengths of 25 nt. It is worth noting, that these observations are made for this specific fluorophore/quencher pair. For a more efficiently quenching pair (with a longer R_0), we expect the signal in the hybridised state to only be fully recovered at longer lengths, i.e. greater distances between fluorophore and quencher. For the ssDNA state, the background increase might then also only occur for longer probes, making this a promising approach for the design of longer fluorogenic probes. On the contrary, for very short probes, the R_0 should be chosen to be as short as possible to allow for sufficient signal recovery upon hybridisation.

2.3.3 Transient secondary interactions

Based on the strong distance-dependency of the FF, we wondered whether the deliberate introduction of transiently stabilising secondary interactions into our constructs could help further improve the FF, especially in longer probes (Figure 2.5A). This approach is used in the design of molecular beacons, which often use hairpin-like structures created by the complementarity of a stem region, usually situated at either end of the probe. Often, these stem regions are of significant length (e.g. 6 nt[29]) and thus forms fairly stable structures within most experimental conditions. Consequently, the hybridisation kinetics will be impaired significantly (the on-rate of molecular beacons with a 5 or 6 bp stem was reduced by several orders of magnitude)[58], which can render the probe unsuitable for certain applications.

The probe used in chapter 5 is 18 nucleotides long and complementary to the 16S ribosomal RNA, which allows it to hybridise to ribosomes. Within its sequence, there is a short, 4 nt intramolecular complementarity within an 18 nt probe (ΔG = -4.23 kcal/mol at 25 °C based on NUPACK[62]). The NUPACK prediction shows that this folds the 3'end into the centre region (Figure 2.5B) and is not forming a terminal stem region (like molecular beacons would). We hypothesised that this would shift the equilibrium of possible ssDNA states in the unbound state towards those with base-pairing, and hence impose a closer distance between fluorophore and quencher (Figure 2.5A). At the same time, the stability of this interaction is low, and it should not inhibit binding to a target. The open 5' end can further serve as a toehold for hybridisation, facilitating an initial interaction with the complementary sequence without requiring the internal interaction to open beforehand.[63]

In our single-molecule experiments, the signal upon hybridisation was not affected by this internal interaction, hence we recovered close to 100 % of the fluorescence

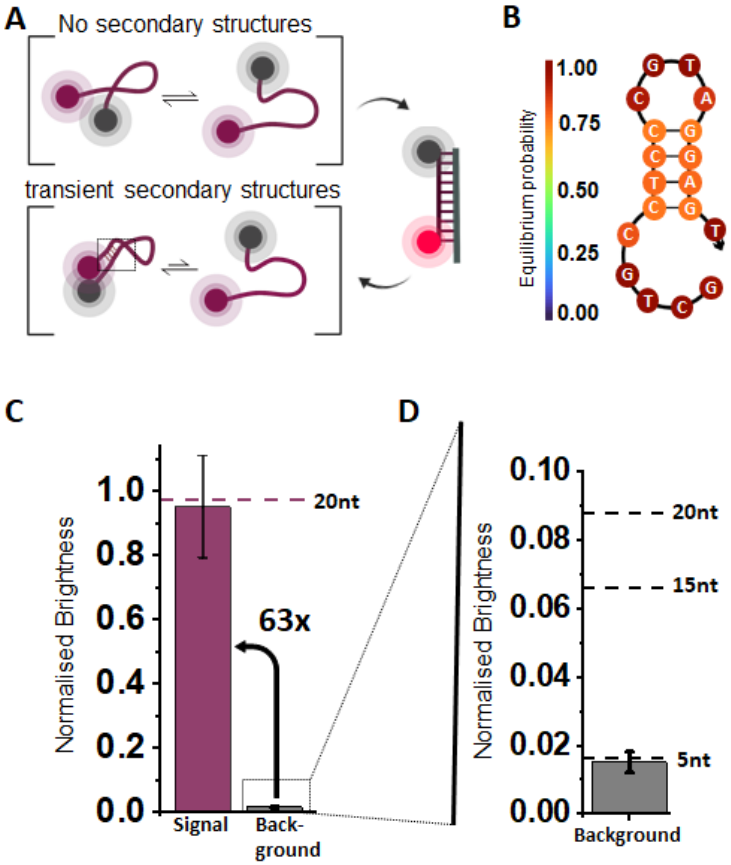

Figure 2.5: Secondary interactions can improve fluorogenicity in a 18nt probe. A: Schematic illustration of the reduced conformational dynamics in the unbound, ssDNA state of probes capable of forming intramolecular base pairs, which leads to an on average reduced distance between fluorophore and quencher. B: NUPACK prediction of the secondary structure of the 18 nt probe at 25 °C based on a 4 nt self-complementary region of the 3'- and centre section of the sequence. C: Signal intensity in the hybridised state and background level of the 18nt probe, normalised to the fluorophore-only reference construct. The 18nt probe with secondary structure emits the same signal level as the fluorophore reference and the 20 nt fluorogenic sample (dashed line, data from Figure 2.3), suggesting full hybridisation and no residual FRET quenching. The background is reduced to 1.5 - 2% of the fluorphore-only reference, resulting in a FF = 63, 5x larger than in reference constructs of comparable lengths (dashed lines in panel D, data from Figure 2.3). D: Zoom in of panel C. Mean values and standard deviation from three independent experiments.

signal (Figure 2.5C) At the same time, we could indeed confirm that even a 4nt complementarity was sufficient to reduce the background emission of this 18nt probe to a similar level as we have observed in the (much shorter) 5nt probe (Figure 2.5D). Consequently, the FF of ≈ 63 in this probe was the highest we have observed in any of the constructs, and much higher than comparable probes without secondary structures exhibit (compare the 15 and 20 nt probe without secondary structures in Figure 2.5A). This approach should be extendable to any long probe, where a complementary region of a certain length can be sufficient to bring fluorophore and quencher into close proximity even if this interaction is not stable in the given experimental conditions.

2.4 Single-molecule assays at micromolar concentrations

The design parameters outlined above allow for the generation of highly fluorogenic probes which can be used in single-molecule experiments at concentrations orders of magnitude above the concentration limit of 100 nM. Figure 2.6A shows different FOVs of the 18 nt probe with a transient secondary structure studied in Figure 2.5. Even at 10 μM, individual molecules can clearly be distinguished and could be analysed for desired parameters such as brightness, location etc. Operating at high concentrations is particularly important in single-molecule experiments which rely on the accumulation of statistics from individual molecules, and where without a sufficient on-rate this process can be long and tedious.

In order to demonstrate our capability to operate single-molecule experiments at concentrations in the μM range, we perform a simple assay which is capable of detecting single-base mismatches in a target structure by evaluating the hybridisation kinetics of a fluorogenic probe (Figure 2.6B).[20]

2.4.1 Experimental design

A full description of the experimental procedures can be found in the appendix. The probe in this case is an 8nt long sequence, labelled with Atto643 and BHQ1, a fluorophore/quencher pair with a low R_0, allowing for a good de-quenching performance of the probe whilst still offering good quenching in solution. A fully matched target will lead to a more stable interaction with the probe, compared to one with a destabilising single-base mismatch. The target itself is double-stranded, but has a 8 nt long "gap" of ssDNA that offers a binding site. To create the mismatches, we will vary the base at the position marked with 'X'. The probe hybridisation in this setting is additionally stabilised by stacking interactions on either side (Figure 2.6B).

2.4.2 Results

Using a fluorogenic probe, the assay could be performed at 2 μM with an SNR sufficient for detection of binding events, as illustrated by the fluorescence-vs-time traces in Figure 2.6C. The dwell times of all binding events were extracted for all four possible bases at the position labelled with X, and their clearly show the more stable interaction of the probe with the fully complementary target with G at the position X, which leads to longer average bound times (Figure 2.6D). The single mismatch reduced the average interaction lifetime by a factor of approx. two (1.1 s (complementary) vs. approx. 0.4-0.6 s (mismatched)) and thus allows for a clear distinction of target sequences purely based on the hybridisation kinetics[20].

Whilst the average of all bound times is a good indicator in this case, a further analysis reveals more details: From previous studies of the kinetics of DNA hybridisation, we know that the observed event duration usually contains (at least) two components, consequently we fitted two lifetimes describing the process.[64]

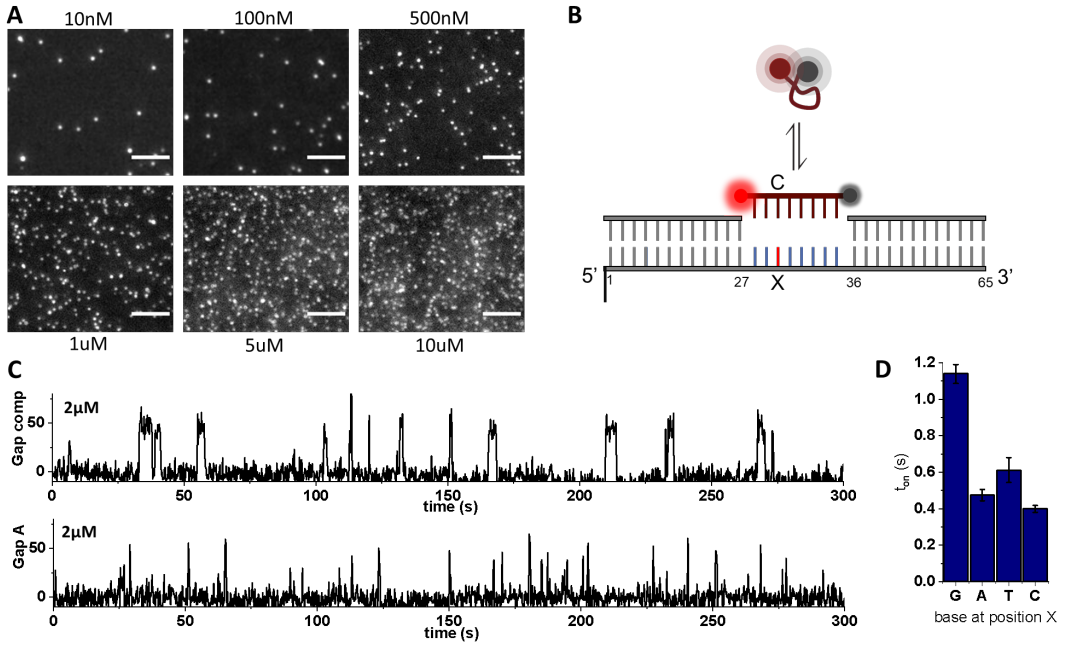

Figure 2.6: Single-molecule experiments at μMconcentrations. A: Single frame images of the 18 nt probe (described in Figure 2.5) at various concentrations, binding to complementary target strands. Individual molecules can be identified at all concentrations up to 10 μM. B. Single-molecule assay for mismatch detection and base calling. The binding kinetics of fluorogenic 8nt probes will distinguish the fully matched sequence from a mismatch at position labelled with X. C. Intensity-vs-time traces of an 8 nt probe binding to a target at 2μM, top: fully complementary target, bottom A:C mismatch at position X. D. The duration of binding events extracted from time traces at 2μM probes for all for possible bases at position X. Lifetimes were fitted accounting for the camera frame rate and error bars are 95 % confidence intervals determined by bootstrapping.

These lifetimes represent two different hybridisation states: The shorter one is a (or a mixture of several) partially hybridised and short-lived state, possibly the initially formed 3-4 bp nucleation site, from where the full hybridisation develops.[64] The larger lifetime is then representing this fully hybridised state. Previous experiments and the theoretical modelling by Ouldridge *et al.* does not exclude further states (and rather assumes an enselmble of states)[64,65], however fitting even lifetimes into an exponential decay is difficult and, if possible, requires an even larger amount of data points to be accurate.

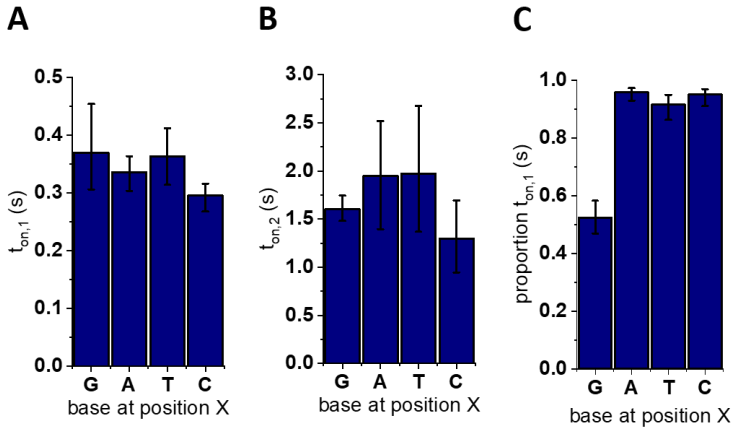

Figure 2.7: Two-exponential fit of the 8 nt probe bound times at fully complementary targets or single-base mismatches. A: Bound-time, first component. B: Bound-time, second component. C: Proportion of fit determined by first component. Both fitted lifetime components have similar values for fully matched and mismatched targets, however the second (longer) lifetime is barely present in the mismatches. Graphs show fitted values with 95 % confidence intervals obtained from bootstrapping.

In our case, both fitted lifetime components for each target, interestingly, are very similar between all four possible bases at the position X, irrespective of the sequence being fully matched or with a single-base mismatch (Figure 2.7A-B, approx. 0.3-0.4 s for the shorter and 1.5-2.0 s for the longer lifetime). Whilst we can theoretically extract a longer lifetime (component 2) from all four samples, it is essentially absent in the mismatched cases, which are almost completely described by the single lifetime of the short component (Figure 2.7C), indicating that the central mismatch does very rarely only allow for the formation of a more stable duplex, in which all possible base pairs are formed.

Operating at 2 μM has allowed us to accumulate approx. 1000 - 3000 fitted binding events within an imaging time of 5 min per FOV, averaging between 10–20 events per evaluated molecule. Use of higher concentration of the fluorogenic probe accelerated the process of delineating the distinction between complementary and mismatch sequences by collecting significant number of

binding events in a shorter span of time due to enhanced on-rate at an escalated probe concentration.

2.5 Conclusion

We have conducted an in-depth characterisation of the fluorogenicity in self-quenching ssDNA probes (terminally labelled with F and Q), carefully evaluating the effect of probe length, R_0 of the F-Q pair, and transient secondary interactions on the fluorogenicity of ssDNA probes. Utilising this has allowed us to create highly fluorogenic constructs over a wide range of lengths and with different F/Q pairs.

Previously, optimising for the highest degree of quenching in the unbound state lead to the conclusion that a minimum of around 15 nt distance had to be incorporated between dye and quencher to allow for sufficient de-quenching for single-molecule detection.[36,52] This was based on the assumption that a large R_0 of approx. 6 nm was required. However, by focusing on the principles guiding the de-quenching efficiency, we can construct probes of high FF of various lengths, the shortest being 5nt. We could further provide strategies which can increase quenching (and thereby fluorogenicity) in longer probes. The probe length in our design is fully flexible within the regions interesting for hybridisation kinetics, spanning the timescales of most experiments (5-25 nt), and through the introduction of secondary structures, even longer designs are possible. We are, however, not relying on specific structural motifs, giving free choice of the sequences used.

Our findings can easily be translated to other spectral regions. We chose the red dye ATTO647N for our characterisation, but have also performed experiments with ATTO643. No data is shown in this thesis, but we have designed probes with Cy3B as well with similar success. The only spectral or dye-specific property

in our design is the R_0 of the F-Q pair, which can easily be determined for any combination by evaluating available spectral data, independent of the spectral region of interest. Previous approaches and our work in chapter 4 on short (8-11 nt) ssDNA fluorogenic probes have used a self-quenching approach, whereby two terminally fluorophores on the probe would contact-quench in solution.[20,38,57] This approach is, however, limited to very specific fluorophore (ATTO647N and ATTO655) and does not easily translate to other spectral regions.

For most of the experimental work, we have focused on FRET as the quenching mechanism, but we have also found some evidence suggesting other mechanisms might contribute to the quenching in the unbound state. We have not focused on them in this study, but hypothesize they will only improve the FF, as the unbound state will be further darkened without affecting the de-quenched fluorescence significantly (given the same R_0). Such contributions could be tested and optimised for by finding the most efficient amongst the available quenchers of a similar R_0 with the fluorophore of choice. Because R_0 are measurable and - to a certain degree - predictable from information often provided by manufacturers, quenchers can be pre-selected for their R_0 and then only a subset of suitable candidates tested for the best contact quenchers – a property which to the best of our knowledge is much more difficult to predict from information accessible before experimental testing.

In conclusion, when applying the presented findings to new probe designs, we have found the following to be helpful guidelines:

- For short labels (shorter than 8-10 nt), the de-quenching in the hybridised state is the limiting factor. Here, short R_0s are particularly important. In combination with ATTO647N and ATTO643, BHQ1 worked well (see following figure 2.6 and chapter 3). These are particularly interesting for applications where fast turnover kinetics are required.

- Intermediate labels, approximately 10-20 nt, are fairly flexible regarding R_0, so the quencher choice is less crucial to achieving a good FF. However, in applications where photon counts are crucial, a low R_0 might aid in facilitating bright signal levels. Maximising the achievable concentration of probes might, on the other hand, require a higher degree of quenching of unbound probes, as can be achieved with a larger R_0 pair.

- For long probes (longer than 20 nt), large R_0 will help in maintaining good quenching of the unbound state, whereas they will not (or barely) affect signal levels once hybridised. These probes allow for stable labelling under most buffer conditions.

3

Fast super-resolution imaging with 6 nt imagers for DNA-PAINT

Contents

The work presented in this chapter is part of the manuscript:

Tunable fluorogenic DNA probes drive fast and high-resolution single-molecule fluorescence imaging, Mirjam Kümmerlin, Qing Zhao, Jagadish Hazra, Christof Hepp, Alison Farrar, Piers Turner, Achillefs N. Kapanidis, bioRxiv 2025.01.21.634148; doi: https://doi.org/10.1101/2025.01.21.634148

3.1 Motivation

To demonstrate a fast and easy implementation of fluorogenic probes into existing experimental protocols, we performed localisation-based super-resolution imaging using DNA-PAINT with a fluorogenic imager. DNA-PAINT allows for imaging of biological samples through the accumulation of localisations from fluorescently labelled imager strands transiently hybridising to complementary docking strands bound to the target structure of interest (see Figure 3.1).[11,51] The spatio-temporal separation of single emitters required for super-resolution imaging is here achieved through a hybridisation reaction, rather than photo-physically as in similar methods like PALM and STORM. Multiplexing in DNA-PAINT is achievable by using orthogonal imager and docking site sequences, then even the same optical channel can be re-used for imaging another target after washing away imager strands in between imaging rounds (so-called exchange-PAINT).[53]

Much like other SRM techniques, the acquisition of a single image is time-consuming, in particular because it is the experimental environment which determines imaging speed in DNA-PAINT. It is primarily determined by two factors: the hybridisation kinetics of imagers to the docking strand and the need for motion blur of unbound imagers, which is required for precise localisation of only target-bound imagers.

To date, the significant imaging time dictated by these two factors is still a major limiting factor to the image acquisition in multiplexed DNA-PAINT experiments. Fluorogenic imagers can help to address both points: Through them being essentially dark when unbound, the need for motion blur is significantly reduced, so shorter exposure times can be realised without resolving unbound imagers. Secondly, speeding up the actual kinetics of the hybridisation/de-hybridisation cycle requires fast off-rates (i.e. shorter sequences) as well as faster on-rates, which is facilitated by higher imager concentrations. Recent developments have

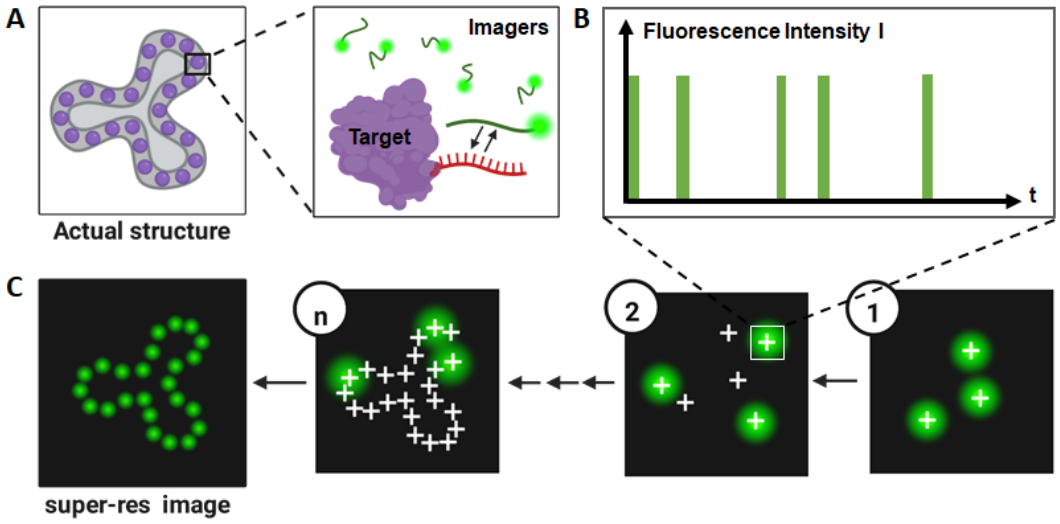

Figure 3.1: Principle of DNA-PAINT imaging. A: The target molecule of interest in its structure is not labelled with a fluorophore directly. Instead, a ssDNA docking site is attached, to which so-called imager strands (fluorescently labelled) transiently hybridise. B: The hybridisation pattern induces blinking at each position, akin to other photo-physical blinking used in PALM and STORM. C: The super-resolution image is reconstructed from the localisations observed in subsequent frames.

seen fluorogenic imager strands[36–38] to allow for faster image acquisition, but efforts focused on specifically developed sequences (which include mismatches) or the use of a limited set of fluorophores to achieve fluorogenicity:

The first use of fluorogenic imagers for DNA-PAINT microscopy was reported in 2022.[36] The authors identified the need for fast exchange kinetics in combination with background suppression if faster exposure times should be implemented in DNA-PAINT microscopy. Under the assumption that in a dye-quencher labelled probe, no significant de-quenching would be achievable below 15 nt, Chung *et al.* selected and optimised two 15 nt sequences with internal mismatches to exhibit similar binding kinetics to a fully matched 6 nt imager. This allowed fast imaging in two different colour-channels at 20 ms exposure times. Further imager sequences using this approach have not been developed to date.

Building on this approach and addressing its multiplexing limitations, FLASH-PAINT ("fluorogenic labelling in conjunction with transient adapter-mediated switching for high-throughput DNA-PAINT") activates and de-activates only a subset of docking sites in subsequent rounds of imaging.[37] Through removable adapter strands, which provide these docking sites to the specific target, multiplexing of targets can be achieved whilst maintaining the same imager sequence (e.g. the mismatched, 15nt sequence introduced by Chung *et al.*). In contrast to the conventional exchange-PAINT, not the imagers but the docking sites are exchanged between rounds of imaging, and multiplexing even with just two fluorogenic imager sequences has been demonstrated for numerous cellular targets. The exchangeable adaptor strands are, however, yet another element in the experiment which might require optimisation, and as the authors highlight, exchange of the docking sites requires several minutes to be completed.

Kessler *et al.* followed a different approach to achieve fluorogenicity, by using two terminal ATTO655 dyes on the imager, akin to our red r-label in chapter 4 (with two terminal ATTO647N).[38] This approach allowed to use a conventional imager sequence, and can thus (presumably) be multiplexed similarly to conventional DNA-PAINT. However, self-quenching behaviour has not been reported for many dyes (and in our own experience specifically does not work with e.g. Cy3B), and so spectral multiplexing and operation using a different excitation laser is difficult. Further, the achieved fluorogenicity was about a factor of five, which substantially lower than we could demonstrate using a dye-quencher combination.

Whilst the approaches in the literature provide sensible solutions to the task at hand - increasing the acquisition speed of DNA-PAINT experiments through the use of fluorogenic imagers, they so far required substantial sequence engineering of either imager or docking sequences, or were spectrally limited to very few dyes. Our fluorogenicity approach enables us to create very short imager strands not

limited to the previously used fluorophores or imager sequences, which, if used at high concentrations, can speed up imaging significantly. The quenching strategy allows for better background suppression than the self-quenching approach and can be integrated seamlessly into an existing DNA-PAINT protocol.

3.2 Interrogating the structure of the Influenza A genome

The Kapanidis Lab has recently developed a DNA-PAINT labelling protocol to study the genomic structure of the Influenza A virus.[15] In this negative-sense, single-stranded RNA virus, the genome is organised on eight segments. In each of these viral ribonucleoprotein complexs (vRNPs), the three viral RNA polymerases together with the viral (v-)RNA, wrapped around the exterior of oligomerised nucleo-proteins (NPs), form a complex stabilised by intramolecular interactions (Figure 3.2A-B).[66] In the viral life-cycle, these segments need to be packaged into viral particles, which can then be released from a host cell to infect a new target. Despite its importance in the prediction and management of influenza pandemics, the mechanistics of the packaging process are yet to be fully understood.

Based on recent evidence, some form of packaging signal seems to control the assembly of one complete set of segments.[67,68] Previous studies have shed light on the nature of inter-segment interactions, which could aid in such a selective assembly process. Whilst some studies highlight the importance of several sequence motifs and direct base-pairing (mutational analysis[69–71]), some predict a complex landscape of contacts along the entire segment length (in-silico and biochemical cross-linking assays[72–74]), others question the importance of RNA-RNA-interactions for packaging all together.[75]

Structural analysis using electron tomography of complete virions suggest that segments align parallelly when budding off a host cell with a central segment mediating the contact to six surrounding segments (termed the "7+1" confirmation, see Figure 3.2C)[76–78], a similar organisation was found in mature particles using Cryo-electron microscopy.[79,80] By using the segment lengths

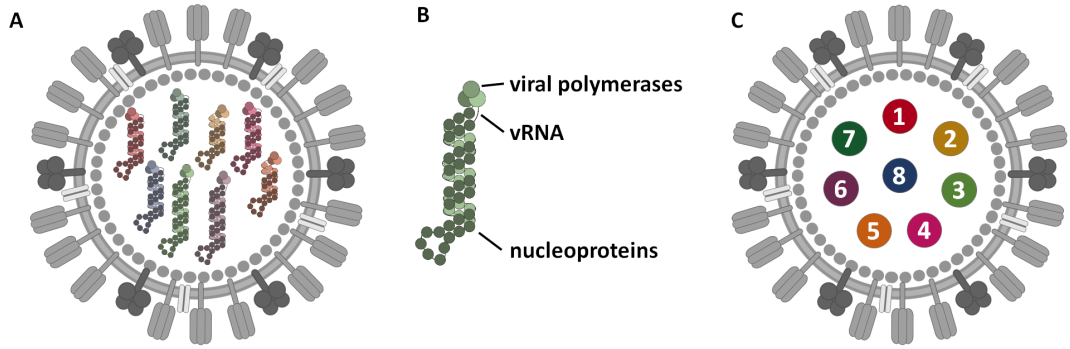

Figure 3.2: Schematic of the structure of the Influenza A genome inside a viral particle. A: A particle contains eight gene segments, encoding the eight viral proteins. B: Each segment consists of a nucleoprotein backbone, around which the viral RNA is wound. Each gene segment further contains the three viral polymerases. C: The proposed '7+1' conformation of segments inside the virion.

to identify certain segments, a significant heterogeneity within the spatial arrangement of RNPs was observed.[78]

DNA-PAINT imaging of the viral genome, as co-workers developed it, allowed to extract structural features and resolving individual segments with a resolution better than $\approx$ 10 nm, linking these features to the segment ID, and also study the presence or absence of individual segments within single virus particles at a large scale (>10,000 individual virus particles).[15] As part of the process, they sequentially interrogated each segment in eight rounds of exchange-PAINT. For the large-scale analysis of the presence and absence of individual segments, imager concentrations were elevated to beyond what would allow for super-resolution imaging in an attempt to shorten data acquisition time — the information was then extracted from intensity-vs-time traces using step-finding algorithms to count binding events. Whilst this was an appropriate solution to the problem at hand, it highlights how limiting the slow imaging process in DNA-PAINT imaging can be for the acquisition of large data-sets.

3.3 Experimental design

A full description of all experimental procedures can be found in the appendix. In brief, for super-resolution imaging of viral gene segments using DNA-PAINT, viral particles are fixed and dried onto the imaging glass surface. Subsequently, they are permeabilised to allow access to segment-specific primary DNA-probes. These label each segment with many (20-60) copies of docking sites for a specific DNA-PAINT imager, as previously established[15] (Figure 3.3A). In eight subsequent rounds of imaging, different segments can be imaged within the same sample. Performing eight rounds of exchange-PAINT is time-consuming, and in our experience the main bottleneck to accessing the heterogeneity within the viral particles at statistically significant levels.

In order to speed up the imaging process, we implemented a fluorogenic imager, which allows much higher operational concentrations. In combination with the short length of only 6 nt, this speeds up the hybridisation kinetics and consequently the imaging process. In our proof-of-principle experiment, we labelled only two of the vRNA segments: The PB1 segment with probes complementary to the 6 nt imager, and the NA segment with probes complementary to the P3 imager sequence used in the original study (as a comparison, Figure 3.3A).[15]

The P3 imager produced the best data quality in the original protocol, so we chose it as a standard to compare the new imager to. The 6 nt imager sequence (5'-TGGTGG-3') was adopted from published imager sequences,[81] but we did not perform any sequence engineering. This was of particular importance since we wanted to demonstrate the ease of adoption of a fluorogenic strategy into an already existing protocol.

We initially tested imaging with the combination of ATTO647N-BHQ1 as fluorophore/quencher pair, chosen because of the low Förster radius allowing

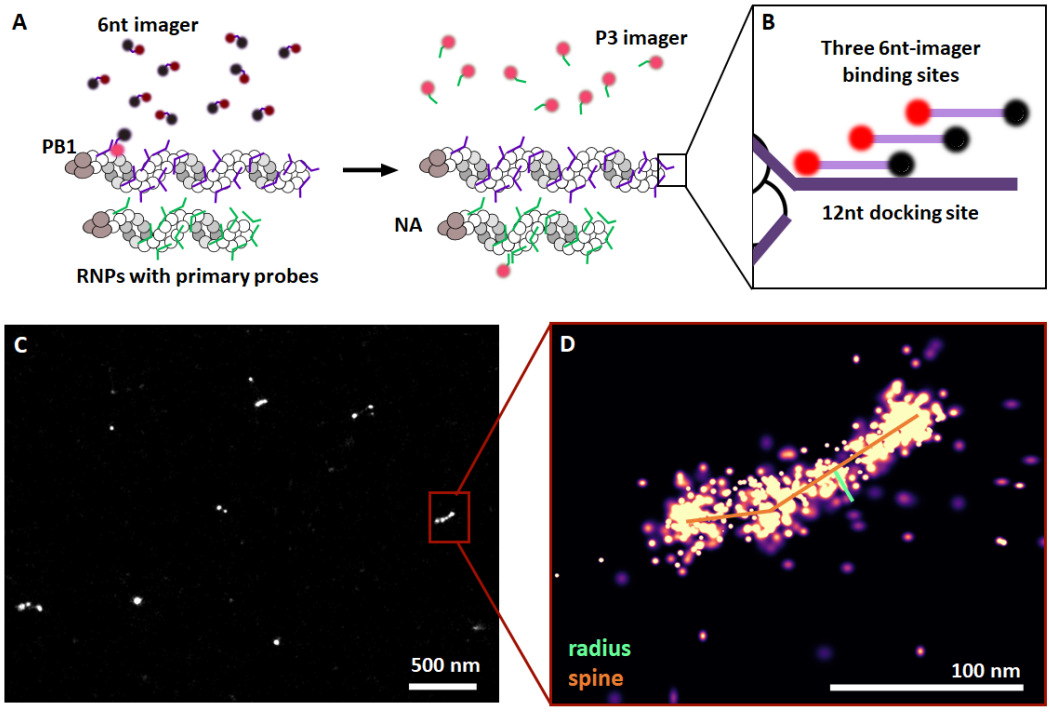

Figure 3.3: Experimental Design of the DNA-PAINT imaging of Influenza A gene segments. A: General strategy for labelling of the viral genome: RNA-carrying viral segments are hybridised by primary probes, which provide the docking sequence for DNA-PAINT imagers. In sequential rounds, the PB1 segment is imaged with the fluorogenic 6 nt imager (purple backbone) followed by the NA segment with the P3 imager. B: Multiplexed design of the 6 nt imager docking site. C: Overview FOV of viral segments imaged with the 6 nt imager. D: Zoom-in onto one segment with radius (green) and spine (orange, drawn here for illustration purposes only).

for good de-quenching at 6 nt length. We later changed to ATTO643-BMNQ1, which proved to reduce unspecific sticking to the surface during imaging and thus improved the performance.

To maximise the on-rate of imager binding, the primary probes carrying the docking site for the 6 nt imager contained a multiplexed docking sequence (extension: 5'-CCACCACCACCA-...), overall creating three possible binding sites for the imager (a concept first introduced in Strauss et al.[54], the docking site is shown in Figure 3.3B). The fluorogenic properties of the 6 nt imager allow

us to raise the imager concentration to 20 nM and shorten the exposure time to 20 ms (compared to 5 nM and 200 ms for the P3 imager)[15] without significant contributions of unbound imagers to the background levels. Since DNA-PAINT uses point-spread function (PSF) fitting to obtain precise localisations for every emitter, it is much more sensitive to background than e.g. the SMF assays we performed in chapter 2, in particular at imaging speed where free imagers no longer blur into a homogenous background. Fluorogenic imagers thus improve the data quality even at concentration much below the "concentration barrier" of 100nM.

The observed localisations are filtered, linked, un-drifted, and analysed for clusters (more details in the appendix). The filtered clusters of localisations are binarised as outlined in Figure 3.4, fitted with a spine along the long axis of the clusters, and a radius perpendicular to the spine. Both parameters report on the physical dimensions of the vRNPs (Figure 3.3C-D and 3.4C). The fitted spine length of the NA segments imaged with P3 exhibits a wide distribution ranging up to about 150 nm, potentially caused by projecting the segments oriented in 3D onto the imaging plane.[15] The segment radius follows a much narrower distribution with a mean of approx. 15-20 nm, in agreement with previous estimates based on electron microscopy.[82,83] We chose the segment radius as the appropriate physical parameter of the viral segments to test our 6 nt imagers and compare to the previous protocol with non-fluorogenic imagers.

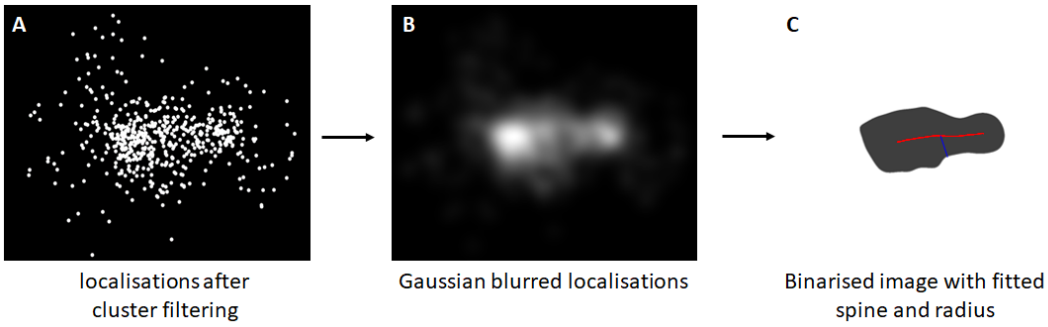

Figure 3.4: The binarisation process to used to fit spine and radius to the clusters. A: exemplary cluster of localisations after filtering. B: A Gaussian blur is added to each localisation, creating a density-based image. C: The density map is thresholded to binarise the image into an area inside and outside the cluster. Spine and radius are fitted into the binary mask.

3.4 DNA-PAINT imaging with a 6 nt imager

3.4.1 Fluorogenicity of the 6 nt imager

The fluorophore and quencher choices were based on earlier characterisation experiments of standardised sequences. We performed the same characterisation again with the specific imager strands used in the DNA-PAINT imaging. Two combinations of fluorophore/quenchers were tested, ATTO647N-BHQ1 and ATTO643-BMNQ1. The first combination was the one deemed most suitable from the original characterisation experiments. Whilst ATTO467N is a very photo-stable and bright dye and well-used for single-molecule experiments, it is known for its hydrophobicity and can cause non-specific sticking.[84] To improve the performance further, we thus also tested ATTO643, a fluorophore developed as the less hydrophobic equivalent to ATTO647N.[85,86] For our very short imagers, both fluorophores were paired with quenchers to have pairs with small R_0 values. With imager sequences as short as 6 nt, de-quenching upon hybridisation would be the main concern for the success of the experiment. For technical reasons with the manufacturer (presumably compatibility in the synthesis pipeline),

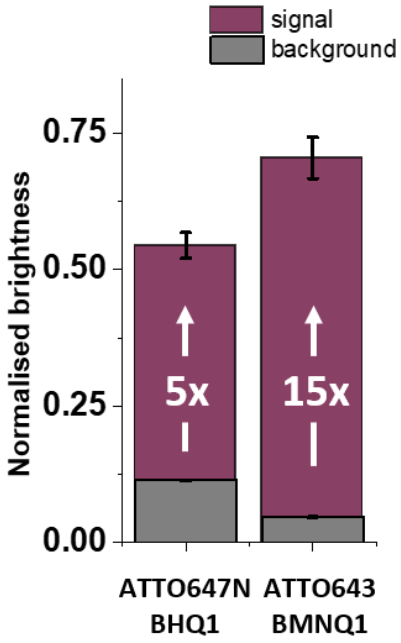

Figure 3.5: Characterisation of the 6 nt imager Fluorogenicity. Red: Signal intensity in the hybridised state, normalised to the fluorophore-only reference construct. Grey: Background emission by unbound probes, normalised to the fluorophore-only reference construct. The ATTO647N-BHQ1 construct had a background of 11% and a signal of 55% of the unquenched construct, resulting in a FF of 5. The lower background in the ATTO643-BMNQ1 construct (5%), combined with the higher signal level of 70% resulted in a FF of 15.

we had to switch from BHQ1 to BMNQ1 in the sequence with ATTO643, but both quenchers share the same properties.[87]

Our fluorogenicity testing aligns with the results expected based on the earlier characterisation experiments: Both sequences have a significantly reduced background level at 5 and 11 % of the reference fluorophore-only sequence for the ATTO643-BMNQ1 and ATTO647N-BHQ1, respectively (see Figure 3.5). The signal levels obtained were 55 and 70 %, respectively, resulting in a FF of 5 for the ATTO647N-BHQ1 and 15 for the ATTO643-BMNQ1 construct. The value for the ATTO647N-BHQ1 strand is lower than expected from previous characterisation experiments, which seems to be the result of higher background levels (11 % for the imager sequence vs. 6 % for the systematic probe sequence in chapter 2). The ATTO643-BMNQ1 imager, in contrast, exhibits a high FF, making it a promising candidate for the actual imaging process.

3.4.2 Specificity of the 6 nt imager

In control experiments, only very few clustered localisations can be detected in a negative control sample without primary probes carrying the docking site for the ATTO647N-BHQ1 6 nt imager strand (Figure 3.6A). This suggests that there are very few non-specific interactions of the imager with e.g. the vRNA of other segments which would lead to spurious localisations. When testing the 6 nt imager against the conventional imager used to label the PB1 segment (P1), we observe high levels of co-localisation when imaging the same field of view (Figure 3.6B). In this particular case, both channels were imaged at the same time, and 50ms was chosen as a compromise exposure time. This will, however, leave a significant proportion of 6 nt binding events undetected, which leads to less signal in the red channel and the visual impression that the P1 imager is detecting more segments.

Both experiments demonstrate that primary probes hybridise well, and binding sites are accessible for the 6 nt imager, which also only specifically binds the correctly labelled segments.

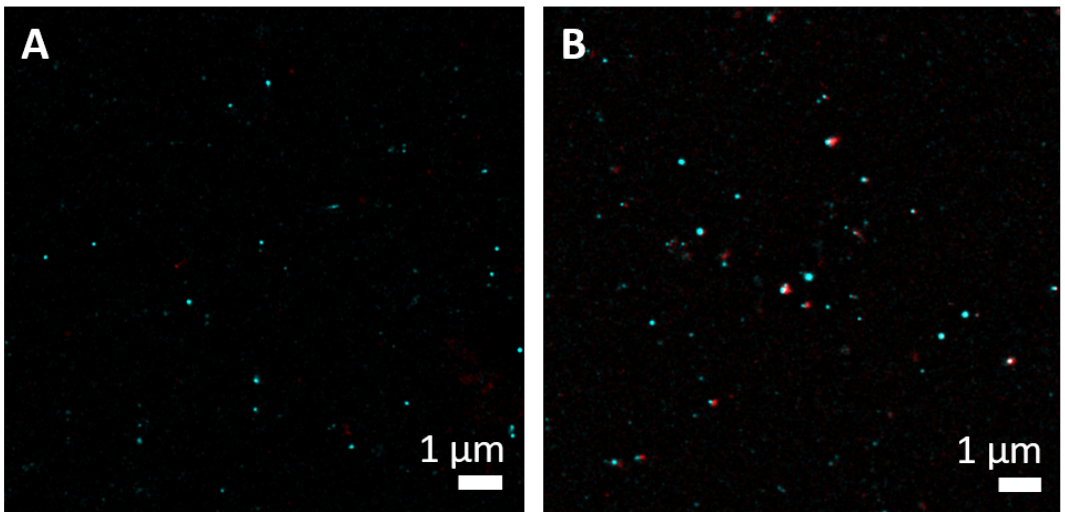

Figure 3.6: Control experiments for 6 nt DNA-PAINT imaging. A: Negative control without primary probes (red) shows few localisations compared to the sample with primary probes (cyan). B: P1 imager (Cy3B, cyan) and 6 nt imager (A647N, red) co-localise at viral segments.

3.4.3 Dye optimisation

Despite the dense clusters of localisations being specifically labelled segments, we observe more localisations uniformly spaced out across the FOV using the ATTO647N-BHQ1 6 nt imager compared to the Cy3B-P3 (Figure 3.7A). We hypothesise these come from non-specific surface interactions of the imagers. When imaging at longer exposure times, these very short events are not picked up (or are very dim and can easily be filtered), but when imaging at 20 ms, they are noticeable. Further, there can be larger ($\approx$ 1μm), less dense or well-defined clusters in the FOV in the 6 nt imaging data, which are far too large for viral targets.

We thus implemented an additional filtering step to extract only those clusters with a high core sampling ratio (i.e. high number of central localisations). This allows to extract only those dense segments we expect to be true viruses and filter out non-clustered or loosely clustered localisations. However, any non-specific binding event will, even in the extracted clusters, lead to noise in the fitting

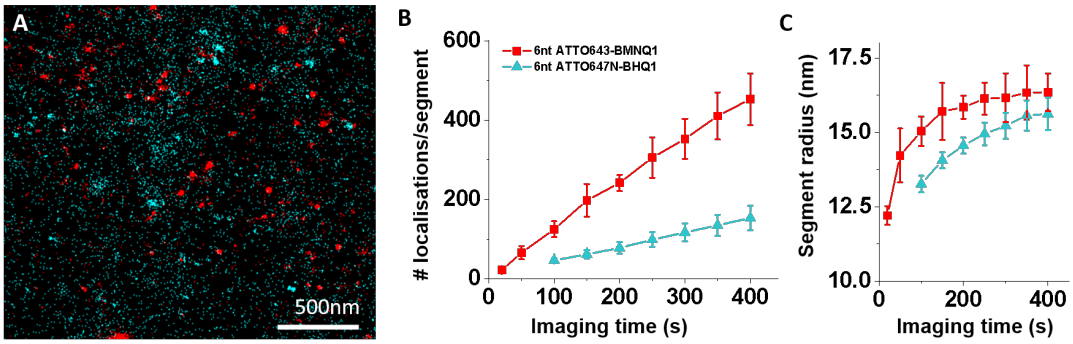

Figure 3.7: Dye optimisation for 6 nt imager. A: non-specific, evenly spread localisations are greatly reduced in the ATTO643-BMNQ-1 (red) data compared to the ATTO647N-BHQ1 data (cyan). Data is presented before filtering, linking, and un-drifting. B: Localisations per Segment for both 6 nt imagers after all filtering steps. C: Segment radii, fitted to the extracted segments.

and therefore skew the results. In an attempt to reduce the localisations coming from non-specific surface interactions, we switched to a less hydrophobic dye, ATTO643. A recent study found both fluorophores to be bright and exhibit a good SNR during the DNA-PAINT imaging process, ATTO643 had a slightly higher photon yield and, most significantly, was much less prone to unspecific interactions (so exhibited a higher specificity) when tested for cellular imaging.[84]

The new ATTO643-BMNQ1 6 nt imager strand had significantly less of the evenly-spread localisations in the raw data than the ATTO647N imager (Figure 3.7A). Presumably because the better SNR allows for more localisations to be detected, and because fewer clusters and localisations were rejected in the further filtering steps, the ATTO643 allows for faster accumulation of localisations (Figure 3.7B). The average binding event duration (after filtering) was comparable in both cases (approx. 60 ms).

The ATTO643 imager also showed a faster convergence of the fitted segment radius (Figure 3.7C) than the ATTO647N imager. When plotting the same data with the number of localisations on the x-axis, both curves overlap, suggesting that the final convergence radius would be equivalent in both cases (not shown).

3.4.4 Speed advantage through fluorogenicity

Using the much shorter ATTO643-BMNQ1 6 nt fluorogenic imager, we could perform DNA-PAINT measurements at 20ms exposure time (a factor of 10 smaller than the previous protocols using the P3 imager). The higher imaging concentration (20 nM in our case instead of 5 for the P3 imager) allows raising the on-rate of the 6 nt imager to 1.19 s^{-1} ($\pm$ 0.02 s^{-1}, calculated from localisations per cluster after filtering, Figure 3.8A), about 6x more than we observe for the P3 imager (0.196 $\pm$ 0.001 s^{-1}). Over the period of image acquisition, the segments sampling increases steadily, and fits of the segment radii converge eventually to their true value (within the error margins affected by the localisation precision) of 16 nm ($\pm$ 1 nm) for the PB1 segment imaged by the 6 nt and 13 nm ($\pm$0.5 nm) for the NA segment imaged by P3 (Figure 3.8B). Notably, the radii could be extracted after imaging of $\approx$ 200 binding events per segment, which required $\approx$ 800-1000 s of imaging with the P3 imager, and only $\approx$ 150 s of imaging with the 6 nt imager. The use of the 6 nt fluorogenic imager improved the imaging speed by a factor of $\approx$ 6, purely using established experimental protocols and published imager sequences.

It is difficult to separate the effects of fluorogenicity and sequence optimisation: Without optimising the sequence, 20nM might not have been enough to speed up on-rates sufficiently to allow for faster accumulation of binding events, especially given the naturally lower on-rate of a shorter ssDNA. We are now operating at the maximum concentration which our surface permits (before non-specific interactions introduce too much spurious localisations), and predict that for a further speed improvement, we would require higher operational concentrations which might be feasible in combination with passivated surfaces. The elevated concentration of the 6nt imager (4x higher than P3) should have sped up the on-rate by a factor of four (assuming linear concentration dependence),

which is facilitated by the fluorogenic nature of the imager. The optimised sequence at the same concentration as the P3 imager (5 nM) would have given an event rate of approx. 0.3 s^{-1}, which is 50% higher than observed for the P3 sequence (approx. 0.2 s^{-1}). However, even at 5 nM, we would have required fluorogenicity to suppress the non-homogenous background introduced by free imagers at an exposure time of 20 ms. Overall, the speed improvement is consequently due to the increased rate of accumulation of localisations when using the fluorogenic 6nt imager, which is equally facilitated by faster imaging speed and faster turnover kinetics.

Aside from speed, the achievable resolution is another key factor to bear in mind when optimising super-resolution protocols. An experimental estimate for the resolution is difficult to obtain in our experiments: We do not have two target sites at a defined separation, which we could try to resolve (like in many origami-based studies)[11,13,38,53,54,81]. We have some insight into how robust (and therefore precise) our imaging is: These radius values are reproducible with <1 nm precision when localisations of each cluster are randomly split into two sub-sets and the analysis is repeated on those separately. It is thus interesting that we observe different radii for the different imagers we used. The radii of all eight segments when imaged with the canonical P imagers converge to 13.5 ± 1 nm (data of a co-worker)[15], the 6 nt imager consistently shows a larger width of 16 ± 1 nm. An additional 3 nm in width would be consistent with the three different binding sites of the 6 nt imager (see Figure 3.3B): The outermost position of the imager would be 6 nt away from the hybridisation point of the P3 imager. ssDNA with this length and a persistence length of 1-1.5 nm would exhibit an end-to-end distance of approx. 3 nm (as calculated using the WLC model[60]). Whilst such a systematic error is at a first glance reducing the accuracy of the measurements obtained using the fluorogenic imager, the fact

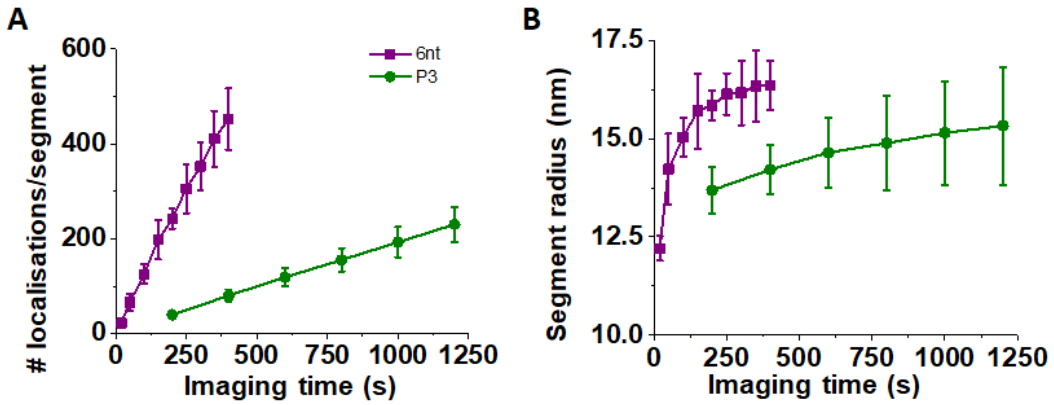

Figure 3.8: DNA-PAINT on viral particles using 6 nt imagers. A: Localisations per Segment. B: Segment radii, fitted to the extracted segments. Error bars are the standard deviation from three independent experiments.

that we can so reliably detect this discrepancy, allows us to correct for it and shows that we are sensitive to structural changes of approx. 3 nm.

As an alternative, Fourier Ring Correlation can aid in estimating the resolution within our data which takes both localisation precision and labelling/sampling density of the image into account:[88,89] The localisation data is split into two (statistically) independent subsets, which are transformed into Fourier-space. The correlation function between both is large for small spatial frequencies (dominated by large features in the image), but decreases with increasing spatial frequencies, until eventually converging to zero when noise in the image becomes dominant. The frequency at which the correlation function first crosses a certain threshold can be transformed into a distance in the original image-space and gives a measure for the achieved resolution in the image.[88,89].

3.5 Conclusion

Overall, our fluorogenic strategy allows us to generate plug-and-play level solutions to introduce fluorogenicity into experimental designs. To demonstrate the ease of implementation of such solutions into existing protocols, we performed DNA-PAINT imaging on influenza A viral segments with a 6 nt long, fluorogenic imager and showed that we can not only recover the physical dimensions far below the diffraction limit, we did so faster than in the initial viral imaging protocol using a non-fluorogenic imager. To achieve this, we relied on imager sequences published previously and simply added fluorogenicity. We are aware of the fact that the used sequence was speed-optimised, unlike the P3 sequence in the "old" protocol. The particular focus of this chapter was to demonstrate the adaptability of the fluorogenic probes to an existing protocol — and to highlight the speed advantage in DNA-PAINT relative to that existing protocol. Overall, the speed improvement is possible because of the delicate interplay between imager binding kinetics and frame rate - without the optimised sequences, hybridisation kinetics of the imager might have been limiting the imaging time, without the fluorogenicity in the imager, it would have been the minimum exposure time required for motion blur.

Our fluorophore and quencher choice focuses on allowing sufficient de-quenching in the hybridised state of an imager as short as 6 nt, which eliminated the need for long imagers as previously postulated.[36] Our approach is translatable to other spectral regions and does not rely on specific fluorophores or sequences. The fluorogenicity allowed us to image with shorter exposure times (20 ms instead of 200ms) at higher imager concentrations (20 nM instead of 5nM), allowing for faster accumulation of binding events and therefore image reconstruction.

DNA-PAINT uses PSF fitting to obtain precise localisations for every emitter, a process which is much more sensitive to (in particular non-homogenous)

background than e.g. the SMF assays we performed in chapter 2. Thus, fluorogenicity of imagers was required to perform good-quality imaging even at concentrations of 20 nM, which in other assays might be operational without fluorogenicity. More generally, the background reduction will improve the SNR at any concentration, so is not only worth consideration for experiments performed beyond the 100 nM concentration barrier.

In summary, we could demonstrate super-resolution imaging of viral genome segments with a fluorogenic 6 nt long imager strand. Through increasing the imager concentration whilst shortening the exposure time, the imaging process could be sped up by a factor of six.

4

Bleaching-resistant, near-continuous single-Molecule fluorescence and FRET

Contents

The work presented in this chapter has been published in: **Bleaching-resistant, Near-continuous Single-molecule Fluorescence and FRET Based on Fluorogenic and Transient DNA Binding**, M. Kümmerlin, A. Mazumder, A. N. Kapanidis, *ChemPhysChem* 2023, 24, e202300175.

4.1 Addressing the Achilles heel of SMF: Photobleaching

Single-molecule methods have transformed the study of biological systems by enabling detailed interrogation of the structure, dynamics, and function of individual molecules.[1] Since the dawn of single-molecule methods, many of the original teething troubles have been addressed and the scope of SMF has drastically increased.

Most SMF methods (and more generally, fluorescence microscopy), however, are still severely limited by photobleaching, which is the irreversible photo-destruction of the fluorophore used to label the bio-molecules of interest. These limitations have been evident since the early days of SMF.[90,91] Due to photobleaching, the photon budget per fluorophore (i.e., the number of photons emitted before the end of the observation) remains limited, and restricts observation time to the low-minute timescale.[92,93] This limitation remains, despite significant improvement through the use of fluorescence stabilisation systems (such as oxygen scavengers and triplet-state quenchers).[94–98]

A possible way to overcome photobleaching is to exchange the fluorescent labels during an ongoing experiment. This can be achieved using transient or reversible interactions between the target molecule under study and the fluorophore, provided that the system allows for an exchange of an attached fluorescent probe with a new probe before the attached probe gets photo-bleached (Figure 4.1A). Exchanging bleached fluorescent labels with fresh ones has been explored for self-healing and regeneration of DNA nanostructures,[99] where an incubation with fresh "staple" strands repaired the effects of photo-damage to fluorescently labelled staples. Further, transiently binding fluorophores have been used to study targets for extended periods, especially in SMLM, with an early example

being the method of PAINT.[24] Such transient binding was also used in DNA-PAINT, where short labelled DNA strands ("imagers") bind to complementary "docking strands" on target biomolecules such as DNA nanostructures[11] and proteins.[53] Exchanging fluorescent labels has also been combined with STED microscopy to avoid the effects of photo-bleaching.[20,100]

To achieve super-resolution, methods like DNA-PAINT require temporal separation of the individual signals from within a diffraction-limited area and thus need extensive "dark intervals" (i.e., during which the target is not bound by a transient label, and thus is not fluorescent). Consequently, these methods cannot provide the continuous signal needed to monitor the presence or motions of a molecular target over extended observation spans.

In principle, the dark interval between two transient labels binding to the same target can be decreased by increasing the rate of binding, either by increasing the concentration, and/or changing the properties of the transient label to increase the on-rate constant. However, in a diffraction-limited TIRF experiment, the concentration of fluorescent transient labels cannot be increased much above 100 nM, as unbound labels contribute to the fluorescence background and degrade the SNR of the measurement.[18,20–22] Higher concentrations of fluorescent species have only been used in combination with STED microscopy (where the effective excitation volume is decreased below the diffraction limit)[100,101] and when fluorogenic probes are used.[36,38,102]

One approach to generate continuous fluorescence over long time spans is to multiplex binding sites for transient DNA labels and optimise binding/unbinding kinetics, which can allow for single-particle tracking for hours.[103] Whilst this approach is attractive for SMF measurements with a single fluorophore, it is incompatible with smFRET studies, where the multiple binding sites on the docking DNA strand will create an uninterpretable range of potential

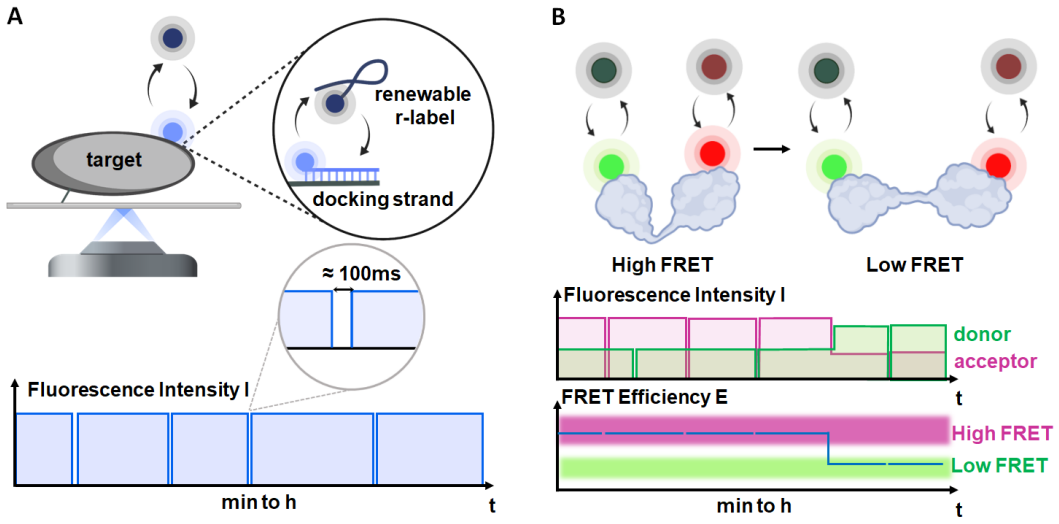

Figure 4.1: The principle of renewable emission via fluorogenic and repeated ssDNA hybridisation (REFRESH). A. Continuous exchange is facilitated by transient hybridisation of short, fluorogenic ssDNA probes (r-labels) to complementary docking strands bound to a target molecule of interest (top). The schematic fluorescence trace (bottom) shows how, if intervals of exchange are short (below or on the order of the frame rate), a near-continuous fluorescence signal can be observed. B. REFRESH-FRET: The same labelling strategy is now applied to donor and acceptor dyes attached to a target of interest which undergoes conformational changes. The observed donor and acceptor traces (middle) can be used to calculate FRET efficiencies (bottom) and monitor conformational dynamics.

FRET-efficiencies. A recent approach built on the concept of "dye-cycling" by implementing it on only a single binding site, thus enabling extended smFRET experiments on holliday junctions (HJs) using the reversible binding of fluorescently labelled 9-nt-long ssDNAs carrying either a FRET donor and a FRET acceptor ("cyclers").[104]

However, despite measuring in an SNR regime that did not allow resolution of the dynamics of the HJ, the maximum concentration of transient fluorescent labels was limiting the temporal sampling to only $\approx 50\%$ per cycler, and thus having single-molecule targets spending only $\approx 25\%$ of time in a doubly-labelled state, during which FRET measurements could be performed.[104]

The limitations of the past studies vividly highlight that the fluorescence background due to unbound labels is the main bottleneck in achieving continuous fluorescence traces. We address these limitations by introducing a transient binding approach that optimises background suppression and label exchange to enable near-continuous, bleaching-independent single-molecule fluorescence observations via **R**enewable **E**mission via **F**luorogenic and **Re**peated **s**sDNA **H**ybridisation (REFRESH, Figure 4.1A). We also extend this approach to smFRET (REFRESH-FRET, Figure 4.1B). In both cases, the target biomolecule is modified with a short ssDNA docking strand which is recognised by a labelled complementary DNA (a "renewable label" or "r-label"). Importantly, our approach involves the design of fluorogenic r-labels that enable measurements in high concentration regimes which allow for continuous (or near-continuous) emission of fluorescence from a target biomolecule with both high temporal resolution and extended observation span (>1 hr, Figure 4.1A, bottom).

We show that we can specifically label two sites within a molecule and enable smFRET measurements over the same period. Finally, we show that transient labelling is fully compatible with dynamic bio-molecules by monitoring the conformational dynamics of HJs using long-lived smFRET measurements. Our strategy can be easily tuned to adapt its temporal resolution and observation span to a plethora of biological systems and applications.

4.2 The photophysics of bleaching

The process of photo-bleaching is induced by chemical reactions of the fluorophore in the excited state: Upon excitation by incoming laser light, electrons in the fluorophore are excited into higher states (mainly the S_1) from which they return to the ground state (S_0) by emitting the later detected fluorescence photon (see Jablonski-diagram in Figure 4.2). The number of photons which can be detected from each molecule ("photon budget") is determined by the excitation laser power and the exposure time in conjunction with the quantum yield, which is dictated by the kinetic rates of all possible de-excitation transitions of the respective electron. These involve de-excitation via fluorescence (k_{fl}), but also non-radiative decay processes (k_{nr}) inter-system crossing into the triplet state T_1 (k_{isc}), and from there permanent transitions into non-fluorescent states (red arrows). The latter process is called photo-bleaching and, due to the cycling of electrons between excited and ground state, will eventually occur for all fluorophores.[105]

There are several factors playing into the process of photo-bleaching, and most of them have been addressed in efforts to increase dye lifetimes. Photo-bleaching is commonly induced by a reaction of F* with electrons in long-lived triplet states with molecular oxygen or free radicals, which are produced by O_2 in the buffer solution.[105] One focus of photo-stabilisation systems is thus the removal of O_2 from the dye environment. Many systems achieve this by employing enzymes which use up O_2 in the reactions they catalyse, such as the cocktail of glucose/glucose-oxidase/catalase (gloxy), or protocatechuic acid (PCA)/protocatechuate-3,4-dioxy-genase (PCD).[95,96]

The latter does not exhibit a significant drop in pH and is thus more suitable for long-term observations.[97] A third system uses glucose, pyranose-oxidase, and catalase and showed an even longer stability of pH with a similar photo-stabilisation performance as the other systems.[98]

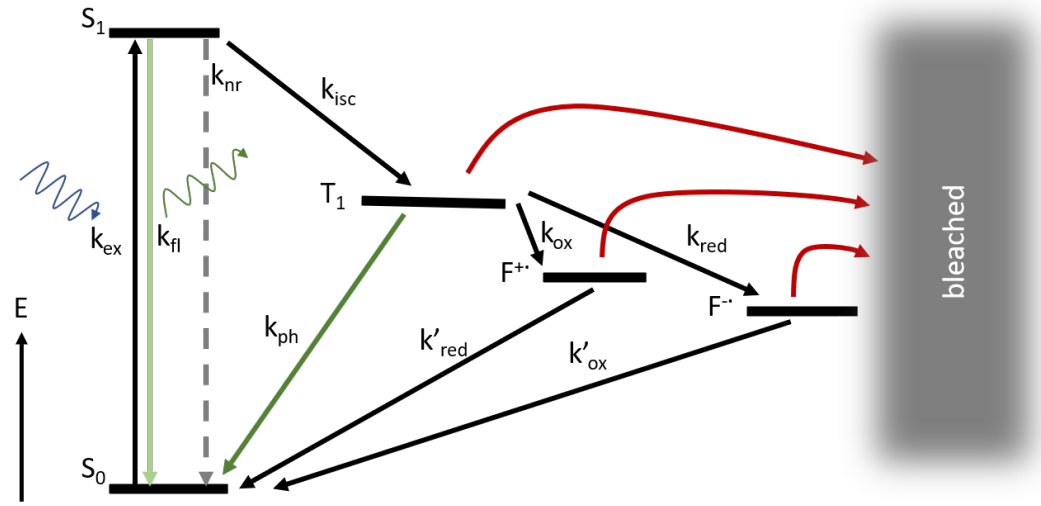

Figure 4.2: Simplified Jablonski-diagram of possible states and transitions for a fluorophore. An electron from the ground state S_0 is excited into the first excited state S1 at a rate k_{ex}, from where it can de-excite emitting a photon (= fluorescence, k_{fl}) or via non-radiative processes (k_{nr}). Competing with this is inter-system crossing (k_{isc}) to the triplet state T_1. From here, phosphorescence can de-excite the molecule back to the ground state (k_{ph}). In the presence of reductants and oxidants, redox reactions into radical-ionic, dark states can occur (k_{ox} and k_{red}). To shorten their lifetimes, these states can be depopulated by complementary redox reactions (k'_{red} and k'_{ox}, respectively). Quickly depopulating the radical ionic and the triplet states reduces not only blinking, but also the chance of photo-bleaching, which usually occurs from these states.[105]

The removal of molecular oxygen from buffers increases the abundance of blinking events, during which the excited electron is stalled in a long-lived triplet state. Oxygen would usually quench this state (by reacting with the triplet state fluorophore, creating singlet oxygen), so that triplet-state blinking would barely affect experiments at time resolutions on the ms timescale. If oxygen is enzymatically removed, an alternative triplet state quencher is required to prevent long blinking events interfering with experiments. Trolox, a vitamin E derivate, is commonly used as a triplet quencher and, in combination with oxygen scavenging, has been effective at extending observation time spans.[105]

Finally, the electron in the excited state is susceptible to redox reactions (k_{ox} and k_{red}), which generate non-fluorescent radical ions. Especially the singlet-oxygen

produced in reaction with the triplet fluorophore is a common reaction partner. As a consequence, the fluorophore is at least temporarily dark. To "re-cycle" those ions into functional fluorophores, mild oxidising and reducing agents can be added to buffers, which restore the ground state via the complementary redox reaction.[106] Quickly depopulating the radical ionic and the triplet states reduces not only blinking, but also the chance of photo-bleaching, which usually occurs from these states.[105]

The implementation of oxygen scavengers, triplet state, and redox quenchers can thus increase the lifespan in *in vitro* experiments, but ultimately cannot permanently prevent photo-damage and bleaching.[105]

Despite having some room for optimising the quantum yield as well as the illumination and detection conditions, the photon budget of a fluorophore employed in single-molecule experiments remains essentially limited by photo-bleaching. The information obtained in single-molecule studies about the position or distance of labelled molecules critically relies on the number of photons collected per frame, the length of which in turn determines the temporal resolution of dynamic processes. By limiting the photon budget, photo-bleaching, even in the presence of stabilisation systems, thus remains one of the major limitations for fluorescence-based single-molecule experiments.

4.3 Design principles for REFRESH

A full description of all experimental procedures can be found in the appendix.

4.3.1 Fluorogenic strategy

To keep the dark intervals low, our technique relies on using high concentrations of unbound labels (100 nM – 1 μM). This, in turn, leads to a significant fluorescence background which needs to be suppressed beyond the level offered by TIRF microscopy (with concentrations up to 100 nM).[18,20–22] To further suppress the fluorescence background, we require fluorogenic probes to deliver fluorophores to their designated targets.

This particular aspect of the REFRESH technique inspired the main theme of this thesis and lead to most of the work presented in other chapters. The fluorogenic strategies presented here thus pre-dates the findings and partially differ from the strategy in the remaining work presented in other chapters. Following from the limited SNR gain (equivalent to the FF in the characterisation chapter but measured differently) in the red label and the need for a longer sequence in the green label, we searched for alternatives and tuning strategies for the fluorogenicity.

Red acceptor label

For a red label, we use a short ssDNA labelled with two ATTO647N fluorophores (one on either end) that exhibit contact-mediated quenching in solution (see Figure 4.3); when bound to the target, the state of quenching is lifted, leading to the appearance of fluorescence corresponding to two ATTO647N fluorophores.[20]

To characterise the level of fluorogenicity, we performed ensemble measurements, assessing the fluorescence of the quenched r-labels in absence and presence of up to 100-fold excess of complementary DNA.

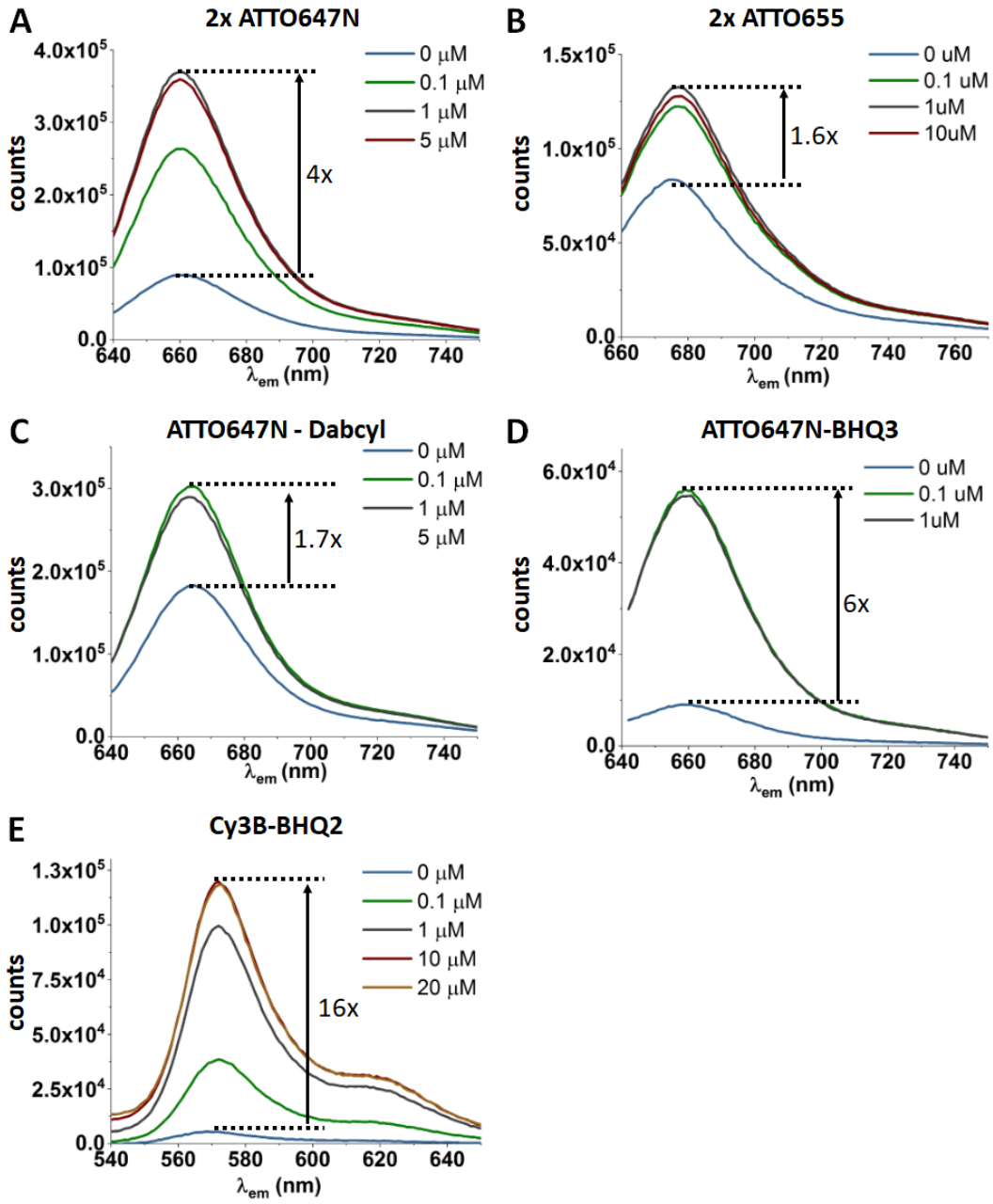

Figure 4.3: Characterisation of de-quenching of r-label strands upon titration with complementary strands. Fluorescence spectra of probes terminally labelled with two ATTO647N (A), two ATTO655 (B), ATTO647N and Dabcyl (C), ATTO647N and BHQ3 (D), or Cy3B and BHQ2 (E) at various concentrations of complementary ssDNA.

We tested a construct terminally labelled with two ATTO655, two ATTO647N, and ATTO647N and BHQ3 or Dabcyl. All constructs were 11nt long, except the ATTO655 labelled probe, which had a length of 8 nt. The emission spectra (Figure 4.3A-D) were recorded in presence of 0 to 20 µM complementary DNA (complementary DNA was added until the fluorescence signal saturated). Upon hybridisation, the increased stiffness of dsDNA forces the dye-dye interactions apart and thus should de-quench the probes.

All red r-labels (Figure 4.3A-D) show an increase in fluorescence upon addition of an increasing concentration of complementary DNA, most prominent the 2xATTO647N (A) and the ATTO647N-BHQ3 (D) probes (4-fold and 6-fold increase, respectively). The level of fluorescence in the ATTO647N-BHQ3 probe is, however, still lower than the fully quenched 2xATTO647N. We reasoned that there is significant FRET from ATTO647N to the BHQ3 even in the hybridised state, which prevents fluorescence emission and thus renders the probe unsuitable for our purpose. For further single-molecule experiments, we selected the 2xATTO647N r-label as a red label, since it proved to be the most suitable out of the tested selection. It also effectively makes the r-label (as a unit) more photostable, since complete loss of fluorescence requires bleaching of both fluorophores and thus will require more time to occur.

Green donor label

For the green label, we have used r-labels that contain a pair of a green fluorophore (Cy3B) and BHQ-2, which serves as a non-fluorescent FRET acceptor to the Cy3B fluorescence in the unbound r-label. To allow for sufficient fluorogenicity in the bound state, we use an extended r-label length of 15 nt with mismatches between r-label and docking strand, as was done recently for fluorogenic DNA-PAINT imagers.[36] For the green r-label, we observe a 16-fold increase in fluorescence intensity upon hybridisation (Figure 4.3E), which suggests that

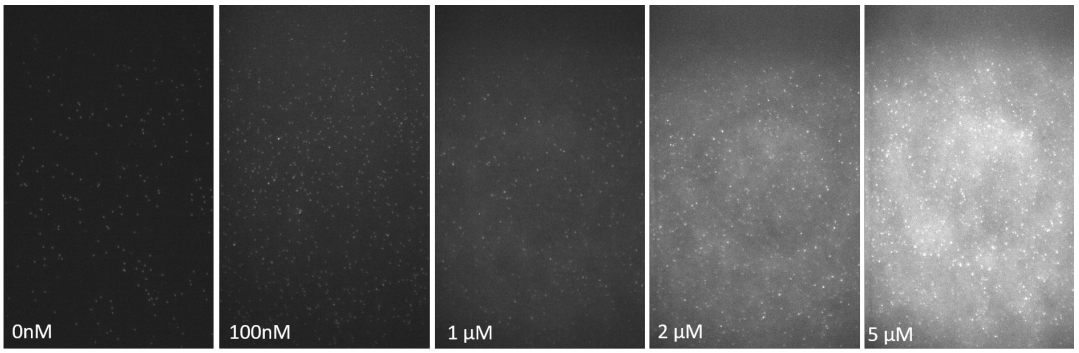

Figure 4.4: Individual frames imaged at various concentrations of green r-labels (0-5 µM) in the imaging buffer. At 0 nM, the observed spots come from immobilised Cy3B. The subsequence images show spots of green r-labels at various concentrations binding to complementary, immobilised docking strands. Through the fluorogenic nature of the r-lables, individual targets can still clearly be identified at 5 µM of r-lables in the imaging buffer.

indeed increasing the distance between dark quencher and fluorophore in the de-quenched state (compared to the ATTO647N-BHQ3 pair) is allowing for strong emission once hybridised with complementary DNA. This allowed for imaging of single-molecule binding sites using a TIRF microscope with up to 5 µM r-label (see Figure 4.4).

4.3.2 Sequence selection

The Sequences of the r-labels – vital to providing the desired binding kinetics — were chosen as follows: for the initial sequence (red r-label), we selected a DNA length of 10-12 nt to provide a "bound time" that is long enough to ensure efficient use of the photon budget of the fluorophores, and short enough to avoid photo-bleaching in the bound state (which, for a single ATTO647N fluorophore, is described by $k_{bleach} = 0.003\ s^{-1}$ under continuous excitation by a laser power of 1.4 mW at 640 nm, Figure 4.5). Broadly speaking, k_{off} has to be 10-100 fold larger than k_{bleach}, and k_{on} should be 10-100-fold larger than k_{off}.

The ultimate goal of a high on-rate (which minimises dark periods) could be facilitated by a high r-label concentration, but could also be influenced by the

sequence: repetitiveness in sequence (e.g., consistent of repeats of a three-base motif) combined with a longer sequence have been shown to increase the on-rate.[54] We also avoided interactions within the sequence by choosing just two non-complementary bases per sequence (e.g., only thymine (T) and guanine (G)), and estimated ΔG values from Santa Lucia et al.[107], and on-rates for DNA hybridisation using an algorithm by Zhang et al.[108] From this, we calculated off-rates for approximately thirty sequences and analysed the impact of G/C content, label length and sequence composition. Starting from the observed bleaching rate ($k_{bleach} = 10^{-3}$ s^{-1}), we defined a range of suitable off-rates (approx. k_{off} = 10^{-2} - 10^{-1} s^{-1}), and in that range looked for the sequence with the highest on rate. Within the sequences we tested, this was a T-only 12mer, which we thought difficult to implement for FRET, because hybrids shifted by a few bases could still form a relatively stable hybrid - but could introduce a multitude of different FRET-states into our measurements. We instead experimentally tested two similar, but not as homogenous sequences (5'-TTT GGG TTT TT-3' and 5'-TTT TGT TTT TTT-3') and eventually chose the first, which had much higher on-rate than the second, and few 100 nM would suffice for continuous fluorescence traces. Specifically, the red r-label showed a mean t_{off} of $\approx$ 3.3 s (or $k_{on} \approx$ 0.30 s^{-1}) and a mean t_{on} of $\approx$ 15 s (or $k_{off} \approx$ 0.07 s^{-1}) at 20 nM.

For the second r-label sequence, we built on the fluorogenic DNA-PAINT imager sequence design by Chung et al., which extended the imager length to 15 nt and used mismatches between imager and docking strand to reduce bound times and allow for blinking and super-resolution imaging.[36] Starting with their green imager sequence, we introduced a higher degree of complementarity into the docking sequence to prolong binding events. We observed the hybridisation of the green r-label sequence to seven different, partially complementary, and surface-immobilised ssDNAs and evaluated the percentage of frames in which we could detect an r-label being bound at 100nM ("occupancy"). This appeared to

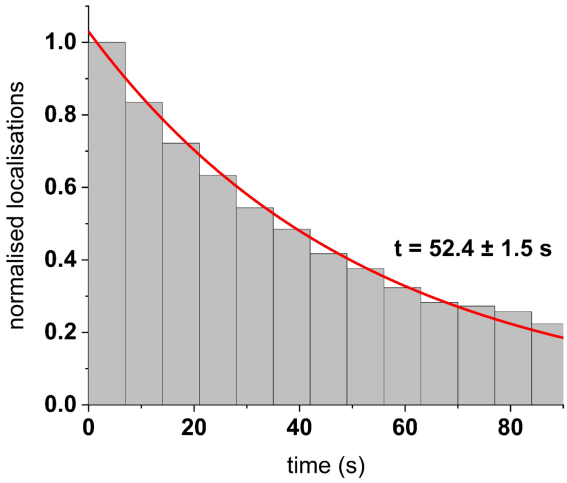

Figure 4.5: Bleaching curve of ATTO647N. Data is obtained from single-molecule measurements under continuous excitation by a laser power of 1.4 mW at 640 nm and fitted with a single-exponential decay using MEMLET.[109]

be an easier measure of how close we are to continuous signals than the lengthy determination of k_{on}, k_{off}, and k_{bleach} we performed for the red r-label. Mean occupancies of the tested sequences ranged from 30-80% at 100mM. The sequence with the highest degree of occupancy was selected (with a mean t_{off} of $\approx$ 12 s (or $k_{on} \approx$ 0.08 s^{-1}) and a mean t_{on} of $\approx$ 22 s (or $k_{off} \approx$ 0.05 s^{-1}) at 100 nM.

To give straightforward numbers for the hybridisation kinetics and allow for easy sequence selection, we have previously calculated mean values of t_{off} and t_{on}, and also the inverse values as k_{on} and k_{off}, respectively. From previous studies, we know, however, that the hybridisation kinetics are indeed better described by a bi-exponential decay with two independent decay constants.[64,65] To further characterise the binding behaviour, we thus fitted a bi-exponential distribution to the dwell times (extracted as described in the main experimental section) of both r-labels using a maximum-likelihood-estimator (MLE) in Matlab (MEMLET[109]). The fitted function takes into account the minimum measurable dwell time (one frame) and the discrete nature of the observable values. Confidence intervals for fitted decay times were determined via bootstrapping (Table 4.1 and Figure 4.6).

Both r-labels exhibited two on-time components, indicative of two hybridisation states.[64,65] The longer one, corresponding to the fully hybridised state in the

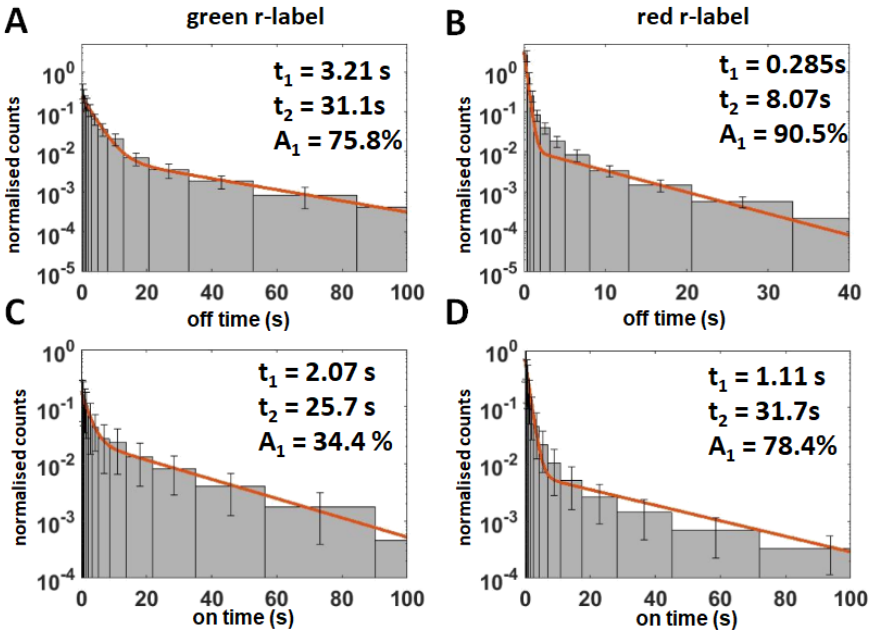

Figure 4.6: Characterisation of the binding kinetics of r-labels. The data was fitted to a bi-exponential distribution using a MLE algorithm in Matlab (MEMLET[109], red graph). For display purposes, the data were binned with increasing bin size, counts were normalised by the bin width. Error bars on bins are derived from bootstrapping (200 iterations).

range of 20-30s, the fast component is about an order of magnitude lower, 1-2 s. Interestingly, the green r-label which was designed to contain mismatches in the sequence, has a higher proportion of binding events being described by the long component than the red r-label. Off-times have a dominant component in the low second-range, suggesting that already at 100nM, a fast exchange is possible. This is particularly true for the red r-label, where this is in the sub-second range (0.3s).

Table 4.1: Parameter mean and 95% CI from bootstrapping (200 iterations) the binding kinetics of the r-labels.

label	state	parameter	mean	lower 95% CI	upper 95% CI
green	off	percentage t_1	0.757	0.752	0.761
		t_1 (in s)	3.189	3.151	3.227
		t_2 (in s)	31.080	30.616	31.544
	on	percentage t_1	0.341	0.337	0.345
		t_1 (in s)	1.491	1.455	1.528
		t_2 (in s)	24.907	24.706	25.108
red	off	percentage t_1	0.905	0.905	0.906
		t_1 (in s)	0.285	0.284	0.285
		t_2 (in s)	8.051	8.005	8.098
	on	percentage t_1	0.783	0.783	0.784
		t_1 (in s)	1.105	1.101	1.108
		t_2 (in s)	31.708	31.571	31.845

4.4 Near-continuous SMF with REFRESH

We first implemented our renewable strategy on a surface-immobilised DNA target containing a docking DNA strand complementary to our respective r-label. The target was also labelled with a Cy3B fluorophore, which served as a localisation signal. During the experiment, we first localised our target using the green emission channel (Figure 4.7A, left); we then added the r-label strands, and recorded movies under red or green excitation (Figure 4.7A, right), which were then used to generate time-traces.

We generated time-traces at different concentrations of the red r-label (Figure 4.7B). They show several intervals of high intensity ($\approx$ 2,000 counts), corresponding to an r-label being bound to the target (blue shading) followed by disappearance of the fluorescence signal (blue triangles), which we attribute to r-label dissociation (and not to bleaching, which would have led to a step-wise decrease in intensity due to the presence of two fluorophores per r-label).

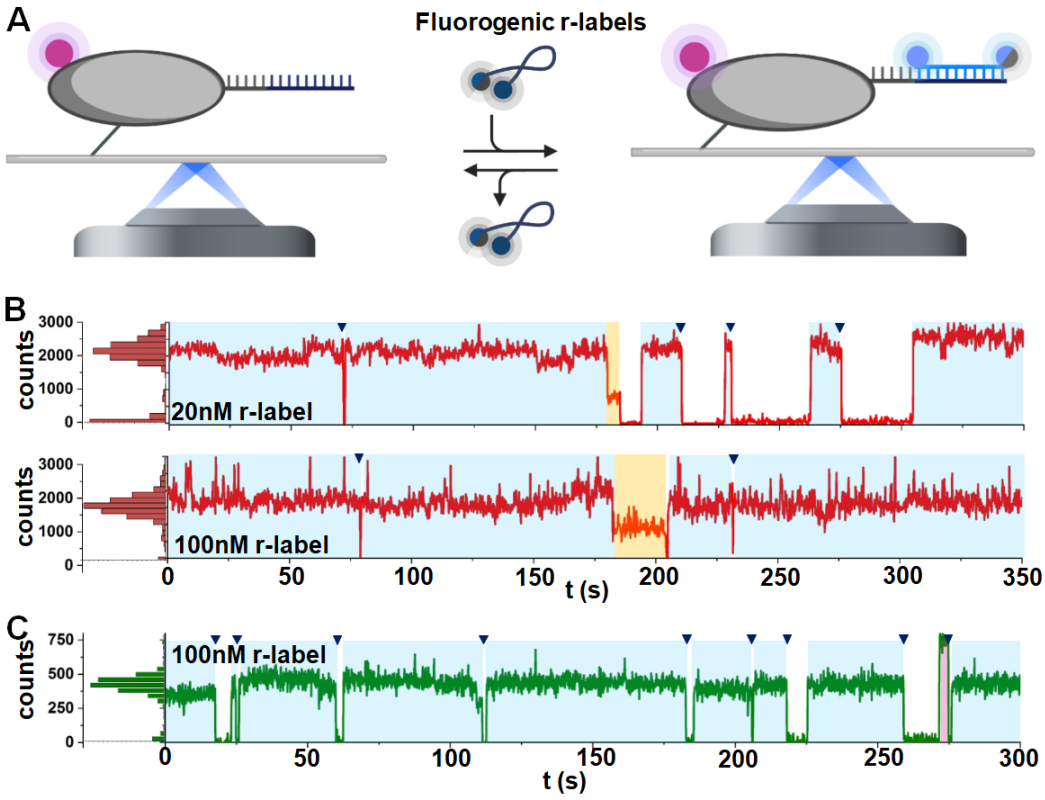

Figure 4.7: REFRESH allows for continuous SMF observations: A. The target molecule is localised on the surface via a localisation label (magenta), observed in an emission channel different from that of the r-labels. After the addition of r-labels (carrying two ATTO647N or Cy3B/BHQ2), binding and unbinding can be observed at co-localising spots. B. Example traces at 20 nM (top) and 100 nM (bottom) red r-label. C. Example traces of 100 nM green r-label. Blue shaded areas: bound intervals of the complete r-label; triangles indicate de-hybridisation; yellow shaded areas: interval with only one emitting ATTO647N; magenta shaded area: interval without functional BHQ2.

As expected, the dark intervals become shorter with increasing r-label concentration (compare Figure 4.7B and C), and for concentrations of >100 nM, become negligible (<2 %, see further traces in Figure 4.8). Occasionally, bleaching of one fluorophore occurs, reducing the fluorescence signal by ≈ 50 %, to ≈ 1,000 counts (yellow shading), which also suggests that de-quenching upon target binding is complete, with no significant impact of any remaining contact-mediated quenching or homo-FRET processes on the quantum yield. Further

decrease to baseline intensity is attributed to r-label unbinding or bleaching of the second fluorophore.

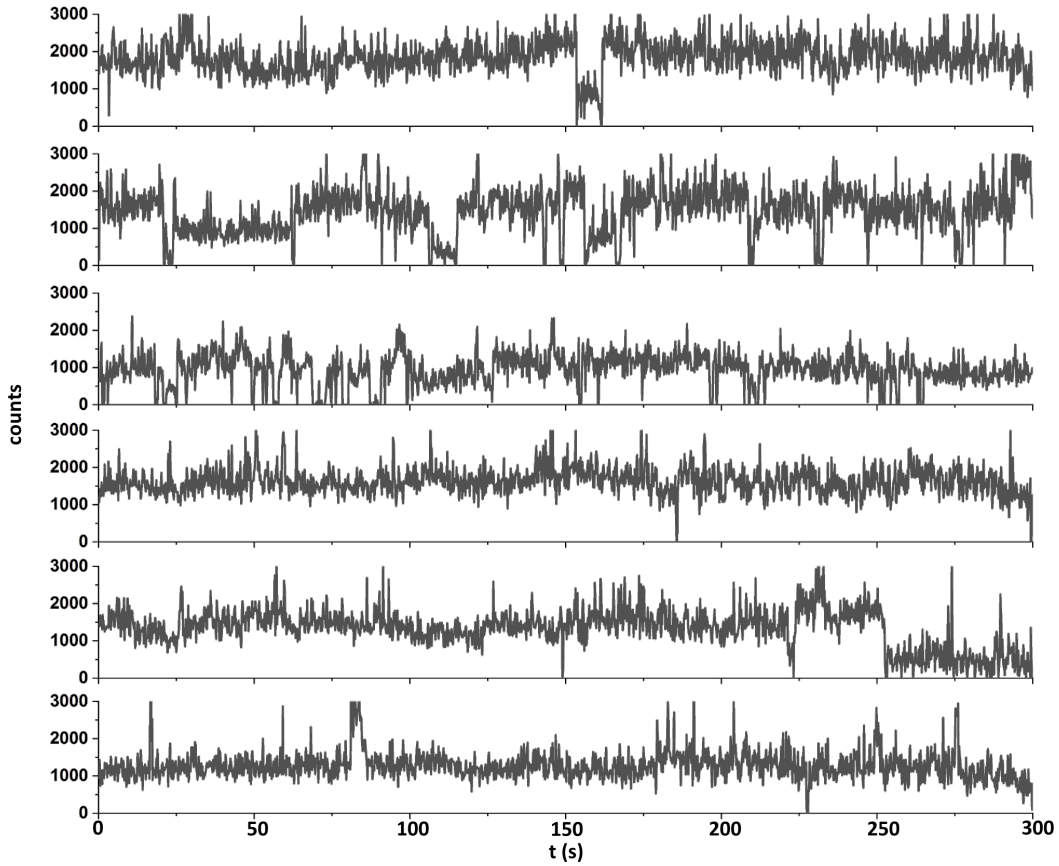

Figure 4.8: Additional traces of the red r-label binding at 100 nM. Repeated binding can be observed by the signal rising to ≈ 1000–1500 counts. Occasionally, the signal shows lower counts (≈ 750 counts), which indicates intervals of only one functional ATTO647N dye emitting.

We performed similar experiments using a target carrying the docking strand for the green r-label. To avoid FRET interactions between localisation signal and r-label, we used a second Cy3B dye as localisation signal, which was bleached before addition of the r-labels. Our traces at 100 nM green r-label (Figure 4.7C, further traces can be found in Figure 4.9) show clear r-label binding events, detected as an increase in signal from background level to ≈ 450 counts (blue shading). We observe a mean bound time of ≈ 22 s (with any dwells shorter

than the 100 ms frame-time being inaccessible), which indicates a turnover faster than for the red r-label.

Occasionally, we observe a signal level of ≈ 800 counts (magenta shading), which we attribute to an r-label without functional quencher (either due to incomplete synthesis or due to temporary quencher blinking process[34]), which thus appears brighter due to the lack of FRET. The observed increased signal in the absence of quenching is consistent with expectations from the 14-bp separation between fluorophore and quencher (≈ 5.5 nm) and the Förster radius between Cy3B and BHQ2 (≈ 6.1 nm).[110] At 100 nM, we observe a temporal sampling of ≈ 70 %. To increase the temporal sampling further, we can increase the r-label concentration to e.g., 300 nM for the following smFRET experiments.

Our results clearly established that we can perform continuous observations on immobile biomolecules using renewable labelling based on the hybridisation of short, ssDNA labels. Importantly, due to constant r-label exchange, the trace length was not limited by the bleaching of individual fluorophores, and since the fluorescence signal was lost for very few frames at a time, we achieved a very high temporal target sampling, which reached up to 98 %.

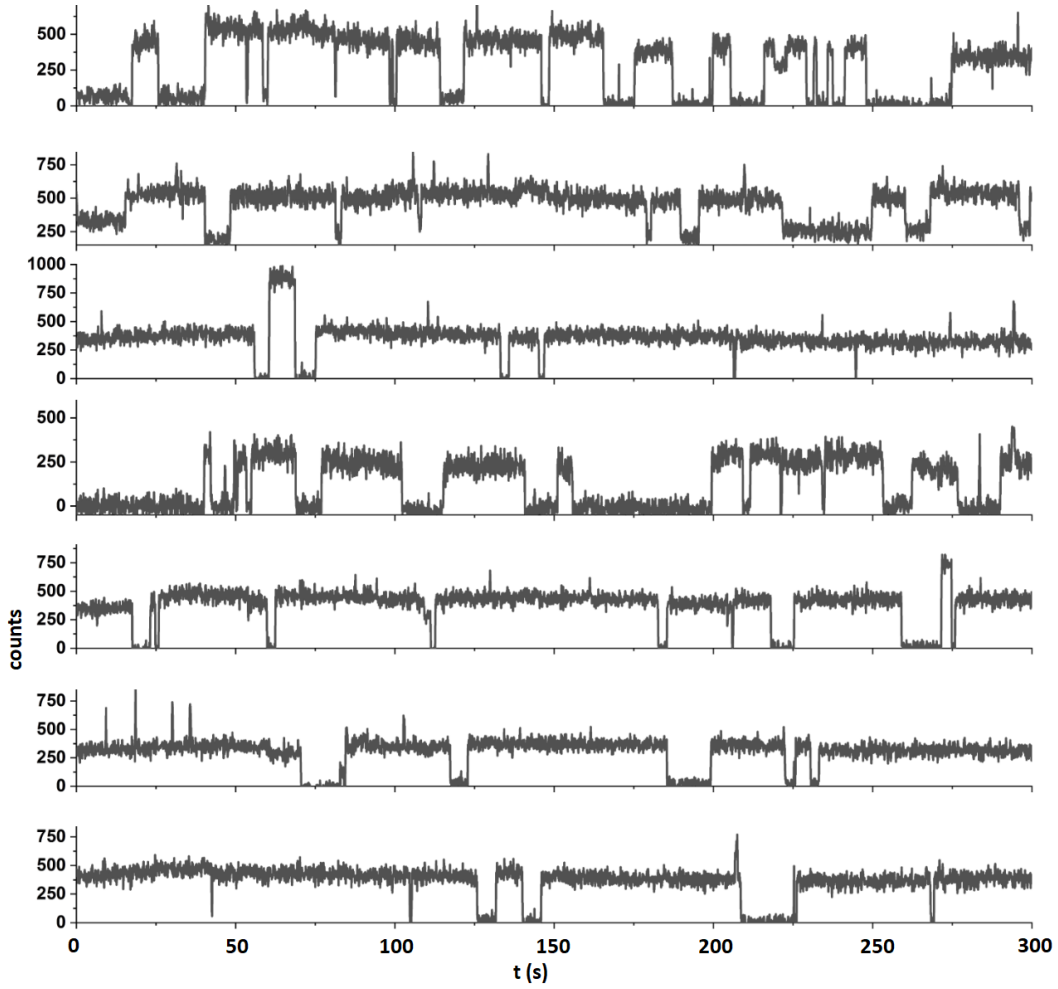

Figure 4.9: Additional traces of the green r-label binding at 100 nM. Repeated binding can be observed by the signal rising to ≈ 450 counts. Occasionally, the signal reaches higher counts (≈ 800 counts), which indicates intervals of Cy3B fluorescence without functional BHQ2.

4.5 Conformational dynamics for hours using REFRESH-FRET

We then moved to the experimental implementation of smFRET measurements using r-labels. As a model system, we chose a HJ, a well-studied, dynamic four-arm DNA structure that allows us to monitor repeated interconversions between two conformational states distinguishable using FRET.[111] We first assembled a "standard" HJ by using four 22 nt-long ssDNA strands, one of which carries a

covalently attached FRET donor and a second carrying a covalently attached FRET acceptor; this labelling strategy results in the fluorophores appearing at the ends of two of the HJ's four arms (Figure 4.10A). In the two main conformational states of this reference HJ, the fluorophores are positioned at very different distances from each other, resulting in two distinct FRET efficiencies (E, a high FRET state of E $\approx$ 0.75 and a low FRET state of E $\approx$ 0.25).

To monitor both FRET and fluorophore stoichiometries, we used alternating laser excitation (ALEX) of the immobilised molecules using 200 ms frame-times (100 ms exposure per channel). For each ALEX frame, the AA signal (emission in the acceptor channel during acceptor excitation) reports on the presence of the acceptor, and the DD and DA signals (emission in the donor or acceptor channel during donor excitation, respectively) are used to observe FRET and conformational changes. Figure 4.10C shows a representative example of a fluorescence trace recorded from the reference HJ: the AA trace shows an intensity of $\approx$ 1,500 counts, and features slow fluctuations between two spectral states of ATTO647N, which have been described before.[112] On the other hand, DD and DA show anti-correlated fluctuations indicating dynamic FRET processes, which are also clearly reflected in the apparent E trace (bottom panel), which shows transitions between high (E $\approx$ 0.75) and low (E $\approx$ 0.25) values.

To implement REFRESH—FRET, we extended the strands carrying the reporter dyes by docking sequences complementary to our green and/or red r-labels. In solution, we provide the required fluorogenic r-labels, which bind specifically to their docking strands (Figure 4.10B). In the two main HJ conformational states, the fluorophores are again positioned at different distances from each other, resulting in two distinct FRET efficiencies. We recorded traces using 100 nM of red and 300 nM of green r-label, and an exposure time of 100 ms/channel/frame (Figure 4.11).

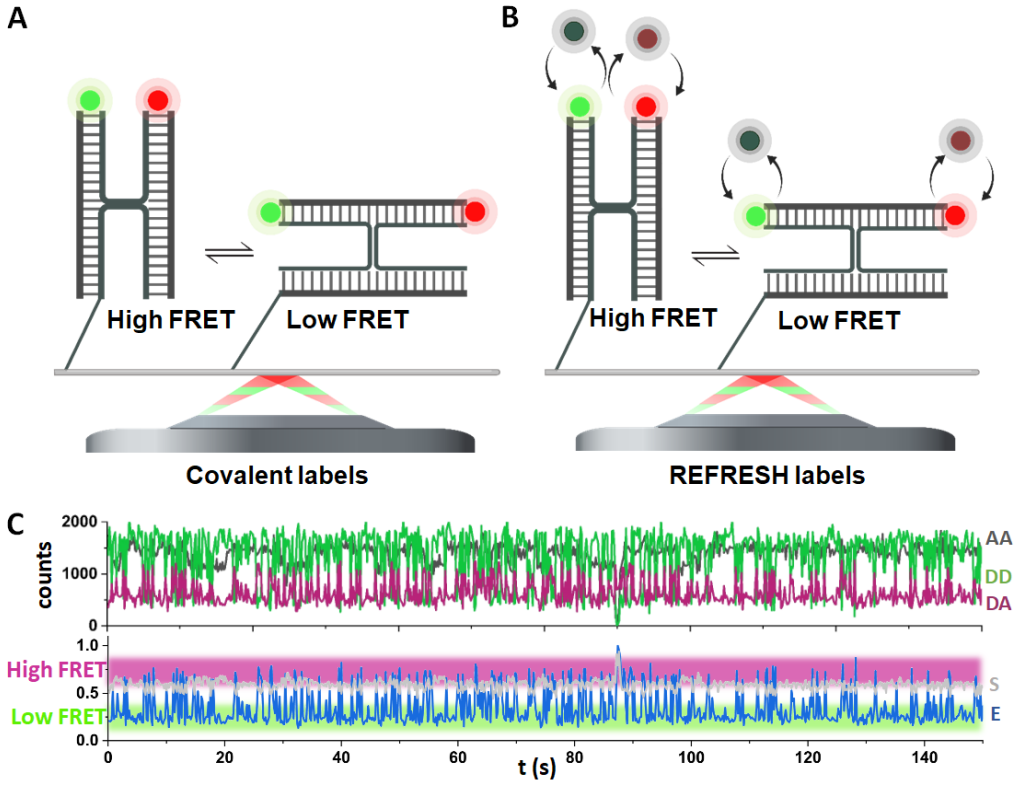

Figure 4.10: Observation of conformational dynamics using REFRESH-FRET. A. Reference structure of a covalently labelled HJ. B. HJ with exchanging labels: The X- and R-strand of the HJ carry extensions, which serve as specific binding site for the fluorogenic r-labels. C. Intensity-vs-time trace of the reference HJ (covalent labels) with AA, DA, and DD signal (top), from which the apparent FRET efficiency (E) was calculated. The anti-correlated fluctuations in DD and DA and the fluctuations in E indicated FRET dynamics between a high-FRET state ($E \approx 0.75$) and a low-FRET state ($E \approx 0.25$).

Upon ALEX excitation, the AA trace in Figure 4.11 specifically reports on the presence of the red r-label, whilst the DD trace reports on the green r-label. The presence of a significant DA intensity (i.e. the FRET signal) is only expected when both dyes are present at the same time and will report on the conformational state of the HJ. The observed time traces show the same pattern of binding events as shorter traces in Figure 4.7, with the additional feature that, whenever both r-labels bind simultaneously, the same anti-correlated dynamics in the DD and DA intensity as with the reference HJ can be observed (zoomed-in

segment, Figure 4.11). The fluorescence fluctuations indicate FRET dynamics, with the E value showing clear transitions between high (E $\approx$ 0.75) and low (E $\approx$ 0.25) values. The FRET efficiencies for the two states are similar to the reference HJ, which validates the choice of the fluorophore location on the r-labels.

Interestingly, the presence of two acceptor dyes on the red r-label does not interfere with these FRET-measurements. Compared to the situation with only one dye, the second acceptor, even if quite far removed from the donor, will add a further FRET de-excitation pathway, overall possibly leading to slightly elevated apparent FRET efficiencies (and might be the reason for the very slight shift in the histograms in Fig 4.13 C vs. D, which is also visible when only the red r-label is used (Figure 4.15C). Once the energy transfer has happened, both ATTO647N dyes are equivalent in their de-excitation pathways (and through homo-FRET can be seen as being in some form of equilibrium), and so emission properties are not expected to be any different to a case with only a single ATTO647N dye. Occasionally, we can observe the system in the presence of only one acceptor dye (e.g. in Figure 4.12, approx. minute 5-8). If it is the proximal dye which bleaches, we lose most of the signal in the DA channel, since FRET to the distal dye is occurring with low efficiency. However, we can afford to lose the distal ATTO647N and can maintain the same ability to monitor conformational dynamics as with two dyes.

Inspection of the traces shows that the AA signal is near-continuous over the recorded period at an r-label concentration of 100 nM, whilst the DD trace shows still periods of time without fluorescence ($\approx$ 20 %).

Since the observation time of the REFRESH-HJ is essentially immune to the photobleaching, we can monitor it for extraordinarily long time-spans. The trace in Figure 4.12 lasts for one hour, several orders of magnitude longer than the bleaching time of the individual fluorophores ($\approx$ 50 s for ATTO647N,

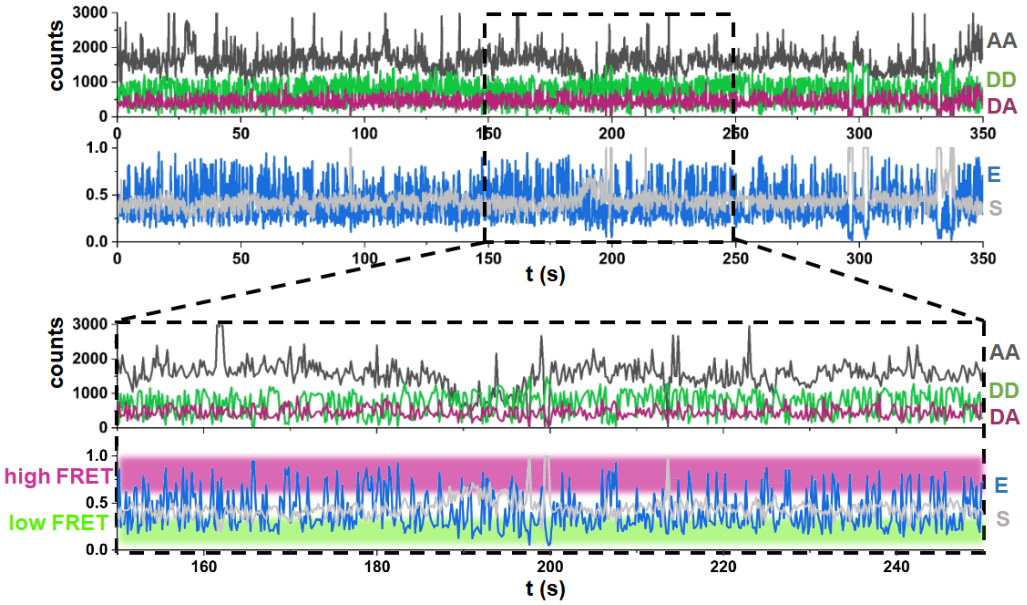

Figure 4.11: Representative traces from the REFRESH-HJ using 100 nM red and 300 nM green r-label. A. Full trace with AA (top), DD, and DA channel (middle) and calculated FRET efficiency (E, bottom). B. Zoom-in of the trace in A. The anti-correlated fluctuations in the DD and DA channels (middle panels) and the fluctuating E trace (bottom) indicate a dynamic interchange between a high-FRET state (E $\approx$ 0.75) and a low-FRET state (E $\approx$ 0.25).

see Figure 4.5. We replaced the buffer in the chamber continuously (with a full volume exchange every 5 min) to replenish the stock of r-labels and the photo-stabilisation system.

For any labelling strategy, it is important to assess how much it influences the system that is to be studied with it - In our case, the HJ. We thus compared the transitions recorded in the traces from the reference HJ with both dyes covalently attached; the two HJs where one dye is supplied by r-labels whilst the other one is attached covalently; and the complete REFRESH-HJ. We used the E traces (see Methods) to generate FRET efficiency distributions and dwell-time histograms for the four different HJs (Figure 4.13, 4.14, and 4.15 for the single r-labels). All structures showed similar FRET distributions, with peaks at E values of $\approx$ 0.25 and $\approx$ 0.75. The relative abundance of the two fractions for the HJ

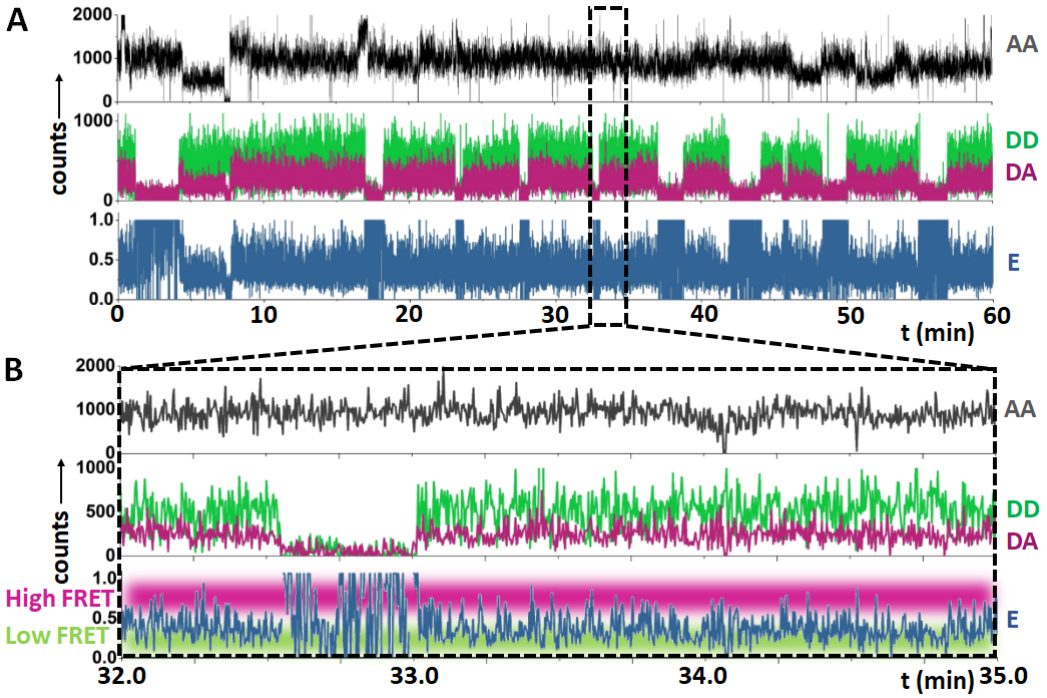

Figure 4.12: Representative hour-long traces from the REFRESH-HJ using 100 nM red and 300 nM green r-label. A. Full trace with AA (top), DD, and DA channel (middle) and calculated FRET efficiency (E, bottom). B. Zoom-in of the trace in A. The anti-correlated fluctuations in the DD and DA channels (middle panels) and the fluctuating E trace (bottom) indicate a dynamic interchange between a high-FRET state (E $\approx$ 0.75) and a low-FRET state (E $\approx$ 0.25).

(reference: low FRET: $\approx$ 70 % high FRET: $\approx$ 30 %, REFRESH: low FRET: $\approx$ 51 %, high FRET: $\approx$ 49 %) indicate an equilibrium constant of $K_{high \rightarrow low}$ $\approx$ 2.3 for the reference HJ, and a $K_{high \rightarrow low}$ $\approx$ 1.0 for the REFRESH-FRET HJ. The relative abundance indicates that the low-FRET state is energetically slightly favoured in the reference HJ, however, the difference between the states is $\approx$ 2-fold smaller when using r-labels. Notably, the shift in the equilibrium when only one dye is supplied as an r-label is much stronger for the red one ($K_{high \rightarrow low}$ $\approx$ 1.2) than for the green one ($K_{high \rightarrow low}$ $\approx$ 2.0), suggesting that the majority of the equilibrium shift is induced by the attachment of the red docking strand and r-label (see Figure 4.15). The r-label concentration does not affect the the FRET populations (Figure 4.14).

We also determined the kinetic constants for the interconversion of FRET states. In the REFRESH-HJ, at 100 nM red and 300 nM green r-label, the interconversion rates were $k_{high \rightarrow low} = 3.45 \pm 0.04\ s^{-1}$ and $k_{low \rightarrow high} = 2.69 \pm 0.03\ s^{-1}$, equating to a $K_{high \rightarrow low} \approx 1.3$. In comparison, the reference HJ showed a $k_{high \rightarrow low} = 5.51 \pm 0.22\ s^{-1}$, $k_{low \rightarrow high} = 1.61 \pm 0.04\ s^{-1}$, and a $K_{high \rightarrow low} \approx 3.4$. These values agree well with the values obtained from the population fitting and further show that, the shift in equilibrium when comparing reference and REFRESH HJ is due to a change in the stability of both states. An interconversion constant $K_{high \rightarrow low}$ near unity is consistent with previously published literature on the HJ: Gilboa *et al.* reported a $K_{high \rightarrow low}$ of ≈ 3.7, while McKinney *et al.* reported a $K_{high \rightarrow low}$ of ≈ 1 across different $[MgCl_2]$.[111,113]

Our results show that, compared to a covalently labelled HJ, the interconversion kinetics and the equilibrium between both FRET states are affected by the addition of our r-labels of their docking sequences. The HJ is, however, a worst-case scenario: Each arm of the HJ is 11 nt long, so we have significantly affected the lengths of the two arms wich carry the r-labels by adding a 11 or 15 nt additon. The structure thus looses its symmetry, and the equilibrium constant together with the interconversion rates suggest there might be some interactions stabilising the high-FRET state, potentially mediated by the extensions. When thinking of translating the REFRESH approach to large (protein) complexes, we would envision these contributions to become less pronounces and potenitally negligable. Any application should, nevertheless, control and check for such labelling effects before drawing conclusions.

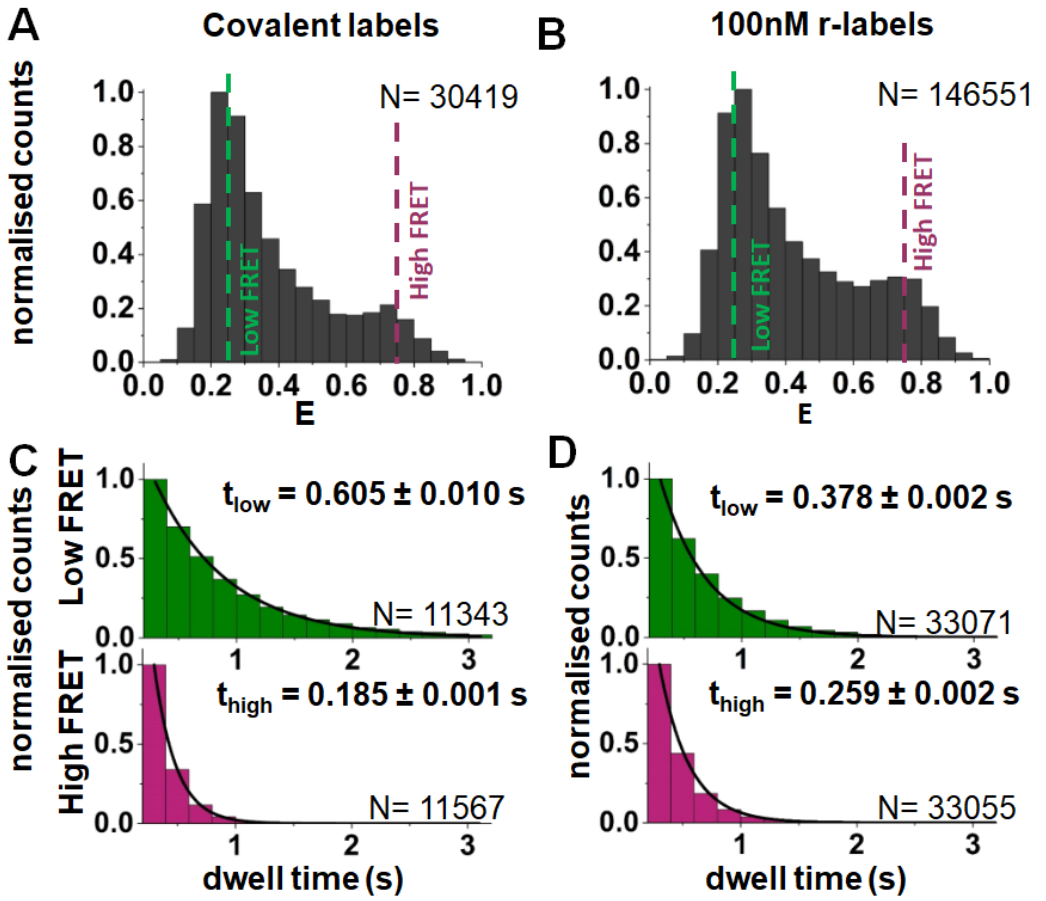

Figure 4.13: Monitoring conformational dynamics using REFRESH-FRET: Representative data from one experiment. A-B. FRET histograms of the reference HJ with covalent labels (A) and the HJ with exchanging donor and acceptor (B). C–D. Dwell time histograms of the high and low FRET states for the reference HJ (panel C; data from 64 molecules), and the HJ with exchanging acceptor label (D; data from 101 molecules), the errors stated are fitting errors. N, number of datapoints across all traces.

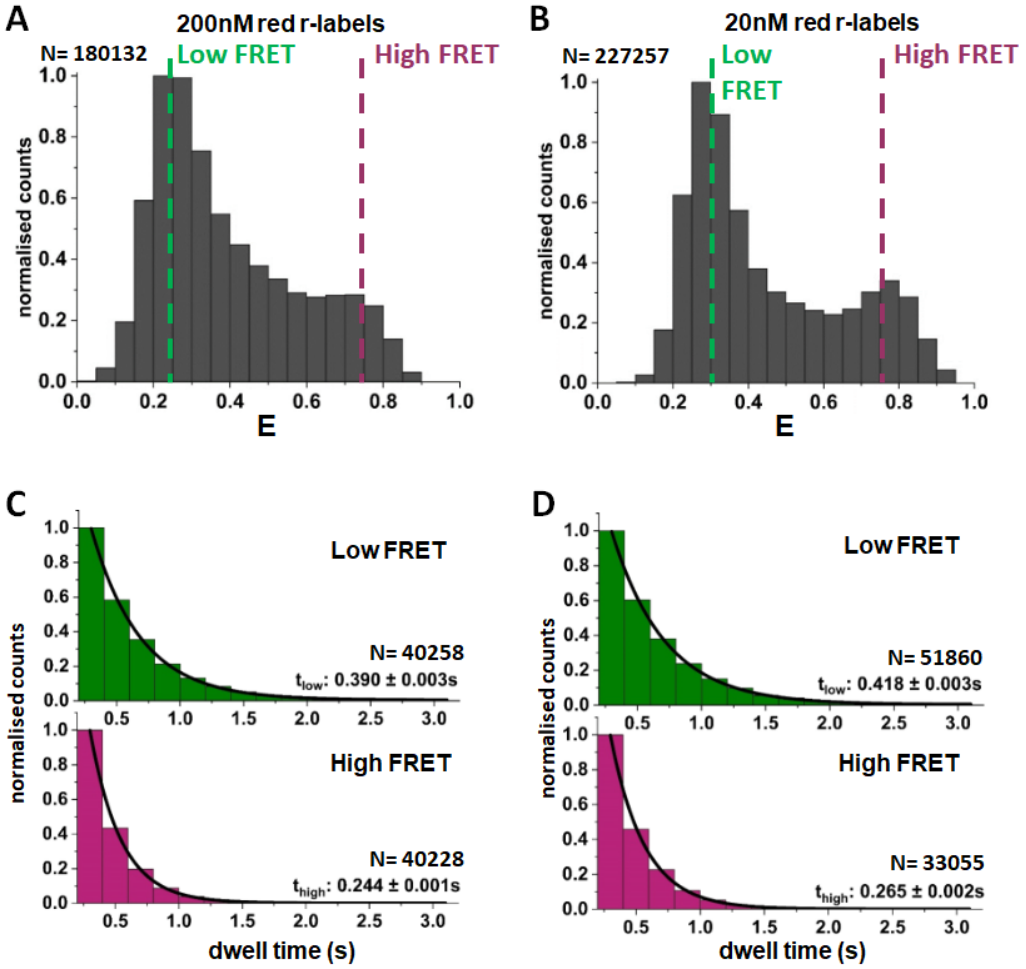

Figure 4.14: Conformational dynamics in the HJ observed with single r-labels at different concentrations. Representative data from one experiment. A-B. FRET histograms of the HJ with covalently attached donor and exchanging acceptor at 200 nM (A) and 20 nM (B). C –D. Dwell time histograms of the high and low FRET states for both HJs, the errors stated are fitting errors. N, number of datapoints across all traces.

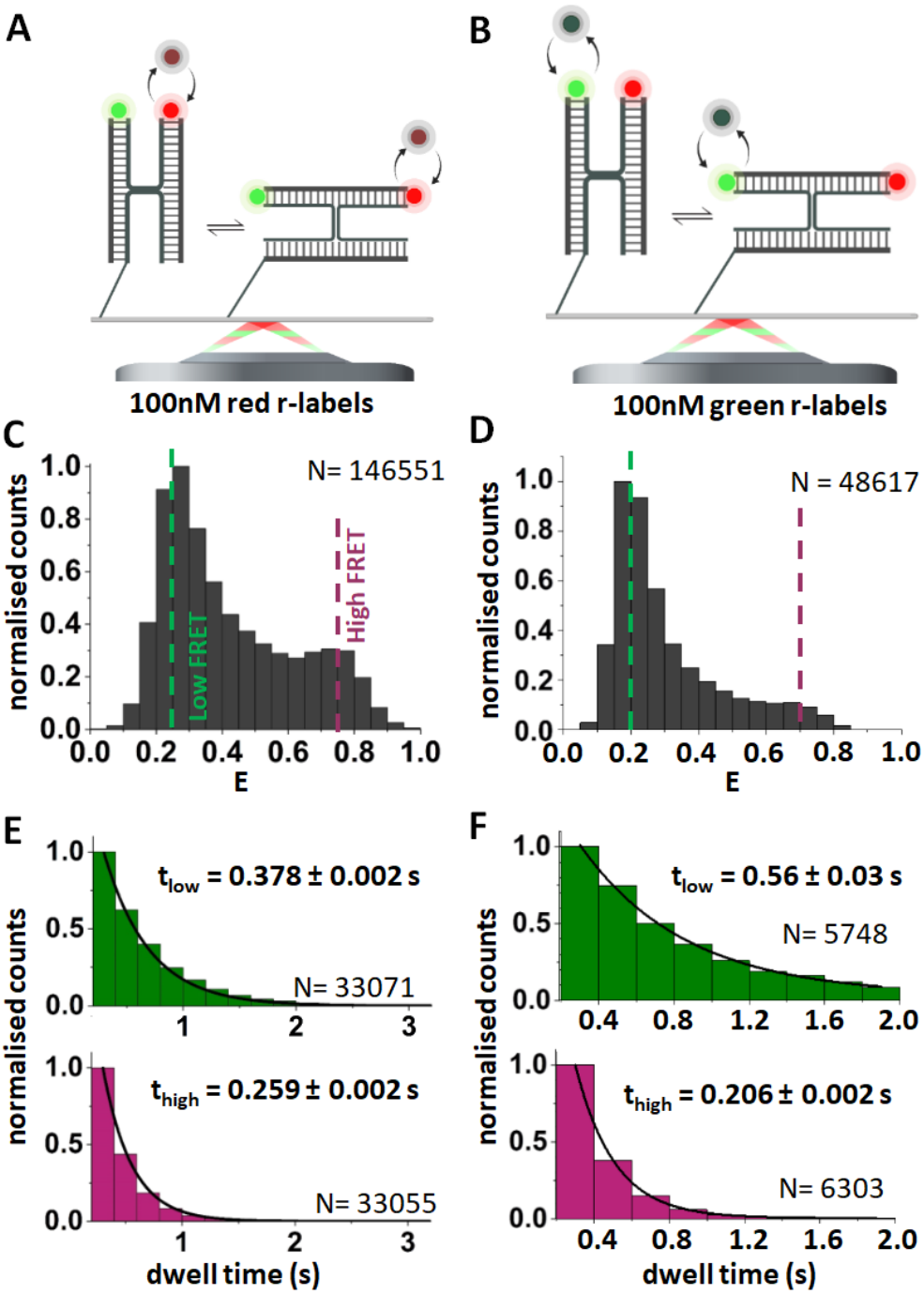

Figure 4.15: Conformational dynamics in the HJ observed with single r-labels. FRET distributions (C-D) and dwell time histograms (E-F) for the HJ with only (A, C, E) or green (B, D, F) r-label, as indicated by the schematics in A and B, respectively. Data 179 (red r-label) and 72 molecules (green r-label). N, number of datapoints across all traces.

Our results clearly establish that we can use REFRESH-FRET to accurately resolve conformational dynamics on the milli-second timescale over observation times on the scale of hours, spanning five orders of magnitude.

Ultimately, the observation time span is limited by the survival time of the target molecule, especially the docking strand. In DNA-PAINT, photo-destruction of docking strands has been reported; however, DNA-PAINT uses 10-25-fold higher laser powers than our experiments.[114] Additionally, DNA-PAINT experiments are often performed without photo-stabilisation, which both preserves fluorescent dyes and prevents damage to DNA structures (such as docking sites or r-labels).[99] Consistent with this, we have observed only a few traces (<5 %) which permanently enter a dark state after some time (or show significant reduced on-times). Using DNA hybridisation to allow for transient interaction provides great tuneability and makes our approach applicable to many experimental conditions: The r-labels are tuneable in terms of length and sequence which enables us to modify the interaction strength in order to tune the off-rates in response to experimental requirements (e.g. lower salt conditions used with proteins). The nature of the r-labels (fluorogenicity) and our imaging conditions allows us to use very high concentrations and therefore we can further enhance the on-rates, if required.

4.6 Conclusion: REFRESHing News for exhausted fluorophores

In most SMF studies, photobleaching severely limits the available photon budget from a reporter fluorophore. Each measurements needs to carefully balance temporal resolution, overall observation span, and photons collected per frame, with the latter feature determining the spatial or FRET resolution of the measurement.

By circumventing this limitation, REFRESH allows monitoring processes at high temporal resolution over long observation spans, opening many new opportunities for single-molecule studies. Most prominently, this allows access to long-lived or rare states in slow reactions, which would be mis-characterised in a bleaching-limited system. In our work, a prominent example of such slow conformational dynamics is the RNA polymerase (RNAP) clamp, a mobile element which has been shown to be critically important for RNAP function.[115] Previous work showed that the clamp populates at least three conformational states and can switch between states within the 1-s timescale. A large majority of the molecules, however, exhibits no dynamics over the photobleaching-limited observation span of the assay ($\approx$ 10 s).[116] These enzymes could all switch to a specific conformational state upon addition of substrate DNA, suggesting that the static RNAP molecules are not inactive but must indeed undergo conformational switching at timescales longer than $\approx$ 10 s. Conformational switching at long timescales was indeed observed in an experiment with reduced frame rates,[117] however, even in these studies, the number of events exhibiting slow conformations switching were limited due to photobleaching, and the reduced frame rates resulted in missed events at the fast timescales. REFRESH-FRET would allow monitoring of slow and fast conformational changes over long periods of time without sacrificing temporal resolution.

Long-lived states and slow transitions have been suggested for many proteins, nucleic acids and their complexes, and they might be critical to understand mechanisms and defining rate-limiting steps, the new capabilities proposed here will shed light on their functional role and relevance.

5

In vivo imaging of ribosomes in *E. coli* using fluorogenic ssDNA probes

Contents

5.1 Motivation

In previous chapters, we could demonstrate the versatility of fluorogenic ssDNA probes to improve or expand the scope of *in vitro* fluorescence experiments and imaging. Many crucial biological processes, however, can only be studied in their correct cellular environment and thus require *in vivo* experiments with live cells. ssDNA is, in principle, a good candidate to be used to deliver probes *in vivo* — DNA is biocompatible, the probes are relatively small compared to larger protein-based tagging systems (e.g. antibodies, Halo- or Flag-tags), and are, through choosing sequence and length, highly adaptable to different contexts. On their own, ssDNAs may be unstable in the cellular environment (and even trigger cellular responses like the SOS response),[118] but the two terminal modifications and their short length should aid in stability.

RNA seems to be a natural choice for targeting with our probes, since they can directly hybridise sequence-specifically by forming an RNA-DNA hybrid.

Single-molecule studies of RNA dynamics *in vivo* can shed light on several fundamental biological processes. RNA carries the information for and forms the catalytic unit of protein synthesis, directly linking transcription and translation. It is further subject to many processes of the cell physiology: adaptation to environmental changes, the cell's metabolic state, antibiotic stress, and much more.[119] To date, studying mRNA *in vivo* often relies on genetically modified strains, which insert aptamer binding sites at a gene of interest.[120–123] Most commonly, these are the MS2 or PP7 aptamer loops, originally derived from bacteriophages. These aptamer loops in the RNA are bound by fluorescent RNA-binding proteins, labelled either by fusion to fluorescent proteins or through tagging systems like Halo.[119,124] Especially for MS2, the loops have been engineered to provide a flexible toolbox for mRNA visualisation, adopting

to RNA turnover rates, preventing early degradation of tagged RNAs, and expanding the target organisms (to yeast and *E. coli*).[125–128]

Techniques targeting of endogenous RNA avoid the consequences of aptamer-based approaches on gene expression and the need for gene editing. On a single-molecule level, CRISPR-based RNA labelling has been performed, utilising the RNA-affinity of (a catalytically dysfunctional) dCas13.[129,130] A second class of endogenous RNA labelling protocols uses molecular beacons, which directly hybridise to a 15-20nt target sequence.[124] Similar to our probes, they carry terminal fluorophores and quenchers, which are brought into close contact by a 4-6nt long, hybridised stem region. We believe our probes improve on these molecular beacon structures in two ways: The stem structure is a kinetic barrier in the hybridisation, slowing down the binding rate. It further leaves ssDNA ends exposed after hybridisation, which could undermine the de-quenching by allowing flexibility in the fluorophore-quencher placement.

When choosing an intracellular RNA target for a proof-of-principle study, we settled on the *E. coli* ribosomal 16S RNA for several biological and technical reasons:

Ribosomes are the cellular machinery translating mRNA into proteins. In *E. coli*, they consist of the larger 50S and the smaller 30S subunit. Each of the subunit consists of several protein- and RNA-components, bridging together RNA binding- and -decoding functions with the catalytic functions of protein synthesis from individual amino acids. In bacteria, translation often occurs co-transcriptionally, so the dynamics of transcription and translation are tightly linked together.[131] Different studies using both fluorescence and cryo-electron microscopy have shown that ribosomes are excluded from the nucleoid and are dispersed throughout the cytoplasm (the individual subunits, however, can enter the nucleoid).[132,133] The distribution of ribosomes responds to the metabolic state and can change in response to antibiotic stress.[133,134] Other

members of the Kapanidis Lab have recently used ribosome distributions to detect antibiotic resistance.[135] Ribosomes are thus attractive targets for single-molecule tracking, allowing insight into fundamental biological processes and being a valuable diagnostic target.

There are further technical reasons for our choice: Firstly, ribosomes are very abundant (10s of thousand copies per cell),[132] which helps in eliminating or at least minimising off-site binding of our probes. Secondly, ribosomes consists in large parts of rRNA, some of which is available for hybridisation by ssDNA probes — a fact which has been exploited in several studies using and developing fluorescence *in situ* hybridisation (FISH)-probes for species identification in bacteria and has been used in the Kapanidis Lab for fixed-cell imaging.[135–140] For a first *in vivo* attempt at labelling using the fluorogenic probes, we can thus circumvent any genetic engineering since our docking sites are already endogenously present. Thirdly, the ribosome and its intracellular distribution has been extensively studied, which establishes a good backdrop of knowledge to help in troubleshooting a new labelling method as we propose here.[132,133,135,141,142]

In this chapter, we evaluate the performance of fluorogenic ssDNA probes targeting the 16S rRNA. We will compare them to non-fluorogenic probes in fixed cells, before assessing probe uptake protocols, probe stability and signal specificity *in vivo*. Finally, we perform a tracking analysis of single ribosome molecules.

To keep our findings widely applicable, we have designed many of the control experiments presented in the following sections to equally apply to many different probes and *in vivo* targets. Nevertheless, for each target, the specific context within the cell (copy numbers, accessibility, diffusion coefficient, size, ...) ultimately needs to be considered before translating any of the findings to a new target.

5.2 Experimental design

A full description of all experimental procedures can be found in the A.

To label ribosomes *in vivo*, we designed a fluorogenic probe which will hybridise directly to available rRNA. For our purpose, we picked a probe sequence complementary to the 16s rRNA, in the literature known as EUB338 (see Figure 5.1).[138] Its target sequence is conserved across all eubacteria, making this probe a versatile label for ribosomes across species.

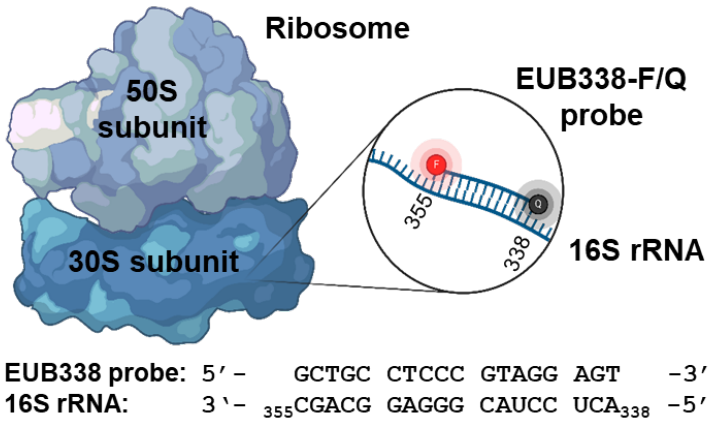

Figure 5.1: Labelling approach for ribosomes. The fluorogenic EUB338-F/Q probe hybridises to a complementary sequence of the 16S rRNA in the 30S subunit of the ribosomes.

In the Kapanidis lab, this specific sequence has been used in fixed-cell experiments for ribosome labelling for phenotyping ribosomal responses to antibiotic treatment.[135,143] The probe is 18nt long, with a 4nt internal complementarity, and is extensively characterised in chapter 2.3.3. We chose ATTO643 as fluorophore and used BHQ1 as quencher. Most remarkably, the probe exhibited a FF >60, making it highly fluorogenic (see Figure 2.5). This will provide not only a good SNR during the imaging, but will also ensure that any signal we observe is actually originating from a labelled ribosome, and not diffusing free probes.

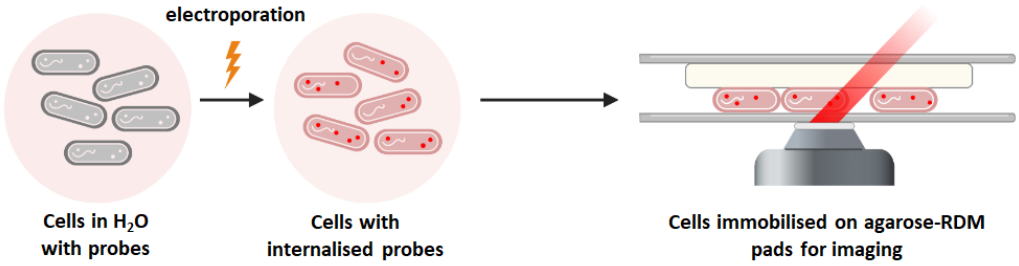

Figure 5.2: Experimental process of *in vivo* ribosome labelling with fluorogenic probes. Probes are internalised through electroporation. After washing with PBS, cells are sandwiched on an agarose pad and imaged on the microscope.

In control experiments, we will compare the ribosome-specific EUB338 probe (F/Q labelled) with a non-fluorogenic, 15nt probe only carrying a fluorophore (nF or standard probes), and a 18nt probe designed to not interact stably with RNA ('non-targeting' or nF).

For probe delivery into cells, we tested several methods, but ultimately found electroporation to be the most promising one. After electroporation and washing, the cells are immobilised by being sandwiched between an agarose pad (1 % agarose in rich defined medium (RDM)) and then imaged on the microscope (see Figure 5.2).

5.3 *In vivo* single-molecule imaging with fluorogenic ssDNAs

5.3.1 Probe performance in fixed *E.coli* cells

The probe sequence has been extensively tested for ribosome labelling in fixed cells by co-workers in the lab.[135,140,143] They, however, did not require a fluorogenic label since any unbound probes could be washed off as part of the protocol. To ensure that fluorogenic probes would in principle be able to hybridise to the ribosome target, the same fixed-cell staining was performed with the fluorogenic probes and with the established fluorophore-only probes ("standard probes"). We assessed several parameters, both before and after washing steps, in an attempt to capture the capabilities of fluorogenic probes as best as possible. Cells for this comparison were treated with ciprofloxacin, an antibiotic which inhibits topoisomerases and prevents relaxation of supercoiled DNA. This leads to a very compact nucleoid region in the centre of the cell, in which ribosomes are rarely observed.[135,143] Based on if and how well we can capture this contrast allows us to assess the performance of our probes (because the ribosomes are so vital for cellular function, it is difficult to engineer "ribosome-free" regions or cells in other ways).

After antibiotic treatment for 30 min, cells were fixed and permeabilised before EUB338 probes were added. A sample of cells was imaged before washing, all other cells were washed according to the standard protocol before being imaged. The random montages of segmented cells in Figure 5.3A show an example of the phenotype we observe from ribosome staining after ciprofloxacin treatment: A distinct dark, i.e. ribosome-poor region is clearly visible in the cell centre in which the very compact chromatin sterically excludes the ribosomes. Curiously, we can already see this in the unwashed sample stained with the standard, dye-only EUB338 probe, and it is also clearly visible when using the fluorogenic probes.

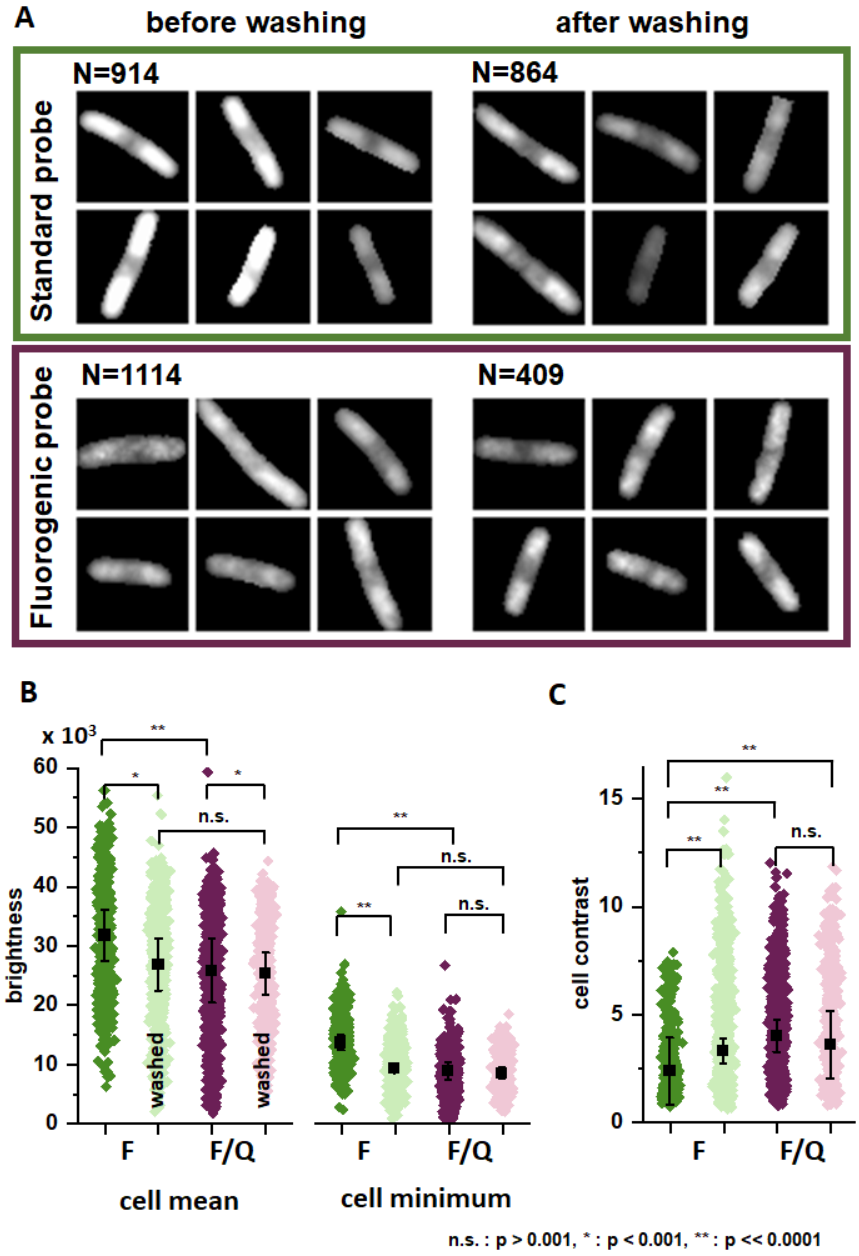

Figure 5.3: Ribosome staining with fluorogenic and standard EUB338 probe. A: Randomly selected examples of segmented cells with stained ribosomes before and after the washing steps indicated in the protocol. Both a dye-only standard probe (F, green) and a fluorogenic probe (F/Q, purple) were used. B: Mean and Minimum cell intensity in above samples. C: Cell contrast in above samples. Black markers are mean and SD from three independent experiments, each data point in colour represents an individual cell, N as given in A. p-values calculated with Kruskal-Wallis-ANOVA with post-hoc Dunn's test for individual pairings.

We evaluated the mean cell brightness (averaged across the whole cell, Figure 5.3B) as an indicator of overall loading and accessibility. In the standard sample, the mean cell brightness is reduced after washing, showing that some unbound probes were removed from the cells. The cell mean brightness in both fluorogenic samples is comparable to the standard sample after washing. We observed no decrease with the fluorogenic probes (despite the statistical significance, the effect is minimal), indicating that potentially unbound probes (which got removed in the washing steps) did not contribute much to the overall brightness — as expected when they are quenched. Between the standard and fluorogenic washed samples, there is no difference in mean brightness, suggesting both probes have good permeability into the fixed cells.

The minimum intensity (in each cell, Figure 5.3B) is a measure of the signal we see in areas where we expect the lowest ribosome density (the closest to evaluating non-specific signals). Since these regions may not be completely ribosome-free, we do not expect a complete drop in intensity to background levels, but we can overall see a substantially lower brightness of those ribosome-sparse areas for the washed or fluorogenic samples as compared to the unwashed sample stained with the standard probe. This again suggests that in the standard sample, we could remove non-specific signal from unbound probes through washing, whereas in the fluorogenic case those unbound probes did not contribute to any observed brightness. This conclusion is further supported by the higher contrast observed in the standard washed or both fluorogenic samples when compared to the standard unwashed sample (Figure 5.3C).

None of the observed differences in these fixed-cell experiments are as pronounced as we have seen in the previous applications and as the FF of the probe would suggest. This could at least partially originate from the lack of a true negative

control, i.e. a ribosome-free area or cell which we cannot easily create experimentally. Therefore, the closest to 'background' levels are the measurements of the cell minimum intensity, which might still contain a significant amount of targets, albeit less than other regions within the cells. Additionally, effects on the ensemble level might be further equalised by the fact that with so many target molecules (10s of thousands per cell[132]), the amount of free probes is relatively low either way and thus effects are less pronounced. On the ensemble level, we can, conservatively, conclude that the fluorogenic labels are capable of permeabilising the fixed cell, they bind to ribosomes and allow extracting all information about distribution of ribosomes at least as good as the standard probes after washing. The additional quencher does, consequently, not impact the probe in any negative way — and any advantage will be more prominent and crucial in the live-cell, single-molecule experiments. These findings are not necessarily specific to the ribosome-labelling EUB338 probes, but could potentially translate to other short, fluorogenic ssDNAs used to bind other cellular targets.

5.3.2 Probe uptake into live *E.coli* cells

The labelling of targets inside living cells with fluorogenic ssDNAs critically relies on a controllable and reliable delivery method. The Kapanidis Lab has extensive experience with delivery of fluorescently labelled molecules such as ssDNAs.[144–147] For single-molecule tracking with hybridising ssDNAs, the intracellular concentration (and probe numbers relative to target numbers) is critical, it dictates hybridisation kinetics, off-target binding, and the proportion of labelled targets. For the subsequent analysis and deciphering of the data, monitoring and understanding the intracellular concentrations is essential. Commonly, we deliver molecules *via* electroporation, followed by a brief recovery period. We also tested a second protocol using a chemical permeabilisation buffer commonly used in plasmid transfection. Through analysing the brightness of individual cells after

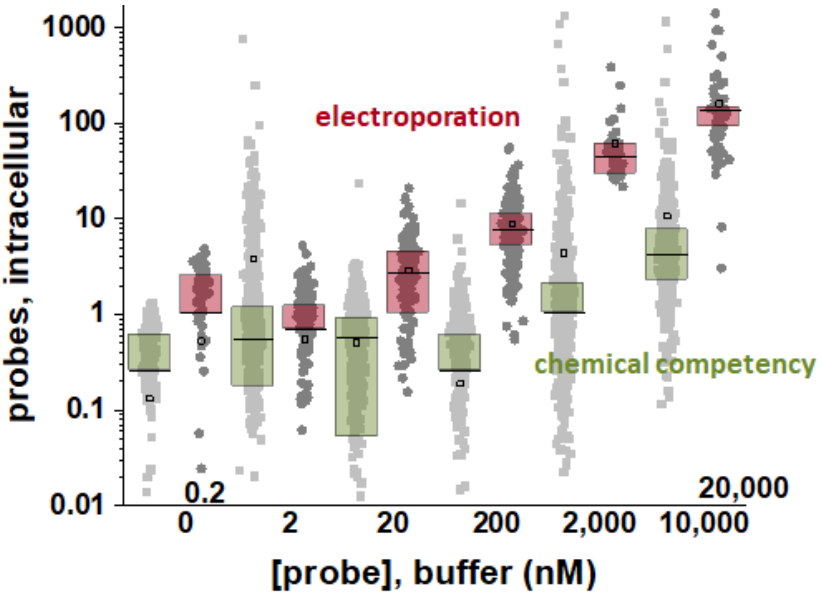

Figure 5.4: Probe uptake into live *E. coli* cells through electroporation (circles, red) and chemical competence (squares, green). Individual mean cell brightness and their population mean (black square) and median (black line with 25/75 percentiles as box).

probe uptake, we can quantify the internal probe concentration, understand the limits in probe uptake, and the heterogeneity within a sample. For these experiments, we used the EUB338 probe labelled only with ATTO643, because we are only interested in the uptake of probes, not their hybridisation state (which would influence the brightness of fluorogenic probes).

The number of probes taken up into the cell was calculated from total single cell brightnesses, divided by the observed singular intensity of individual probes (Figure 5.4). Due to imaging in epifluorescence mode, substantial background fluorescence (from free probes in the buffer) had to be subtracted. For the analysis, we consider all cells with less than 1–2 probes/ cell as empty, these are on the scale we would also expect artefacts of averaging the singular brightness across the whole FOV.

The chemical transfection method (faintly coloured/green data in Figure 5.4) yielded consistently lower probe uptake than electroporation, and required a

much higher probe concentration in the buffer for any uptake to happen. Further, there is a significant proportion of cells which remains without any probes being taken up, resulting in a larger spread of the distribution of internalised probes. In single-molecule experiments, such heterogeneity can skew results significantly, and further complicate the interpretation of any observations.

In contrast to that, electroporation with any of the tested probe concentrations yielded a single population of cellular brightnesses, which was narrower than with the chemical method. Consequently, the number of probes taken up into the cell is more defined and overall higher through electroporation (boldly coloured data in Figure 5.4, the right population for each concentration).

Despite being higher in the electroporation samples, the internal concentration of probes in all cases remains far below the buffer concentration, and outliers reach a maximum of 4-5 fold the population mean. This suggests that no equilibrium is reached between buffer and cytosol and that consequently cellular membranes remain intact during the procedures. To conclusively assess cell viability after the procedures, however, cells would need to be monitored for extensive periods of time in conditions suitable for growth. On an agarose pad with nutrient-rich media, viable cells would be expected to divide over the course of 1-2 hrs. Counting the percentage of dividing vs non-dividing cells could thus be used to assess cell viability and correlate it with the probe uptake. From experience, cell viability after electroporation is high, for our conditions around 70% of cells were dividing after electroporation in previous studies.[144,148]

We can further fit the uptake data to different uptake models and find the best fit to be a saturation-model, which suggests a maximum intra-cellular concentration of approx. 250nM can be reached with the electroporation protocol (assuming an average cell volume of 1fL, which results in 1 probe/cell $\approx$ 2nM).

Concentrations might be further increased by varying the voltage during the electroporation, or by optimising "chemical" delivery methods, if required. Higher concentrations may be required for *in vivo* REFRESH experiments, where 100s of nM are required to maintain hybridisation kinetics (even in a much higher-salt environment). In the specific case of ribosome labelling, we operate at 50nM to ensure we only label a small fraction of ribosomes, otherwise the labelling will be too dense for single-molecule tracking.

5.3.3 Fluorogenicity and signal specificity *in vivo*

For specific single-molecule tracking *in vivo*, we rely on signals only and specifically coming from probes hybridised to their target. This implies firstly that unbound probes have to remain quenched inside the cellular environment, and secondly that probes only hybridise to their specific target sequence and do not interact with other nucleic acids, proteins, or any other cellular component. Such interaction with e.g. complementary single-stranded nucleic acids (mainly RNA), single-strand binding protein (SSB) involved in DNA-repair and defence against pathogen DNA, or other, non-specific interaction partners could lead to a false-positive signal. We anticipate that also fluorophore and quencher may influence the behaviour — either through sterically hindering access to the probe ssDNA, or by interacting themselves in a non-specific manner.

Control experiments on this matter are difficult to implement as many of the potential intra-cellular interactions are with potentially vital cellular components (such as SSB), or are difficult to predict.

In an attempt to quantify the signal specificity, we compared several probes, all labelled with ATTO643 and BHQ1. We delivered them into cells and evaluated the cellular brightness in comparison to a probe not carrying BHQ1 ('non-fluorogenic' or nF). This serves as the positive control, showing what

signal level to expect if all probes were to de-quench completely. Another probe has been specifically designed to not bind any mRNA or rRNA sequence ('non-targeting' or nT). It is 18nt long, and has an internal 4nt complementary region, akin to the EUB338 probe. The maximum complementarity to any transcribed RNA is 11nt, which should be significantly more unstable than a fully bound EUB338 ribosome probe.

Figure 5.5A shows representative FOVs. Even within the different samples, cell brightnesses vary, indicating some heterogeneity in probe uptake. We have seen a similar spread when comparing different probe uptake protocols (see Figure 5.4). In our tracking experiments, we are interested in a certain spot density, which ultimately even the bright cells will achieve after a certain amount of bleaching. Heterogeneity is thus not impeding, as long as it has no further implications on e.g. cell viability. In contexts where the label concentration is more critical (like an *in vivo* version of REFRESH), uptake protocols might need to be further optimised or only cells of a certain brightness i.e. label concentration would have to be selected for analysis.

Further, brightness differences between the different samples are quite apparent: The EUB338-F/Q probe yielded brightly stained cells, with individual spots being resolvable in some. In contrast, with the nT-F/Q probe, cells appear very dim, and the nF-F probes stained cells even brighter. Quantified by the mean cell intensity (Figure 5.5B and zoom-in in C), cells show a wide distribution of brightness values, but median values recapitulate the images:

The F-only probe shows the highest signal, which serves as reference for the scenario in which all probes are fully fluorescent. The nT-probe has a much lower signal of approximately 10 % of the fully de-quenched intensity (in the fully quenched state *in vitro*, we observed approximately 3 %), suggesting that

a significant proportion of probes remains quenched and does not engage in off-target interactions with e.g. SSB or mRNA.

The remaining signal (which is higher than what we expected based on the 3% *in vitro*) suggests that either we are not fully able to interrupt all off-target interactions, or that the fully quenched state is not as dark *in vivo* as we have observed in high-salt conditions *in vitro*. In comparison, the EUB338 ribosome probes exhibit approx. 40-50 % of the nF-F probe signal, suggesting a significant target-bound population.

When localising individual spots within the FOVs, we can extract their brightness values and now examine individual molecules. For these measurements, we lowered the exposure time to 20ms in order to measure even fast-diffusing, but target bound molecules. We can see spots appearing within the cells with all probes, where probes are diffusing slow enough to be resolved as spots — presumably because there are some probes interacting with a molecule with much slower diffusion. These spots reveal the same brightness for all three probes (Figure 5.5D), supporting the idea that when bound, de-quenching is complete and those signal levels are comparable.

The number of spots varies greatly across the three probes (Figure 5.5D, data is normalised to show abundance per cell per frame): The EUB338 probe, having a high number of targets in the cell, has the most spots being found, followed by the nF-F probe. The nF-F probe sequence has not been specifically selected, so we can expect a certain level of hybridisation to cellular targets, which accounts for the spots we identify in the images. Lastly, the nT-F/Q probe showed the lowest number of spots, confirming the findings from the ensemble analysis of cell brightness values that the nT-F/Q probe remains largely unbound and quenched.

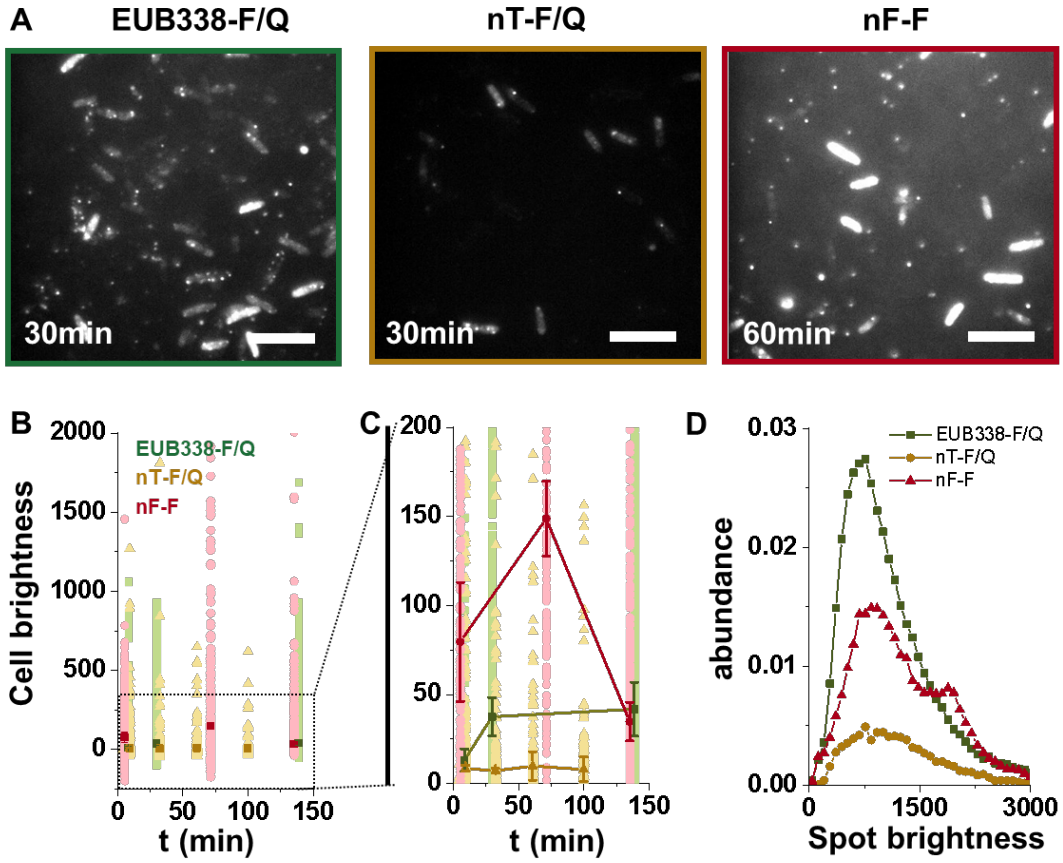

Figure 5.5: Signal specificity and fluorogenicity *in vivo*.A: Representative FOVs of cells electroporated with the three probes. B: Brightness of cells electroporated with different probes over time. Dots represent single cells, darker markers show the median value and 25-50% percentiles. C: Zoom-in on panel A. D: Brightness histogram of individual spots localised in one FOV at 20ms exposure, normalised to reflect spot abundance per cell per frame. EUB338: ribosome-targeting probe, nT: non-targeting, nF: non-fluorogenic.

In summary, through comparing the cell brightnesses, spot brightnesses and spot abundance of three different probes, we could demonstrate that our fluorogenicity is translatable into living cells and provides a SNR benefit, which on the ensemble level is about a factor of 10. This value is most likely underestimating the actual FF of individual probes, because any off-target observations would increase the background level. These occur at a basic level, even for a probe that is optimised to not exhibit many sequence-specific interactions.

The much lower amount of interactions detected with the nT-F/Q probe suggests, however, that the vast majority of signal observed for the EUB338-F/Q probe is specific and originating from sequence-specific interactions. A further filtering of the true signal might be possible based on diffusion properties, which are discussed in section 5.3.5

5.3.4 Probe stability *in vivo*

A major concern for any work including ssDNA inside live cells is the cellular machinery which evolved to detect and process ssDNA, mitigating pathogen attacks, preventing any interference with cellular processes, or ensuring efficient processing of endogenous ssDNA.

Degradation of probes by nucleases inside the cells is our greatest concern in this context for two reasons: Firstly, probes which are cut into smaller pieces will no longer be quenched since the fluorophore-carrying fragment will quickly diffuse out of the FRET-reach of the quencher. Consequently, the observed signals can no longer safely be attributed to hybridised labels or, if blurred through faster motion, contribute to a higher background level.

Secondly, the hybridisation specificity and duration is greatly altered if not completely abolished and the target can no longer be observed or tracked. We hoped that through the short length of our probes, in combination with the fluorophore and quencher modifications and any attractive interaction that stabilises a compact ssDNA conformation, the steric hindrance is protecting our probes to a certain degree from nuclease digest and allows for meaningful observations over typical experimental timescales.

To observe whether a significant digest or degradation of probes was happening within our typical experimental timescales, we electroporated cells with 50nM of one of three different probes: the ribosome-targeting EUB338-F/Q probe (18nt

long), the nT-F/Q probe designed to not form any significant hybridisation products, and the non-fluorogenic nF-F probe (15nt, nF). Immediately after electroporation, we washed cells once in PBS before placing them onto the agarose pads for imaging. This allowed us to monitor probe dynamics and any cellular response to the probes immediately after probe delivery into the cells.

We expect the three different probes to exhibit a variety of intracellular hybridisation states or distributions: The 18-nt EUB338 probes has many targets (the ribosomes) and we thus expect it to be target-bound to a large proportion. Further, the 18nt-hybridisation is near stable on the timescales of these experiments, so no significant turn-over of probes is expected. The stable hybridisation into a DNA-RNA hybrid could protect probes from degradation.

In contrast to that, the nT probe has no specific target inside the cells (any off-target sequence complementarity with RNA is a maximum of 11nt long), so we expect it to stay mostly freely diffusing and therefore quenched. The nF-probe was employed to have a comparison for the signal levels to expect in case of complete hybridisation or separation of fluorophore and quencher through e.g. digest. It has no specific target, but we have found several complementary sequences on transcribed RNA, so there could be a proportion of probes hybridised. Overall, the three probes should give a good indication of any degradation/processing happening within the timescales relevant to our experiments.

Figure 5.6 shows several representative FOVs of the three different probes imaged for up to 150 mins (Note: The image contrast and brightness settings are conserved within each row, not between the different probes. For a comparison between the probes, see Figure 5.5). The cells in each FOV exhibit a certain level of diffusive brightness, originating from probes diffusing faster than can be resolved in the respective image (200 ms exposure time here). Several cells also

have distinctly visible bright foci, here diffusion is slower, presumably because the probe is bound (some examples highlighted by arrows, more details in section 5.3.5).

The nF-probe shows the highest brightness levels (with a background corrected median cell brightness of 100–150 units, which peaks after 60 min and declines afterwards, maybe because of degradation processes.

The nT-probe exhibits a low median brightness at all time points, about 10 % of the nF probe. The nT brightness level remains constant over the course of 100 min, we therefore do not think there is a significant digest of probes happening, which would result in the release of bright probe fragments. Since this probe is remaining largely in its ssDNA state, we thought it to be the most susceptible to degradation, but its signal remains constant and at a very low level.

The EUB-F/Q probe shows a signal increase in the first 30 min of the experiment, before stabilising for the following 2 hrs at approx. 40 units. The initial increase in signal could reflect the time span of target binding, or a potential increase in target quantity after cells stabilise on the agar pads.

In summary, we observe no indication for degradation of probes on this ensemble level, and can therefore conclude that ssDNA labels are suitable for labelling cellular targets and observing them over typical experimental timescales. Based on this ensemble analysis, we cannot yet explain the dynamics observed for the nF-F probe.

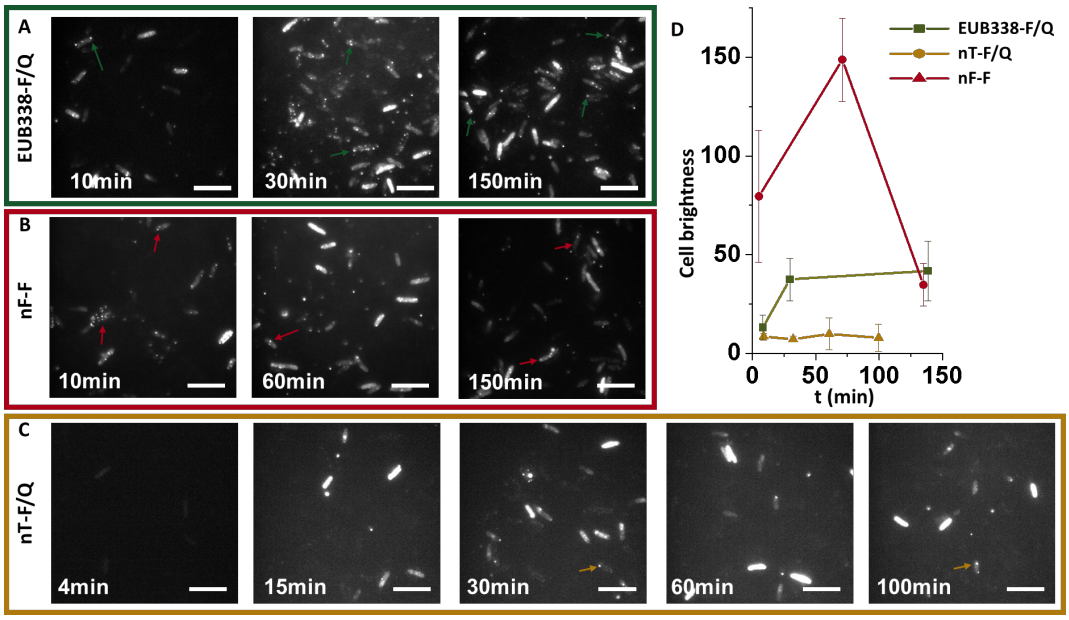

Figure 5.6: *In vivo* stability of fluorogenic probes. A-C: Cells with internalised ssDNA probes at several time points after being placed on nutrient-rich agarose pad. D: Cell brightness with median and 25-75% quartiles. This plot has been cropped to highlight time-dependent developments of median values. The full range data can be seen in Figure 5.5B. EUB338: ribosome-targeting probe, nT: non-targeting, nF: non-fluorogenic.

5.3.5 Single Ribosome tracking *in vivo*

Through a series of control experiments, we could establish that fluorogenic ssDNAs of the EUB338 sequence are suitable to label ribosomes *in vivo*. We now imaged cells electroporated with our probes at much higher speed (20 ms exposure), in order to capture the diffusive behaviour of ribosomes at different stages.[133] We localised all appearing spots with the picasso algorithm within a custom python software. Through brightfield images, we were able to segment cells and discard localisations not resulting from probes inside cells. The remaining localisations were linked to tracks. Several cells showed multiple tracks, often spanning the whole cell area (see Figure 5.7A). Tracks last on average 23 frames, with some molecules being trackable for 100s of frames.

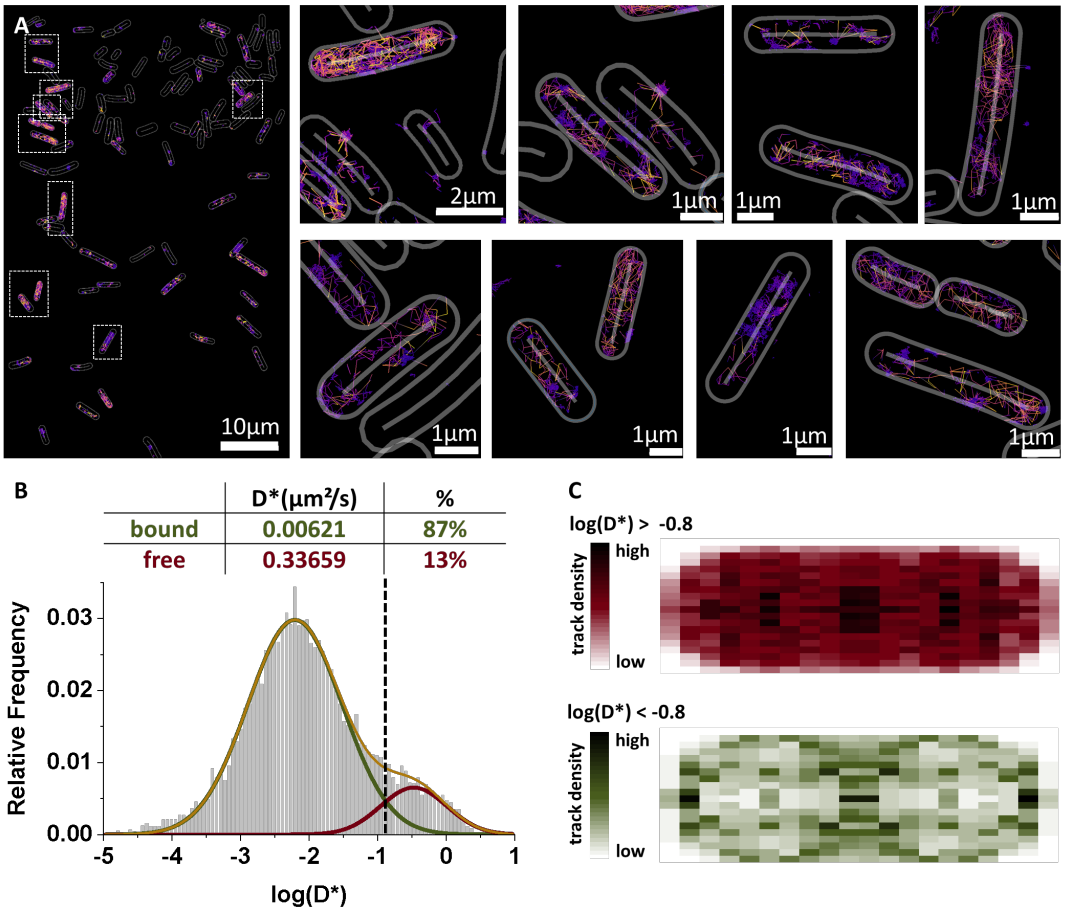

Figure 5.7: Single-molecule tracking of ribosomes *in vivo*. A: Exemplary FOV of ribosome tracks with several cells zoomed-in. Tracked Ribosomes are found across the cell, but slow (blue) tracks are more prominent in the cell periphery and on the membrane. Fast diffusing species (orange/yellow/white) can occupy the whole cell. B: Diffusion histogram of the labelled ribosomes with two fitted populations. C: Heatmaps of the spatial profile of the two populations fitted into B. Mean diffusion coefficient and percentage of each population. Data from 2155 tracks in 117 cells.

For diffusion analysis, tracks were split up into 5-frame track segments, for which diffusion histograms were extracted. We can identify two distinct subpopulations with different apparent diffusion coefficients (D*) (see Figure 5.7B). The faster subpopulation with a D* = 0.34 $\mu m^2 s^{-1}$ accounts for about 13 % of all data points (red population). This is consistent with previous measurements of the diffusion of the free small ribosomal subunit (Sanamrad *et al.* report approx. 12 % free small ribosomal subunit with D* of approx. 0.2-0.4 $\mu m^2 s^{-1}$, Bakshi

et al. find a D* of $0.35\mu m^2 s^{-1}$).[132,133] The heatmap in Figure 5.7C of this subpopulation (in red) further shows that these fast molecules are uniformly found across the whole cell (as are individual orange/yellow tracks in Figure 5.7A), in line with previous findings of the small ribosomal subunit being capable of diffusing throughout the cell, including the nucleoid.[133]

The other subpopulation shows significantly slower diffusive behaviours, with a D* about two orders of magnitude smaller (D*= $6.2 \cdot 10^{-3}$ $\mu m^2 s^{-1}$). This subpopulation has previously been termed 'bound'[133] and is found predominantly in the cell periphery, not in the nucleoid region(s) of the imaged cells (see heatmaps in Figure 5.7C, and blue-purple tracks in Figure 5.7A).

Apart from these population-level observations, we could observe changes in the diffusive state of individual ribosomes. Individual Step-size-trajectories show how the step size changes dramatically — presumably when a free subunit enters the 'bound' state — and occasionally becomes 'free' again (see Figure 5.8).

Taken together, these results - diffusion properties, spatial distributions, and observable state transitions, are consistent with our probes binding ribosomes, which we can then observe throughout their function cycle. Whilst we cannot at this point rule out an impact of our probes onto the ribosome functionality, we have several pointers suggesting labelled ribosomes remain functional: The populations of bound vs. free populations, their diffusion properties and spatial distribution remains unaltered compared to reported literature. Moreover, labelled ribosomes are capable of forming the full 70S ribosome from the 30S subunit (as evident by transitions from the free to the bound state in the trajectories), suggesting that mRNA binding (by the 30S subunit) and subsequent assembly of the 70S ribosome are unaffected (or at least not abolished) by our probe hybridising to the 16S rRNA.

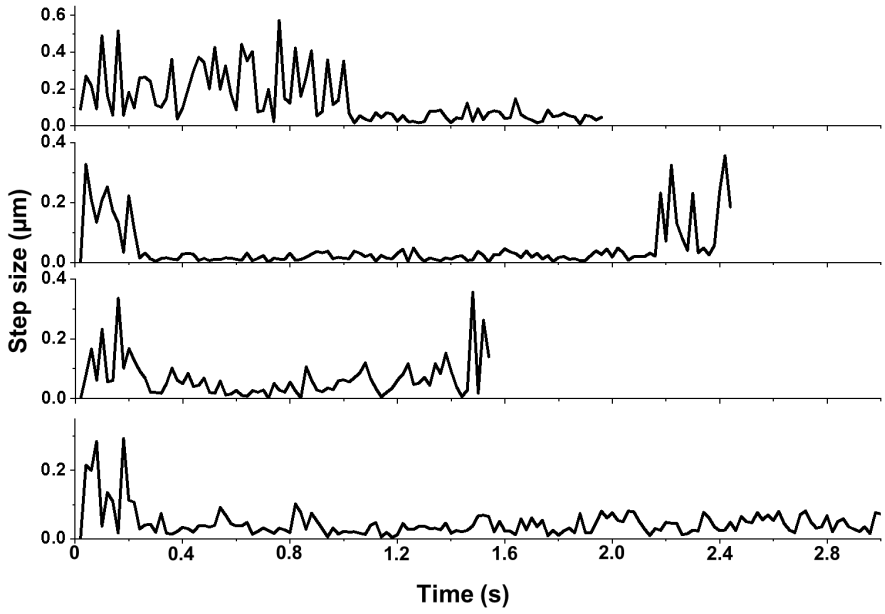

Figure 5.8: Example step-size traces of single ribosomes. Ribosomes can change diffusive states, as evident by changes in step-size.

5.4 Conclusion

In this chapter, we have translated our labelling strategy to *in vivo* single-molecule tracking. We chose ribosomes as an intracellular target, with a 18nt fluorogenic probe directly hybridising to the 16S RNA of the small ribosomal subunit.

Fixed-cell imaging confirmed that our fluorogenic probes can provide an SNR-benefit in a scenario where removal of excess, unbound probes is not possible, serving as first evidence of our fluorogenic strategy being translatable to cellular targets. Whilst we focused primarily on *in vivo* experiments in this chapter, this result provides an interesting avenue for imaging of other targets in fixed cells in settings where the advantage in speed of sample preparation can be crucial, such as in diagnostic testing.

We could further establish a delivery method for 100s of nM of our probes, opening doors for potential REFRESH-applications *in vivo* or the targeting

of low-abundance targets which require high probe concentrations for fast and efficient labelling.

Through careful examination of the signal from non-targeting, fluorogenic probes, we showed that the fluorogenic properties of our probes prevailed *in vivo*, facilitating efficient background suppression (by at least 90 %) and, consequently, a high SNR. These non-targeting probes further showed very little off-target binding, suggesting that in our experimental setting, the ssDNA is not involved in sequence-independent interactions. Further, our fluorogenic probes remained intact and quenched over the experimental time-spans of up to 150 min.

Having established that the signal from our probes is bright, specific, and the background suppression by fluorogenicity is functional *in vivo*, we moved on to performing single-molecule tracking of ribosomes. The diffusion analysis revealed two distinct subpopulations, whose apparent diffusion coefficients and spatial distribution are in accordance with those reported for 'free' and 'bound' ribosomal subunits.[132,133] We have so far not optimised our imaging conditions to obtain longer tracks by reducing the excitation power, and adjusting the label concentration to prevent wrongly linked tracks. For the analysis, we thus chose short track segments of just 5 frames to minimise any bias this might induce. With longer tracks, however, we should be able to observe more of these transitions between different diffusive states, allowing access to the kinetics of processes the ribosome is involved in. The exposure time of 20 ms allowed us to clearly image the free subunit diffusion, but potential substates in the slow population are lost in the localisation error. With longer exposure times, we could shift the sensitivity towards slower diffusive processes. We are currently working on stroboscopy illumination and overall longer exposure times at lower laser powers, and are confident the probes are photostable enough to image tracks long enough to capture significant timescales of ribosome functional - the average

translation duration of an average protein should be ≈ 15-20 s (assuming 300 amino acids in length and a translation speed of 15-20 amino acid per second[131]).

Further, our probes allow us to study the ribosomes in the context of different perturbations, such as antibiotic treatments. Reproducing the ribosome phenotypes which have been observed in response to treatment with antibiotics such as ciprofloxacin, gentamicin, and chloramphenicol, this would further support the specificity of the EUB338 probes.[135] Especially given the absence of a true negative control (i.e. observing our probes *in vivo* but in the absence of ribosomes), such perturbation experiments are particularly important. Moreover, in live cells, antibiotic susceptibility testing as co-workers have performed it[135] would not require fixation protocols, instead we can monitor the phenotype as it develops after electroporation in live cells. The tracking might reveal a more detailed phenotype with different parameters characterising each antibiotic response (rather than just the spatial distribution in fixed cells), some of which might develop fast and could allow for rapid read-out of susceptibility. Such tests are particularly interesting with respect to patient samples potentially containing different bacterial species. The EUB338 probe hybridises to a rRNA sequence conserved in all eubacteria,[138] and can thus be used for ribosome labelling in a species-independent way.

In summary, we demonstrated functional single-molecule tracking *in vivo* using fluorogenic ssDNA probes. Our signal is specific without any genetic engineering and can accurately report on the diffusive behaviour of our target, the small ribosomal subunit.

6

Single-molecule fluorescence imaging with fluorogenic ssDNA probes

Contents

6.1 Flexibility of fluorogenicity

This thesis has developed a method to facilitate fluorescent labelling by utilising short ssDNAs to hybridise their complementary sequence. We designed fluorogenicity into the probes, by terminally linking a fluorophore and a quencher to the ssDNA. In the single-stranded, un-hybridised state, the probes remain quenched through contact-mediated and/or FRET quenching processes. The change in end-to-end distance of the probe upon hybridisation leads to a change in distance between fluorophore and quencher, resulting in de-quenching and a substantial increase in fluorescence. As a consequence, the background fluorescence from unbound probes is greatly reduced, facilitating a better SNR, which allows operating at much higher concentrations (we demonstrated experiments at 2 μM, but can still identify single molecules at 10 μM), much above the "high concentration barrier" (50-100 nM for TIRF experiments). Further, fluorogenic probes provide very specific signal only when bound to their target, which allows them to be implemented in *in vivo* imaging.

Expanding on previous work on molecular beacons, fluorogenic DNA-PAINT imagers and PCR probes, we performed a detailed characterisation of the parameters in our design that allow us to adopt the fluorogenic strategy to different experimental requirements. The characterisation work we performed in this thesis thus laid the ground for a universal design strategy of fluorogenic ssDNA-based probes, which found a multitude of applications, some of which we have discussed in this thesis.

Previous work often focused on finding the most efficient quenching, which then in turn sacrificed the potential de-quenching, or significantly restricted the remaining design parameters (such as label sequence, length, or choice of dye(s)) and consequently only had limited or very specific applicability in many cases.[28,36,52]

In contrast, we identified the R_0 between fluorophore and quencher in combination with the probe length as the major tuning screws to facilitate fluorogenicity. They shape the careful balance between good quenching in the ssDNA and sufficient de-quenching in the dsDNA state: The label length determines the end-to-end distance between fluorophore and quencher in both hybridisation states, long distances as seen in longer labels lead to less quenching in the unbound, but more de-quenching in the hybridised state. The R_0 on the other hand, determines the level of quenching at any given distance, and also affects the change in distance which leads to the most change in fluorescence emission. We can utilise these properties to create a good level of fluorogenicity (FF>10) in a wide range of experimental scenarios:

Whether specific hybridisation kinetics are required, or the experimental setting dictates the label sequence and length: The choice of R_0 can be adjusted to facilitate fluorogenicity in any scenario with labels between 5-25nt, which covers most hybridisation timescales required in experiments, as well as facilitating specific hybridisation within a large sequence space. Some experiments might require a certain level of fluorescence emission, on which they cannot compromise - a low R_0 or longer label can facilitate this, albeit by increasing the background.

Other scenarios require the best possible SNR but are more flexible about other parameters, and so the combination with the absolute best FF will be most suitable - potentially combined with transient secondary interactions within the label: This greatly increased fluorogenicity (FF>60) by stabilising a ssDNA confirmation with very short F-Q distances, suggesting that probes even longer than 25nt could be made fluorogenic with our strategy.

The design of a fluorogenic probe should thus be seen as a process of optimising and adjusting several parameters, rather than searching for the one universal best way - this would ultimately sacrifice performance in certain applications.

We have outlined the trends these parameters follow and have given concrete experimental values for a set of combinations which can inform other researchers and allow for easy implementation into new and existing protocols.

6.2 Plug & play level solutions to implement fluorogenicity

Our universal design approach has allowed us to implement fluorogenicity into a great variety of experimental settings. From classical single-molecule FRET experiments (albeit with a twist), to super-resolution imaging and *in vivo* single-particle tracking, we could use fluorogenic ssDNA probes to harness a variety of their specific advantages, which will be outlined in the following.

6.2.1 Fast DNA-PAINT imaging of viral gene segments

The DNA-PAINT application was chosen to highlight the ease of implementation of the fluorogenic labels into an existing protocol. We chose a different imager sequence of our desired length and sequence, adjusted the F-Q combination and could start imaging, without the requirement for extensive experimental troubleshooting or optimisation of imager properties. Implementing fluorogenicity into our DNA-PAINT experiment allowed us to significantly speed up the imaging process, recovering the physical features (segment radius, <20 nm) of the imaged viral gene segments after just 3 min. This was facilitated by using a very short 6 nt imager strand at high concentrations, which, in combination with a short exposure time of only 20 ms, lead to a faster accumulation of binding events and therefore sampling of the target structure. Fluorogenicity here facilitated improvements on existing DNA-PAINT protocols, by harnessing the much reduced background emission of fluorogenic imager strands.

6.2.2 Bleaching-resistant SMF and FRET

The development of fluorogenic labels has also allowed us to follow completely new experimental paths, addressing the long-standing problem of photo-bleaching in SMF. High operational concentrations allow us to achieve turnover-kinetics of transiently binding labels fast enough to create a near-continuous labelling of target structures whilst constantly exchanging the fluorophore. This approach, which we termed REFRESH, makes the overall experimental timescale independent of the bleaching of individual fluorophores.

We labelled HJs with exchanging donors and acceptors, facilitating smFRET measurements of individual molecules for 1 hour and accumulating 18,000 data points from an individual molecule. The fluorogenic labelling did not affect the FRET values or dynamics of the conformational changes of the HJs, promising good performance for studying other target structures of biological interest.

Our experiments were made possible by very high operational concentrations in the 100 nM-1 μM range, and so we relied on the fluorogenicity to improve the SNR and facilitate these measurements.

6.2.3 *In vivo* ribosome tracking

For *in vivo* tracking applications, signal specificity is crucial. Otherwise, the true signal and diffusive behaviour is "diluted" too much by wrongly labelled molecules to make meaningful conclusions. ssDNA labels can provide specificity by their sequence, and the fluorogenicity allows us to observe only those molecules bound to a target structure whilst keeping background fluorescence low.

We could demonstrate that the fluorogenicity remains functional *in vivo*, our probes are stable over typical timespans, and we can target a specific cellular component, here the ribosome. When tracking individual ribosomes, we could

recapitulate their spatial distributions and diffusion properties, as previous studies with different tagging approaches had found them.[133,149]

In *in vivo* applications, where unbound probes cannot be simply removed from the cellular environment, fluorogenicity allowed us to optically remove them from the background and only visualise hybridised probes. The ssDNA-nature of them further allowed us to directly hybridise our target structure without the need for any genetic engineering, simply using the wildtype strain.

6.3 Future Applications

The aim of the great deal of characterisation work performed as part of this thesis was to create a solid basis for easy and broad application of fluorogenic ssDNAs in different fluorescence imaging contexts. Based on what we have demonstrated to date, there are several new avenues we can envision for future experiments and expansions, a few of which we will briefly discuss in the following.

6.3.1 Long-term study of proteins using REFRESH

In principle, the REFRESH approach can be extended to more complex conformational ensembles to monitor functionally relevant changes in conformational states, such as in large protein complexes.

One interesting target are the mechanistics of RNA polymerase (RNAP), the central molecular machine responsible for gene transcription in cells. Starting from studies on single diffusing transcription complexes[150–153], the Kapanidis group has established robust smFRET strategies on immobilised complexes, which can also monitor transcription in real-time with high-temporal resolution (down to 5 ms) for >5 minutes.[154–156] An attractive molecular target for bleaching-free FRET is a vital RNAP structural module, the RNAP clamp, which forms one wall of the active-site cleft of RNAP. Results from previous studies indicate that

the clamp populates at least three conformational states and can switch between these on the second timescale. A large majority of the molecules, however, exhibits no dynamics over the observation time of the assay (∼10 s).[157,158] These enzymes could switch to a specific conformational state upon addition of substrate DNA, suggesting that the static RNAP molecules are not inactive but must indeed undergo conformational switching at timescales which remain inaccessible under the current experimental conditions limited by photobleaching to only ∼10 s. Bleaching-free FRET should allow monitoring of these conformational changes over long periods of time without sacrificing temporal resolution.

These slow conformational changes may have substantial functional relevance, as has been proposed for other DNA-processing machines (e.g., the RecBCD DNA helicase[158]). The new capabilities proposed here will shed light on this fundamental biophysical question. Furthermore, since the bacterial RNAP has significant structural and functional similarities with eukaryotic and archaeal RNAPs, understanding bacterial transcription will illuminate the mechanisms of many RNAPs, some of which have large biomedical and biotechnological importance.

6.3.2 Imaging mRNA expression on the single-molecule level

Based on our success of achieving fast hybridisation kinetics to complementary DNA-sequences, and the ability to also target RNA demonstrated by tracking the ribosome *in vivo*, we envision using our fluorogenic probes to facilitate monitoring of many rounds of transcription emanating from a single DNA molecule on the surface.

Specifically, mRNA expression will be monitored by sequence-specific, diffusing probes which (reversibly or stably) bind their complementary sequence on the

mRNA. Using one probe (one colour) complementary to a sequence of interest, the hybridisation will report on transcription activity, transcription speed, as well as processes such as transcription re-initiation.

By competitively binding in regions of RNA secondary structures, the assay could be further developed to look at co-transcriptional RNA folding. Since certain mRNA regions will become inaccessible to the probe once folding is complete, the ability for an mRNA to hybridise transiently with a probe and generate fluorescence signal will be lost. This signal loss will identify the timing of the RNA folding event.

Implementing a second imager complementary to an RNA sequence at other points along the gene allows monitoring the time elapsing between the emergence of specific mRNA sequences, and will provide access to the transcription speed and transcriptional pausing as well as further insight into the formation of RNA secondary structures.

The obtained kinetic data can provide insight into the stochasticity of *in vitro* transcription and pave the way for similar experiments combining it with (REFRESH-)FRET: While a doubly labelled RNAP molecule performs the transcription, conformational states will be identified and the inter-transition kinetics could be characterised by the bleaching-free FRET assay, and the kinetic data gained on mRNA production will allow connecting the conformational profile of a protein to functional states and functional heterogeneity - creating a unique link between functional and structural states of a large protein complex.

6.3.3 *In vivo* (m)RNA tracking

Based on the achievements in tracking rRNA *in vivo*, we could envision a monitoring system for production of specific mRNAs in the presence of all regulatory pathways and cellular influences. Such work will allow studying

the spatial distribution as well as the kinetics of mRNA production with high spatial and temporal resolution.

RNA levels within bacterial cells fluctuate substantially, and are controlled by stochastic events, such as DNA conformational changes, transcription factor binding, and rate-limiting steps during transcription. These large variations in RNA levels are due to transcription bursts, i.e., transcripts being produced during periods of intense activity, followed by inactivity.[159–161] The origin of this burst behaviour is far from clear. It is also unclear how gene location affects transcription, especially considering previous work in the Kapanidis lab showing that transcription of moderately-to-highly expressed genes occurs in the nucleoid periphery.[162] As part of the efforts to study and understand transcription on a mechanistic level, the production of specific mRNAs *in vivo* is of particular interest.

A

Appendix

Contents

A.1 Glossary

ALEX	alternating laser excitation
FF	fluorogenic factor
FISH	fluorescence *in situ* hybridisation
FOV	field of view
FRET	fluorescence resonance energy transfer
HJ	holliday junction
HMM	hidden markov model
ISC	inter-system crossing
LB	lysogeny broth
MLE	maximum-likelihood-estimator
NP	nucleo-protein
OD	optical density
PAINT	points accumulation for imaging in nanoscale topography
PALM	photo-activated localisation microscopy
PCA	protocatechuic acid
PCD	protocatechuate-3,4-dioxy-genase
PCR	polymerase chain reaction
PET	photo-induced electron transfer
PSF	point-spread function
Q	quencher
RDM	rich defined medium
REFRESH	renewable emission via fluorogenic and repeated ssDNA hybridisation
RNAP	RNA polymerase
SMF	single-molecule fluorescence
SMLM	single-molecule localisation microscopy
SNR	signal-to-noise ratio
SRM	super-resolution microscopy
SSB	single-strand binding protein
STED	stimulated emission depletion
STORM	stochastic optical reconstruction microscopy

TIRF	total internal reflection
WLC	worm-like chain model
dsDNA	double-stranded DNA
gloxy	cocktail of glucose/glucose-oxidase/catalase
smFRET	single-molecule fluorescence resonance energy transfer
ssDNA	single-stranded DNA
vRNP	viral ribonucleoprotein complex

A.2 Material & Methods chapter 2: Tuning fluorogenicity

Some illustrations in this chapter were created in biorender.

A.2.1 Characterisation experiments

Probe design

All labelled probe sequences can be found in Table A.1. They were modified to carry a 5'-ATTO647N and a 3'-quencher. Probes of different lengths were designed to conserve the 3nts surrounding the fluorophore and quencher attachment site (5'-ATTO647N-TTT-X_n-TTT-quencher), with only the central section altered to facilitate different lengths. The 18nt probe which contained a 4nt self-complementary region differs from this design. All probes were ordered from biomers.net (Ulm, Germany). Complementary, biotinylated docking strands were ordered from Merck (Darmstadt, Germany).

Sample preparation

Target strands were immobilised via a 3'-biotin binding NeutrAvidin on coverslips coated by polyethylene-glycol (PEG). In wells of silicone gaskets, 20 µL of the target strands (100-500 pM) were incubated for 10-30 s, followed by washing three times with 200 µL PBS. Subsequently, 30 µL of DNA imaging buffer (200 mM $MgCl_2$, 10 mM NaCl, 50 mM HEPES pH 7.4, 6 mM BSA, 3 mM Trolox, 1 % Glucose, 40 µg/mL catalase and 0.1 mg/mL glucose oxidase) containing the stated probe concentrations were added.

Imaging

Single-molecule fluorescence movies were collected using the Nanoimager-S single-molecule fluorescence microscope (Oxford Nanoimaging). The microscope

was used as a widefield single-molecule fluorescence microscope with objective-based total internal reflection fluorescence (TIRF) illumination mode, with the excitation angle set at 54.0°. We performed the imaging using continuous-wave excitation (640 nm, with the laser powers of 9 % (1.4 mW). In all experiments, we used 100-ms exposures.

Image processing

To obtain brightness information for localised spots ('signal'), all '.tif' files obtained from imaging at 10 nM were processed in the Picasso 'localize' tool[51]. Photon counts of these localisations were frequency-counted and distributions were fitted to obtain mean photon counts for each probe. In some samples, we observed two brightness populations. We excluded the population resulting from probes without functional quenchers (either bleached quenchers or faulty synthesis), which exhibits the same brightness as probes with only the F labelling (.

Data presentation & comparison

The obtained photon counts were normalised by dividing them by the average photon counts observed for probes without quenchers ('normalised signal').

$$normalised\ S = S_N = \frac{S_{FQ}}{S_F} \tag{A.1}$$

From the all videos, background intensities were extracted using a custom script, averaged over the central area of the field of view and across all frames of the movies. The background intensities were plotted against the probe concentration and fitted with a linear regression in Origin (Origin Labs). These molar background emissions were normalised by dividing them by the molar background emission of probes only labelled with a F, but no quencher ('normalised background').

$$normalised\ B = B_{N,mol} = \frac{B_{FQ,mol}}{B_{F,mol}} \tag{A.2}$$

Both values can be then used to calculate the FF, which is the fold change in emission intensity upon hybridisation:

$$\mathrm{FF} = \frac{S_N}{B_{N,mol}} \tag{A.3}$$

The normalisation applied here extracts changes induced by the addition of the quencher to a probe and is not sensitive to e.g. changes in quantum yield of the dye when forming dsDNA. To keep our assessment as general as possible, we would like to be makes the assessment agnostic to these effects. Any FF>1 in this work reports on a fluorogenicity greater than what could be observed in the fluorophore-only constructs.

For comparison with theoretical estimates, we calculated predicted quenching efficiencies for all the probes in section 2.3.2, approximating their end-to end distances with the WLC model:[60]

The Worm-Like Chain (WLC) model formula for the mean-squared end-to-end distance is:

$$\langle R^2 \rangle = 2L_p L \left(1 - \frac{L_p}{L}\left(1 - e^{-L/L_p}\right)\right) \tag{A.4}$$

Where L_p is the persistence length (1 nm for ssDNA, 50 nm for dsDNA),$L = N \cdot l_{\mathrm{nt}}$ is the contour length, N is the number of nucleotides,l_{nt} is the length per nucleotide (0.6 nm for ssDNA, 0.34 nm for dsDNA).

The root-mean-square (RMS) end-to-end distance is:

$$R_{\mathrm{RMS}} = \sqrt{\langle R^2 \rangle} \tag{A.5}$$

To correct the distance for helical structure in dsDNA, we use:

$$R_{\mathrm{eff}} = \sqrt{R_{\mathrm{WLC}}^2 + \left(2r \sin\left(\frac{\theta}{2}\right)\right)^2} \tag{A.6}$$

Where r is the radial distance from the helix axis (we have assumed 1 nm) and $\theta = N \times 34.3°$ is the angular offset based on the number of nucleotides. From these predicted distance, we have calculated expected signal levels under the assumption that all quenching is mediated purely by FRET.

Calculation of Förster radii of FQ-pairs

We measured absorption spectra of all quenchers on the Nanodrop, and used the fluorophore emission spectra and fluorophore fluorescence lifetimes provided by the manufacturer.[85,86] The Förster radii were then calculated using the FRET-Calc tool.[163]

A.2.2 Single-molecule hybridisation assay

Sample preparation

Oligos were obtained from biomers.net and Merck, dissolved to a final concentration of 100 µM, and stored at -20 °C (for sequences, see Table S1). All components of the gapped target were mixed in annealing buffer (200 mM Tris–HCl pH 8.0, 500 mM NaCl, 1 mM EDTA) at 2 µM, and then annealed in a thermocycler (program: heating to 90 °C, then cooling to 25 °C at 2 °C/min, storing at 4 °C). The labelled 8 nt probe was ordered from biomers.net (Ulm, Germany), carrying a 3' Atto647N and a 5'-BHQ1. Preparation of surfaces and immobilisation was performed as described for characterisation experiments. Imaging was performed in buffer containing 20 mM Hepes, 200 mM NaCl, 80 mM $MgCl_2$, 5 % dextran sulphate, and 5 % formamide.

Imaging

Samples were imaged at 2 µM under the same conditions as described for the characterisation experiments. Imaging was performed at 1.4 mW of 640 nm and 0.8 mW of 532 nm excitation, with an exposure time of 200 ms.

Data analysis

Molecules were localised in the green channel, traces were extracted and fitted with an HMM using a custom Python software. Binding kinetics were fitted using the probability density functions, correcting for finite exposure times of the camera and length of states in MEMLET.[109] All graphs were plotted in Origin (Origin Labs).

A.3 Materials & Methods chapter 3: DNA-PAINT

Some illustrations in this chapter were created in biorender.

Virus strain

A/Puerto Rico/8/34 (H1N1) influenza virus (PR8) purified from embryonated chicken eggs was purchased from Charles River Laboratories, aliquoted, flash-frozen in liquid N_2 and stored at -80 °C before use.

Probe design

Primary probes against the NA and the PB1 segment were designed as outlined in Hepp *et al.*[15], the PB1 probes were adopted to contain multiplexed docking sites against the 6nt-imager (5'-CCACCACCACCA-3'). All sequences of primary probes were taken from Hepp *et al.*[15] The P3 imager sequence was used as described previously[51] and was fluorescently labelled with Cy3B on the 5' end. The 6nt imager has the following sequence: 5'-TGGTGG-3' and was labelled with ATTO643 or ATTO647N on the 5' and with BMNQ1 or BHQ1, respectively, on the 3' end. Imager strands were purchased from Metabion international AG (P3-Cy3B, Planegg, Germany) or biomers.net (6nt imagers, Ulm, Germany).

Virus sample preparation and imaging

All virus samples were prepared as outlined in Hepp *et al.*[15], in brief this comprised the following steps: Cover slips were cleaned (sonic bath and plasma cleaner) to remove any contaminations immediately before use. Viral particles were thawed on ice and fixed using 4% formaldehyde. After dilution in 0.9 % NaCl solution, viral particles were added into CultureWell gaskets (Ø 6 mm, Grace Biolabs, US) mounted on the cleaned coverslips, and the liquid evaporated at 40 °C. After removal of the gaskets, sticky slides VI0.4 (ibidi, Germany) were used to create flow channels over the viral particles. Viral particles were then permeabilised with 0.5 % Triton-X-100 before primary probes were added to a final concentration of 4 µM and incubated overnight at 37 °C. Unbound probes were removed using a clearing buffer before DNA-PAINT imaging was performed. Samples were imaged on the Nanoimager at laser powers of 3.6 mW (532 nm) and 150 mW (640 nm) at exposure times of 200 and 20 ms, respectively.

Image processing

The image processing steps are following those outlined in Hepp *et al.*[15], but were adjusted to adopt the different noise behaviour in these experiments: Localizations were detected with Picasso "Localize"[51] with the following sections: box length: 7, gradient: P3 is 3000 and 6 nt is 5000, baseline: 400, sensitivity: 2.75, quantum efficiency: 0.82, pixel size: 117 nm. The gain (=sensitivity * quantum efficiency) and offset(=baseline) are estimated using the sCMOS analysis provided by GDSC imageJ plugin[164].

Localisations were then undrifted using the AIM algorithm[165] implemented in picasso render using the following parameters: Segmentation: 100 frames, Intersection distance: 20 nm, max. drift in segment: 60 nm. DBSCAN[166] was performed to find clusters with the following parameters: eps: 0.5 pixel,

min_samples: 0.01 * frame number. Clusters were then filtered by core sample ratio (number of core samples / total samples > 0.8) and with component number = 2 in the 6 nt data.

To extract physical features from the found clusters, each localisation in a cluster is rendered as a Gaussian with a sigma of 7.8 nm, then a low pass filter (order-one Butterworth filter with a cut-off frequency of 0.02) and Gaussian filter (sigma 5.85 nm) are applied to the image. Next, it is transferred to a binary image using the ISODATA method (excluding any clusters larger than 5000 nm^2), then the Hilditch skeleton[167] is found to represent the segment ("spine"). If branches exist in the skeleton, the longest one is chosen. The median value of the distance between each pixel on the skeleton and the boundary of the binary image is considered to be the radius of the segment. Reconstructed super-resolution images were exported from Picasso "Render".[51]

A.4 Materials & Methods chapter 4: REFRESH

Some illustrations in this chapter were created in biorender.

Determining the Fluorogenic Factor

To characterise the level of quenching, we performed ensemble measurements, assessing the absorption spectra and the fluorescence of the quenched r-labels in absence and presence of up to 100-fold excess of complementary DNA. The fluorescence spectra were measured at a scanning spectro-fluorometer (PTI) using 1-s integration time per 1-nm-wavelength intervals using 100 µL r-labels in buffer (50 mM HEPES, pH 7.4; 200 mM $MgCl_2$, 10 mM NaCl, 0.1 % BSA, the same buffer as used for single molecule measurements) to a final concentration of 100 nM. Complementary DNA was added stepwise to achieve different concentrations until saturation of the signal was observed (0.1-10 µM). Samples

were excited at 520 nm (containing Cy3B), 620 nm (containing ATTO647N) or 640 nm (containing ATTO655).

Holliday junction annealing and immobilisation on surfaces

Oligos were obtained from Metabion and Merck, dissolved to a final concentration of 100 µM, and stored at -20°C (for sequences, see Table S1). HJ components (strands: HJ-H, HJ-B, HJ-X or HJ-XI, HJ-R or HJ-RI) were mixed in annealing buffer (200 mM Tris–HCl pH 8.0, 500 mM NaCl, 1 mM EDTA) at 2-4 µM, and then annealed in a thermocycler (program: heating to 90 °C, then cooling to 25 °C at 2 °C/min, storing at 4 °C). HJs were immobilised via a biotinylated H-strand binding NeutrAvidin on coverslips coated by polyethylene-glycol (PEG). In wells of silicone gaskets, 20 µL of the HJs (100 -500 pM) were incubated for 10-30 s, followed by washing three times with 200 µL PBS. Subsequently, 30 µL of DNA imaging buffer (200 mM $MgCl_2$, 10 mM NaCl, 50 mM HEPES pH 7.4, 6 mM BSA, 3 mM Trolox, 1 % Glucose, 40 µg/mL catalase and 0.1 mg/mL glucose oxidase) containing the stated r-label concentrations were added. For hour-long acquisition of FRET dynamics, the buffer was renewed at a rate of 6 µL/min, allowing for a complete volume exchange every 5 min.

Imaging

Single-molecule fluorescence movies were collected using the Nanoimager-S single-molecule fluorescence microscope (Oxford Nanoimaging). The microscope was used as a widefield single-molecule fluorescence microscope with objective-based TIRF illumination mode, with the excitation angle set at 53.6°. We performed the imaging using continuous-wave excitation (532 nm for Cy3B and 640 nm for ATTO647N) or alternating laser excitation (ALEX) mode, with the laser powers of 12-13 % (2.9-3.6 mW) at 532 nm; and 6 % (1.4 mW) at 640 nm. In

all experiments, we used 100 ms exposures and ALEX movies were recorded at 100 ms/frame/excitation, leading to traces with 200 ms temporal resolution.

Fluorescence trace extraction

Movies were corrected for lateral drift as follows: localisations were found using Picasso[51] 'localize' and were then loaded in 'render' and un-drifted by redundant cross-correlation (RCC). The created drift file was used in a custom MATLAB (MathWorks) script to undrift individual frames, which were then combined using FIJI.[168] For all data except the red 1-hr trace, fluorescence intensity vs. time traces were extracted and background-corrected using TwoTone.[169] The program extracts the fluorescence intensity in the green and red channel upon green excitation (DD and DA, respectively), and in the red channel upon red excitation (AA). Traces were manually inspected and any traces, in which multiple molecules were detected, were discarded. For one-colour experiments, the DD signal was used for localisation, and the AA signal was plotted as intensity vs time traces. In FRET experiments, all three signals were used to calculate the apparent FRET efficiency E and donor-acceptor stoichiometry S were calculated as follows:[170]

$$E = \frac{DA}{DD + DA} \tag{A.7}$$

$$S = \frac{DA + DA}{DD * DA * AA} \tag{A.8}$$

Two-dimensional E-S plots were used to select data points which contain both donor and acceptor dyes, for which E histograms were plotted. Further analysis and HMM fitting were performed using ebFRET.[171] We fitted two distinct FRET states and extracted dwell time histograms for each state. By fitting these with a single exponential, the transition rates were determined. Stated rates with errors are means and standard deviations, respectively, of three independent

experiments. The figures show exemplary data from one of multiple experiment per condition. All traces and histograms were plotted using Origin (OriginLab).

Determining binding-kinetics of the r-labels

For extraction of dwell times from our fluorescence time traces, we performed HMM fitting on the intensity vs time traces obtained for both r-labels. Fitting worked well on the green traces, but for the red label, the multiple emission states of ATTO647N combined with the two intensity levels resulting from two bound fluorophores lead to difficulties for hidden markov model (HMM) fitting. We thus resulted to using localisation-based information extracted using Picasso[51] for fitting dwell times for the red r-label. Localisations were extracted using the 'localize' tool and then undrifted using redundant cross correlation (RCC). All remaining localisations were filtered for in sx/sy for the main population and linked, allowing one dark frame between localisations. From this data, the length of binding events (= on times) and the dark time between events (= off time) can be extracted. To give readers straightforward numbers for the hybridisation kinetics in the main text, we have calculated mean values of toff and ton, and the inverse values as k_{on} and k_{off}, respectively. From previous studies, we know, however, that the hybridisation kinetics are indeed better described by a bi-exponential decay with two independent decay constants. To further characterise the binding behaviour, we thus fitted a bi-exponential distribution to the dwell times (extracted as described in the main experimental section) of both r-labels using a maximum-likelihood-estimator in Matlab (MEMLET[109]). The fitted function takes into account the minimum measurable dwell time (one frame) and the discrete nature of the observable values. Confidence intervals for fitted decay times were determined via bootstrapping.

A.5 Materials & Methods chapter 5: *In vivo* single-molecule tracking

Some illustrations in this chapter were created in biorender.

Fixed cell experiments

Bacterial cultures were prepared in a shaking incubator at 37℃ in 5 mL lysogeny broth (LB) until reaching an optical density (OD) of 0.2. Then, 0.5 mg/L ciprofloxacin were added, and the samples were incubated at 37°C for 30 min. Samples were then fixed in 2 % paraformaldehyde for 20 min. After fixation, cells were pelleted and washed once with 1xPBS, and re-suspended in 5 mL 1xPBS before being split into 1 mL aliquots and permeabilised in 500 µL absolute ethanol before being stored at -20 °C.

Before imaging, the cells were centrifuged to remove the ethanol supernatant, washed with 500 μL1xPBS, and resuspended in hybridization buffer (20 % v/v formamide, 0.9 M NaCl, 20 mM Tris pH 7.5, 0.01 % SDS w/v). 25 nM of EUB338-ATTO643 or ATTO643-BHQ1 were added to the solution and the sample was incubated for 20 min (for sequences, please see table A.1). Following incubation, the samples were washed and resuspended in 150 µL PBS.

Samples were imaged on agarose pads prepared with 1.5 % (w/v) high purity agarose (Bio-Rad, US) in distilled water. Images were collected on the Nanoimager (ONI, UK) with a 100X oil-immersion objective in multi-acquisition mode. Image processing and segmentation. Each field of view was segmented using BacSeg, a user-friendly bacterial analysis platform that allows microscopy images to be segmented using machine learning models. Within the software, the resulting segmentations can be easily curated and then exported in multiple formats to facilitate downstream analysis. Descriptive statistics of the segmented bacteria can also be computed and exported. The BacSeg plugin can be

installed from the Napari Hub, the Python package manager PyPi, or GitHub (https://github.com/piedrro/naparibacseg).

Transfection of fluorogenic ssDNAs

Electro-competent cells were created as follows: *E. coli* MG1655 wildtype cells were grown in LB medium at 37 °C, 350 rpm to an OD of 0.4. Cells were pelleted and washed three times with MilliQ water, aliquoted (20 μL), and flash-frozen at -80 °C. Prior to electroporation, cells were thawed on ice and incubated with 5μLthe relevant concentration of ssDNA probes for 5–10 mins. For electroporation, cells were transferred to chilled electro-cuvettes (Bio-Rad, US) and electroporated at 1.4 kV. Cells recovered in SOC media at 37 °C, 350 rpm for 30 min. Cells were pelleted at 3300xg at 4 °Cand washed three times with chilled PBS. After the final wash, cells were suspended in 20 µL of 1X PBS and placed on ice.

Chemical competency was achieved following the manufacturers instructions of the Mix & Go! E.coli Transformation Kit (Zymo Research, US). Briefly, cells were grown to an OD of 0.5, then pelleted and washed once with the provided washing buffer. Cells were then resuspended in the provided competent buffer and frozen at -80 °C.

Imaging of live cells

For imaging, cells were placed on 1 % agarose pads containing 1X RDM. Images of cells were collected in bright field and fluorescence mode (excitation at 640 nm, 10-16 mW) on the Nanoimager (ONI, UK) at exposure times of 20 and 200 ms. Fluorescence images were acquired at beam angles of 0 and 51°.

Image analysis

For extraction of brightness data, brightfield images were segmented using BacSeg (as outlined for the fixed cell experiments), before the masks were used on the fluorescence images to extract e.g. brightness data. For tracking, the python software MolTrack was used, which tracks individual molecules within the segmented cell masks (as created with BacSeg). It can be installed from GitHub (https://github.com/piedrro/napari-moltrack). Tracks were split into 5-frame segments and D* values were extracted in a custom python script. Diffusion data was extracted and visualised using Origin (Origin Labs).

A.6 DNA sequences

Table A.1: DNA-Sequences used in this Thesis.

Name	Sequence 5' → 3'	5' linked	3' linked
Characterisation			
SP_5_A647N_BHQ1	TTTTT	A647N	BHQ1
SP_6_A647N_BHQ1	TTTTT T	A647N	BHQ1
SP_8_A647N_BHQ1	TTTGG TTT	A647N	BHQ1
SP_10_A647N_BHQ1	TTTGT GGTTT	A647N	BHQ1
SP_12_A647N_BHQ1	TTTGT TGGTT TT	A647N	BHQ1
SP_15_A647N_BHQ1	TTTGT TGGTT GGTTT	A647N	BHQ1
SP_20_A647N_BHQ1	TTTGT TGGTT GGGTT GTTTT	A647N	BHQ1
SP_25_A647N_BHQ1	TTTGT TGGTT GGGTT GTGTT GGTTT	A647N	BHQ1
SP_6_comp_bio	AAAAA A	biotin	
SP_8_comp_bio	AAACC AAA	biotin	
SP_10_comp_bio	AAACC ACAAA	biotin	
SP_12_comp_bio	AAAAC CAACA AA	biotin	
SP_15_comp_bio	AAACC AACCA ACAAA	biotin	
SP_20_comp_bio	AAAAC AACCC AACCA ACAAA	biotin	
SP_25_comp_bio	AAACC AACAC AACCC AACCA ACAAA	biotin	
SP_15_BHQ1	TTTGT TGGTT GGTTT	A647N	BHQ1
SP_15_BHQ2	TTTGT TGGTT GGTTT	A647N	BHQ2
SP_15_BBQ650	TTTGT TGGTT GGTTT	A647N	BBQ650
SP_15_A647N	TTTGT TGGTT GGTTT	A647N	
SP_18_2ndry	GCTGC CTCCC GTAGG AGT	A647N	BHQ1

Name	**Sequence 5' → 3'**	**5' linked**	**3' linked**
SP_18_comp_2ndry_bio	ACTCC TAC GG GAG GC AGC	biotin	
REFRESH			
HJ-B	CCCTA GCAAG CCGCT GCTAC GG		
HJ-H	CCGTA GCAGC GAGAG CGGTG GG	biotin	
HJ-R	CCCAC CGCTC TTCTC AACTG GG	ATTO647N	
HJ-X	CCCAG TTGAG AGCTT GATAG GG	Cy3B	
HJ-RI	aaaaa gggaa aCCCACCGCTCTTCTCAACTGGG		
HJ-XI	ttcaa cattt cttct CCCAGTTGAGAGCTTGATAGGG		
rI-2xATTO647N	tttcc ctttt t	ATTO647N	ATTO647N
rI-ATTO647N-Dabcyl	tttcc ctttt t	ATTO647N	3'Dabcyl
rI-ATTO647N-BHQ3	tttcc ctttt t	ATTO647N	BHQ3
comprI	aaaaa gggaa a		
gI-Cy3B-BHQ2	agaag taatg tggaa	Cy3B	BHQ2
compgI	ttcaa cattt cttct		
8mer-2xATTO655	tccac cgt	ATTO655	ATTO655
Comp-8mer	acggt gga		
DNA-PAINT			
P3	GTAAT GAAGA	Cy3B	
P1	CTAGA TGTAT	Cy3B	
6ntI_A643_BMNQ1	TGGTG G	Atto 643	BMNQ1
6ntI_A647N_BHQ1	TGGTG G	A647N	BHQ1
comp_R2-6mer_bio	TTTCC ACCA	biotin	
Primary Probes 6ntI_PB1	CCACC ACCAC CA-R		PB1 Sequences[15]
Primary Probes P1_PB1	TTATA CATCT A-R		PB1 Sequences[15]

Name	**Sequence 5' → 3'**	**5' linked**	**3' linked**
Primary Probes P3_NA	TCTTC ATTAC-R		NA Sequences[15]
Ribosomes			
EUB_A647N_BHQ1	GCTGC CTCCC GTAGG AGT	A647N	BHQ1
EUB_A643_BHQ1	GCTGC CTCCC GTAGG AGT	Atto 643	BHQ1
comp EUB18_bio	ACTCC TACGG GAGGC AGC	biotin	
non-targeting_F/Q	ATCAT GATCC CTAGA TCT	Atto 643	BHQ-1
F_A643	AAGAA GTAAA GGGAG	Atto 643	BHQ-1

References

1. Miller, H., Zhou, Z., Shepherd, J., Wollman, A. J. M. & Leake, M. C. Single-molecule techniques in biophysics: a review of the progress in methods and applications. *Reports on Progress in Physics* **81,** 24601 (2 2017).
2. Xie, X. S., Choi, P. J., Li, G. W., Nam, K. L. & Lia, G. *Single-molecule approach to molecular biology in living bacterial cells* May 2008.
3. Lelek, M. *et al.* Single-molecule localization microscopy. *Nature Reviews Methods Primers* **1,** 39 (1 June 2021).
4. Löschberger, A. *et al.* Super-resolution imaging visualizes the eightfold symmetry of gp210 proteins around the nuclear pore complex and resolves the central channel with nanometer resolution. *Journal of Cell Science* **125,** 570–575 (3 Feb. 2012).
5. Hess, S. T., Girirajan, T. P. K. & Mason, M. D. Ultra-high resolution imaging by fluorescence photoactivation localization microscopy. *Biophysical Journal* **91,** 4258–4272 (11 Dec. 2006).
6. Betzig, E. *et al.* Imaging intracellular fluorescent proteins at nanometer resolution. *Science* **313,** 1642–1645 (5793 Sept. 2006).
7. Rust, M. J., Bates, M. & Zhuang, X. Sub-diffraction-limit imaging by stochastic optical reconstruction microscopy (STORM). *Nature Methods* **3,** 793–795 (10 Oct. 2006).
8. Gelles, J., Schnapp, B. J. & Sheetz, M. P. Tracking kinesin-driven movements with nanometre-scale precision. *Nature* **331,** 450–453 (6155 Feb. 1988).
9. Schmidt, T., Schutz, G. J., Baumgartner, W., Gruber, H. J. & Schindler, H. Imaging of single molecule diffusion. *Proceedings of the National Academy of Sciences* **93,** 2926–2929 (7 Apr. 1996).
10. Pertsinidis, A., Zhang, Y. & Chu, S. Subnanometre single-molecule localization, registration and distance measurements. *Nature* **466,** 647–651 (7306 July 2010).
11. Jungmann, R. *et al.* Single-molecule kinetics and super-resolution microscopy by fluorescence imaging of transient binding on DNA origami. *Nano Letters* **10,** 4756–4761 (11 Nov. 2010).
12. Shroff, H., White, H. & Betzig, E. Photoactivated localization microscopy (PALM) of adhesion complexes. *Current protocols in cell biology* **41,** 4–21 (1 2008).

13. Reinhardt, S. C. M. *et al.* Ångström-resolution fluorescence microscopy. *Nature* **617,** 711–716 (7962 May 2023).

14. Sigal, Y. M., Zhou, R. & Zhuang, X. Visualizing and discovering cellular structures with super-resolution microscopy. *Science* **361,** 880–887 (6405 2018).

15. Hepp, C., Zhao, Q., Robb, N., Fodor, E. & Kapanidis, A. *Structural analysis of the influenza genome by high-throughput single-virion DNA-PAINT* to be submitted. 2024.

16. Shashkova, S. & Leake, M. C. Single-molecule fluorescence microscopy review: shedding new light on old problems. *Bioscience reports* **37,** BSR20170031 (2017).

17. Tinnefeld, P. Breaking the concentration barrier. *Nature Nanotechnology* **8,** 480–482 (7 July 2013).

18. Holzmeister, P., Acuna, G. P., Grohmann, D. & Tinnefeld, P. *Breaking the concentration limit of optical single-molecule detection* 2014.

19. White, D. S., Smith, M. A., Chanda, B. & Goldsmith, R. H. Strategies for Overcoming the Single-Molecule Concentration Barrier. *ACS Measurement Science Au* **3,** 239–257 (4 Aug. 2023).

20. Andrews, R. *et al.* Transient DNA binding to gapped DNA substrates links DNA sequence to the single-molecule kinetics of protein-DNA interactions. *bioRxiv,* 2022.02.27.482175 (Jan. 2022).

21. Peng, S., Wang, W. & Chen, C. Breaking the Concentration Barrier for Single-Molecule Fluorescence Measurements. *Chemistry – A European Journal* **24,** 1002–1009 (5 2018).

22. Van Oijen, A. M. Single-molecule approaches to characterizing kinetics of biomolecular interactions. *Current Opinion in Biotechnology* **22,** 75–80 (1 Feb. 2011).

23. Puchkova, A. *et al.* DNA Origami Nanoantennas with over 5000-fold Fluorescence Enhancement and Single-Molecule Detection at 25 µM. *Nano Letters* **15,** 8354–8359 (12 Dec. 2015).

24. Sharonov, A. & Hochstrasser, R. M. Wide-field subdiffraction imaging by accumulated binding of diffusing probes. *Proceedings of the National Academy of Sciences of the United States of America* **103,** 18911–18916 (50 Dec. 2006).

25. Vietz, C., Lalkens, B., Acuna, G. P. & Tinnefeld, P. Synergistic Combination of Unquenching and Plasmonic Fluorescence Enhancement in Fluorogenic Nucleic Acid Hybridization Probes. *Nano Letters* **17,** 6496–6500 (10 Oct. 2017).

26. Livak, K. J., Flood, S. J., Marmaro, J., Giusti, W. & Deetz, K. Oligonucleotides with fluorescent dyes at opposite ends provide a quenched probe system useful for detecting PCR product and nucleic acid hybridization. *PCR methods and applications* **4,** 357–362 (6 1995).

27. Lee, L. G., Connell, C. R. & Bloch, W. Allelic discrimination by nick-translation PCR with fluorogenic probes. *Nucleic acids research* **21,** 3761–3766 (16 Aug. 1993).

28. Tyagi, S. & Kramer, F. R. Molecular beacons: probes that fluoresce upon hybridization. *Nature biotechnology* **14,** 303–308 (3 1996).

29. Tyagi, S., Bratu, D. P. & Kramer, F. R. Multicolor molecular beacons for allele discrimination. *Nature Biotechnology* **16** (1 1998).

30. Johansson, M. K., Fidder, H., Dick, D. & Cook, R. M. Intramolecular Dimers: A New Strategy to Fluorescence Quenching in Dual-Labeled Oligonucleotide Probes. *Journal of the American Chemical Society* **124,** 6950–6956 (24 June 2002).

31. Dubertret, B., Calame, M. & Libchaber, A. J. Single-mismatch detection using gold-quenched fluorescent oligonucleotides. *Nature Biotechnology 2001 19:4* **19,** 365–370 (4 2001).

32. Nazarenko, I. Multiplex quantitative PCR using self-quenched primers labeled with a single fluorophore. *Nucleic Acids Research* **30,** 37e–37 (9 May 2002).

33. Marras, S. A. E., Kramer, F. R. & Tyagi, S. Efficiencies of fluorescence resonance energy transfer and contact-mediated quenching in oligonucleotide probes. *Nucleic acids research* **30** (21 2002).

34. Reste, L. L., Hohlbein, J., Gryte, K. & Kapanidis, A. N. Characterization of dark quencher chromophores as nonfluorescent acceptors for single-molecule FRET. *Biophysical Journal* **102,** 2658–2668 (11 2012).

35. Zhang, Z., Revyakin, A., Grimm, J. B., Lavis, L. D. & Tjian, R. Single-molecule tracking of the transcription cycle by sub-second RNA detection. *eLife* **3,** e01775 (Jan. 2014).

36. Chung, K. K. H. *et al.* Fluorogenic DNA-PAINT for faster, low-background super-resolution imaging. *Nature Methods* **19,** 554–559 (5 May 2022).

37. Schueder, F. *et al.* Unraveling cellular complexity with transient adapters in highly multiplexed super-resolution imaging. *Cell* **187,** 1769–1784 (2024).

38. Kessler, L. F. *et al.* Self-quenched Fluorophore Dimers for DNA-PAINT and STED Microscopy. *Angewandte Chemie (International ed. in English)* **62** (39 Sept. 2023).

39. Weigert, F. & Käppler, G. Polarisierte Fluoreszenz in Farbstofflösungen. *Zeitschrift für Physik* **25,** 99–117 (1924).

40. Gaviola, E. & Pringsheim, P. Über den Einfluss der Konzentration auf die Polarisation der Fluoreszenz von Farbstofflösungen. *Zeitschrift für Physik* **24,** 24–36 (1924).

41. Förster, T. Zwischenmolekulare Energiewanderung und Fluoreszenz. *Annalen der Physik* **437,** 55–75 (1948).

42. Förster, T. Delocalization excitation and excitation transfer. *Modern quantum chemistry* (1965).

43. Hellenkamp, B. *et al.* Precision and accuracy of single-molecule FRET measurements—a multi-laboratory benchmark study. *Nature methods* **15,** 669 (2018).

44. Stryer, L. & Haugland, R. P. Energy transfer: a spectroscopic ruler. *Proceedings of the National Academy of Sciences of the United States of America* **58,** 719 (1967).

45. Hestand, N. J. & Spano, F. C. Expanded Theory of H- and J-Molecular Aggregates: The Effects of Vibronic Coupling and Intermolecular Charge Transfer. *Chemical Reviews* **118,** 7069–7163 (15 Aug. 2018).

46. Kasha, M., Rawls, H. R. & El-Bayoumi, M. A. The exciton model in molecular spectroscopy. *Pure and Applied Chemistry* **11,** 371–392 (3-4 Jan. 1965).

47. Albani, J. in, 141–192 (Elsevier, 2004).

48. Lakowicz, J. R. in, 277–330 (Springer US, 2006).

49. Lakowicz, J. R. in, 331–351 (Springer US, 2006).

50. in (International Union of Pure and Applied Chemistry (IUPAC), Feb. 2014).

51. Schnitzbauer, J., Strauss, M. T., Schlichthaerle, T., Schueder, F. & Jungmann, R. Super-resolution microscopy with DNA-PAINT. *Nature Protocols* **12,** 1198 (6 2017).

52. Schueder, F. & Bewersdorf, J. Highly Multiplexed Imaging with Speed and Fluorogenic DNA-PAINT. *Microscopy and Microanalysis* **29,** 1069–1069 (Supplement$_1$ July 2023).

53. Jungmann, R. *et al.* Multiplexed 3D cellular super-resolution imaging with DNA-PAINT and Exchange-PAINT. *Nature Methods* **11,** 313–318 (3 Mar. 2014).

54. Strauss, S. & Jungmann, R. Up to 100-fold speed-up and multiplexing in optimized DNA-PAINT. *Nature Methods* **17,** 789–791 (8 2020).

55. Linko, V. *et al.* One-step large-scale deposition of salt-free DNA origami nanostructures. *Scientific Reports* **5,** 15634 (1 Oct. 2015).

56. Kielar, C. *et al.* On the Stability of DNA Origami Nanostructures in Low-Magnesium Buffers. *Angewandte Chemie International Edition* **57,** 9470–9474 (30 July 2018).

57. Kümmerlin, M., Mazumder, A. & Kapanidis, A. N. Bleaching-resistant, Near-continuous Single-molecule Fluorescence and FRET Based on Fluorogenic and Transient DNA Binding. *ChemPhysChem* **24,** e202300175 (12 June 2023).

58. Tsourkas, A., Behlke, M. A., Rose, S. D. & Bao, G. Hybridization kinetics and thermodynamics of molecular beacons. *Nucleic Acids Research* **31,** 1319–1330. eprint: `https://academic.oup.com/nar/article-pdf/31/4/1319/7038350/gkg212.pdf` (Feb. 2003).

59. Asanuma, H., Fujii, T., Kato, T. & Kashida, H. Coherent interactions of dyes assembled on DNA. *Journal of Photochemistry and Photobiology C: Photochemistry Reviews* **13,** 124–135 (2 June 2012).

60. Milstein, J. N. & Meiners, J.-C. in, 2757–2760 (Springer Berlin Heidelberg, 2013).

61. Murphy, M., Rasnik, I., Cheng, W., Lohman, T. M. & Ha, T. Probing single-stranded DNA conformational flexibility using fluorescence spectroscopy. *Biophysical journal* **86,** 2530–2537 (2004).

62. Zadeh, J. N. *et al.* NUPACK: analysis and design of nucleic acid systems. *Journal of computational chemistry* **32,** 170–173 (1 2011).

63. Yurke, B. & Mills, A. P. Using DNA to power nanostructures. *Genetic Programming and Evolvable Machines* **4,** 111–122 (2003).

64. Ouldridge, T. E., Šulc, P., Romano, F., Doye, J. P. K. & Louis, A. A. DNA hybridization kinetics: Zippering, internal displacement and sequence dependence. *Nucleic Acids Research* **41,** 8886–8895 (19 2013).

65. Craig, M. E., Crothers, D. M. & Doty, P. Relaxation kinetics of dimer formation by self complementary oligonucleotides. *Journal of molecular biology* **62,** 383–401 (1971).

66. Arranz, R. *et al.* The structure of native influenza virion ribonucleoproteins. *Science (New York, N.Y.)* **338,** 1634–1637 (6114 Dec. 2012).

67. Bancroft, C. T. & Parslow, T. G. Evidence for Segment-Nonspecific Packaging of the Influenza A Virus Genome. *Journal of Virology* **76,** 7133–7139 (14 July 2002).

68. Chou, Y.-y. *et al.* One influenza virus particle packages eight unique viral RNAs as shown by FISH analysis. *Proceedings of the National Academy of Sciences* **109,** 9101–9106 (23 June 2012).

69. Gavazzi, C. *et al.* A functional sequence-specific interaction between influenza A virus genomic RNA segments. *Proceedings of the National Academy of Sciences* **110,** 16604–16609 (41 Oct. 2013).

70. Cobbin, J. C. A. *et al.* Influenza Virus PB1 and Neuraminidase Gene Segments Can Cosegregate during Vaccine Reassortment Driven by Interactions in the PB1 Coding Region. *Journal of Virology* **88,** 8971–8980 (16 Aug. 2014).

71. Gilbertson, B. *et al.* Influenza NA and PB1 Gene Segments Interact during the Formation of Viral Progeny: Localization of the Binding Region within the PB1 Gene. *Viruses* **8,** 238 (8 Aug. 2016).

72. Aw, J. G. A., Shen, Y., Nagarajan, N. & Wan, Y. Mapping RNA-RNA Interactions Globally Using Biotinylated Psoralen. *Journal of Visualized Experiments* (123 May 2017).

73. Dadonaite, B. *et al.* The structure of the influenza A virus genome. *Nature Microbiology* **4,** 1781–1789 (11 July 2019).

74. Sage, V. L. *et al.* Mapping of Influenza Virus RNA-RNA Interactions Reveals a Flexible Network. *Cell Reports* **31,** 107823 (13 June 2020).

75. Jakob, C. *et al.* Sequential disruption of SPLASH-identified vRNA–vRNA interactions challenges their role in influenza A virus genome packaging. *Nucleic Acids Research* **51,** 6479–6494 (12 July 2023).

76. Noda, T. *et al.* Architecture of ribonucleoprotein complexes in influenza A virus particles. *Nature* **439,** 490–492 (7075 Jan. 2006).

77. Nakatsu, S. *et al.* Complete and Incomplete Genome Packaging of Influenza A and B Viruses. *mBio* **7** (5 Nov. 2016).

78. Noda, T. *et al.* Three-dimensional analysis of ribonucleoprotein complexes in influenza A virus. *Nature Communications* **3,** 639 (1 Jan. 2012).

79. Harris, A. *et al.* Influenza virus pleiomorphy characterized by cryoelectron tomography. *Proceedings of the National Academy of Sciences* **103,** 19123–19127 (50 Dec. 2006).

80. Huang, Q. J. *et al.* Quantitative structural analysis of influenza virus by cryo-electron tomography and convolutional neural networks. *Structure* **30,** 777–786.e3 (5 May 2022).

81. Schueder, F. *et al.* An order of magnitude faster DNA-PAINT imaging by optimized sequence design and buffer conditions. *Nature Methods* **16,** 1101–1104 (11 Nov. 2019).

82. Beliveau, B. J. *et al.* Single-molecule super-resolution imaging of chromosomes and in situ haplotype visualization using Oligopaint FISH probes. *Nature Communications* **6,** 7147 (1 May 2015).

83. Nir, G. *et al.* Walking along chromosomes with super-resolution imaging, contact maps, and integrative modeling. *PLOS Genetics* **14,** e1007872 (12 Dec. 2018).

84. Steen, P. R. *et al.* The DNA-PAINT palette: a comprehensive performance analysis of fluorescent dyes. *Nature Methods* (Aug. 2024).

85. GmbH, A.-T. *Atto647N product Information* Apr. 2022.

86. GmbH, A.-T. *Atto643 product Information* Sept. 2024.

87. biomers.net. *biomers.net | BMN Dyes and Quencher - biomers.net Oligonucleotides* "accessed 29/08/2024". 2023.

88. Nieuwenhuizen, R. P. *et al.* Measuring image resolution in optical nanoscopy. *Nature methods* **10,** 557–562 (2013).

89. Banterle, N., Bui, K. H., Lemke, E. A. & Beck, M. Fourier ring correlation as a resolution criterion for super-resolution microscopy. *Journal of structural biology* **183,** 363–367 (2013).

90. Hirschfeld, T. Quantum efficiency independence of the time integrated emission from a fluorescent molecule. *Appl. Opt.* **15,** 3135–3139 (12 Dec. 1976).

91. Bruchez, M., Moronne, M., Gin, P., Weiss, S. & Alivisatos, A. P. Semiconductor Nanocrystals as Fluorescent Biological Labels. *Science* **281,** 2013–2016 (5385 1998).

92. Joo, C. *et al.* Real-Time Observation of RecA Filament Dynamics with Single Monomer Resolution. *Cell* **126,** 515–527 (3 Aug. 2006).

93. Choi, J. *et al.* Dynamics of the context-specific translation arrest by chloramphenicol and linezolid. *Nature Chemical Biology* **16,** 310–317 (3 Mar. 2020).

94. Ha, T. & Tinnefeld, P. Photophysics of fluorescent probes for single-molecule biophysics and super-resolution imaging. *Annual review of physical chemistry* **63,** 595–617 (Jan. 2012).

95. Harada, Y., Sakurada, K., Aoki, T., Thomas, D. D. & Yanagida, T. Mechanochemical coupling in actomyosin energy transduction studied by in vitro movement assay. *Journal of molecular biology* **216,** 49–68 (1990).

96. Aitken, C. E., Marshall, R. A. & Puglisi, J. D. An oxygen scavenging system for improvement of dye stability in single-molecule fluorescence experiments. *Biophysical journal* **94,** 1826–1835 (2008).

97. Shi, X., Lim, J. & Ha, T. Acidification of the oxygen scavenging system in single-molecule fluorescence studies: in situ sensing with a ratiometric dual-emission probe. *Analytical chemistry* **82,** 6132–6138 (2010).

98. Swoboda, M. *et al.* Enzymatic oxygen scavenging for photostability without pH drop in single-molecule experiments. *ACS nano* **6,** 6364–6369 (2012).

99. Scheckenbach, M., Schubert, T., Forthmann, C., Glembockyte, V. & Tinnefeld, P. Self-Regeneration and Self-Healing in DNA Origami Nanostructures. *Angewandte Chemie International Edition* **60,** 4931–4938 (9 Feb. 2021).

100. Spahn, C., Grimm, J. B., Lavis, L. D., Lampe, M. & Heilemann, M. Whole-Cell, 3D, and Multicolor STED Imaging with Exchangeable Fluorophores. *Nano Letters* **19,** 500–505 (1 Jan. 2019).

101. Spahn, C. *et al.* Protein-Specific, Multicolor and 3D STED Imaging in Cells with DNA-Labeled Antibodies. *Angewandte Chemie International Edition* **58,** 18835–18838 (2019).

102. Werther, P. *et al.* Bio-orthogonal Red and Far-Red Fluorogenic Probes for Wash-Free Live-Cell and Super-resolution Microscopy. *ACS Central Science* **7,** 1561–1571 (9 Sept. 2021).

103. Stehr, F. *et al.* Tracking single particles for hours via continuous DNA-mediated fluorophore exchange. *Nature Communications* **12,** 4432 (1 Dec. 2021).

104. Vermeer, B. & Schmid, S. Can DyeCycling break the photobleaching limit in single-molecule FRET? *Nano Research* **15,** 9818–9830 (11 May 2022).

105. Ha, T. & Tinnefeld, P. Photophysics of fluorescent probes for single-molecule biophysics and super-resolution imaging. *Annual review of physical chemistry* **63** (2012).

106. Vogelsang, J. *et al.* A reducing and oxidizing system minimizes photobleaching and blinking of fluorescent dyes. *Angewandte Chemie International Edition* **47,** 5465–5469 (2008).

107. SantaLucia, J. A unified view of polymer, dumbbell, and oligonucleotide DNA nearest-neighbor thermodynamics. *Proceedings of the National Academy of Sciences* **95,** 1460–1465 (4 1998).

108. Zhang, J. X. *et al.* Predicting DNA hybridization kinetics from sequence. *Nature chemistry* **10,** 91–98 (2018).

109. Woody, M. S., Lewis, J. H., Greenberg, M. J., Goldman, Y. E. & Ostap, E. M. MEMLET: An Easy-to-Use Tool for Data Fitting and Model Comparison Using Maximum-Likelihood Estimation. *Biophysical Journal* **111,** 273–282 (2 July 2016).

110. Lambert, T. J. FPbase: a community-editable fluorescent protein database. *Nature Methods* **16,** 277–278 (4 Apr. 2019).

111. McKinney, S. A., Déclais, A. C., Lilley, D. M. J. & Ha, T. Structural dynamics of individual Holliday junctions. *Nature Structural Biology* **10,** 93–97 (2 Feb. 2003).

112. Vogelsang, J. *et al.* A reducing and oxidizing system minimizes photobleaching and blinking of fluorescent dyes. *Angewandte Chemie International Edition* **47,** 5465–5469 (29 2008).

113. Gilboa, B. *et al.* Confinement-free wide-field ratiometric tracking of single fluorescent molecules. *Biophysical journal* **117,** 2141–2153 (2019).

114. Blumhardt, P. *et al.* Photo-induced depletion of binding sites in DNA-PAINT microscopy. *Molecules* **23,** 3165 (12 2018).

115. Mazumder, A., Ebright, R. H. & Kapanidis, A. N. Transcription initiation at a consensus bacterial promoter proceeds via a 'bindunwindload-and-lock' mechanism. *eLife* **10** (2021).

116. Duchi, D., Mazumder, A., Malinen, A. M., Ebright, R. H. & Kapanidis, A. N. The RNA polymerase clamp interconverts dynamically among three states and is stabilized in a partly closed state by ppGpp. *Nucleic acids research* **46,** 7284–7295 (2018).

117. Mazumder, A., Wang, A., Uhm, H., Ebright, R. H. & Kapanidis, A. N. RNA polymerase clamp conformational dynamics: Long-lived states and modulation by crowding, cations, and nonspecific DNA binding. *Nucleic Acids Research* **49** (5 2021).

118. Lima-Noronha, M. A. *et al.* Sending out an SOS - the bacterial DNA damage response. *Genetics and Molecular Biology* **45** (3 suppl 1 2022).

119. Gerber, A., van Otterdijk, S., Bruggeman, F. J. & Tutucci, E. Understanding spatiotemporal coupling of gene expression using single molecule RNA imaging technologies. *Transcription* **14,** 105–126 (3-5 Oct. 2023).

120. Bertrand, E. *et al.* Localization of ASH1 mRNA Particles in Living Yeast. *Molecular Cell* **2,** 437–445 (4 Oct. 1998).

121. Lange, S. *et al.* Simultaneous Transport of Different Localized mRNA Species Revealed by Live-Cell Imaging. *Traffic* **9,** 1256–1267 (8 Aug. 2008).

122. Larson, D. R., Zenklusen, D., Wu, B., Chao, J. A. & Singer, R. H. Real-Time Observation of Transcription Initiation and Elongation on an Endogenous Yeast Gene. *Science* **332,** 475–478 (6028 Apr. 2011).

123. Chao, J. A., Patskovsky, Y., Almo, S. C. & Singer, R. H. Structural basis for the coevolution of a viral RNA–protein complex. *Nature Structural & Molecular Biology* **15,** 103–105 (1 Jan. 2008).

124. Tingey, M. *et al.* Technologies Enabling Single-Molecule Super-Resolution Imaging of mRNA. *Cells* **11,** 3079 (19 Sept. 2022).

125. Golding, I. & Cox, E. C. RNA dynamics in live Escherichia coli cells. *Proceedings of the National Academy of Sciences of the United States of America* **101,** 11310–11315 (31 Aug. 2004).

126. Tutucci, E. *et al.* An improved MS2 system for accurate reporting of the mRNA life cycle. *Nature Methods 2017 15:1* **15,** 81–89 (1 Nov. 2017).

127. Tutucci, E., Vera, M. & Singer, R. H. Single-mRNA detection in living S. cerevisiae using a re-engineered MS2 system. *Nature Protocols 2018 13:10* **13,** 2268–2296 (10 Sept. 2018).

128. Li, W., Maekiniemi, A., Sato, H., Osman, C. & Singer, R. H. An improved imaging system that corrects MS2-induced RNA destabilization. *Nature Methods* **19,** 1558–1562 (12 Dec. 2022).

129. Yang, L. Z. *et al.* Dynamic Imaging of RNA in Living Cells by CRISPR-Cas13 Systems. *Molecular Cell* **76,** 981–997.e7 (6 Dec. 2019).

130. Davis, B. J. & O'Connell, M. R. Put on Your Para-spectacles: The Development of Optimized CRISPR-Cas13-Based Approaches to Image RNA Dynamics in Real Time. *Molecular Cell* **77,** 207–209 (2 Jan. 2020).

131. Proshkin, S., Rahmouni, A. R., Mironov, A. & Nudler, E. Cooperation Between Translating Ribosomes and RNA Polymerase in Transcription Elongation. *Science* **328,** 504–508 (5977 Apr. 2010).

132. Bakshi, S., Siryaporn, A., Goulian, M. & Weisshaar, J. C. Superresolution imaging of ribosomes and RNA polymerase in live Escherichia coli cells. *Molecular Microbiology* **85,** 21–38 (1 2012).

133. Sanamrad, A. *et al.* Single-particle tracking reveals that free ribosomal subunits are not excluded from the Escherichia coli nucleoid. *Proceedings of the National Academy of Sciences* **111,** 11413–11418 (31 Aug. 2014).

134. Blundell, M. R. & Wild, D. G. Altered ribosomes after inhibition of Escherichia coli by rifampicin. *Biochemical Journal* **121,** 391–398 (3 Feb. 1971).

135. Farrar, A. *et al.* Ribosome Phenotypes Enable Rapid Antibiotic Susceptibility Testing in Escherichia coli. *medRxiv,* 2024.06.18.24309111 (June 2024).

136. DeLong, E. F., Wickham, G. S. & Pace, N. R. Phylogenetic Stains: Ribosomal RNA-Based Probes for the Identification of Single Cells. *Science* **243,** 1360–1363 (4896 Mar. 1989).

137. Amann, R. I., Krumholz, L. & Stahl, D. A. Fluorescent-oligonucleotide probing of whole cells for determinative, phylogenetic, and environmental studies in microbiology. *Journal of bacteriology* **172,** 762–770 (2 1990).

138. Amann, R. I. In situ identification of micro-organisms by whole cell hybridization with rRNA-targeted nucleic acid probes. *Molecular Microbial Ecology Manual,* 331–345 (1995).

139. Fuchs, B. M. *et al.* Flow cytometric analysis of the in situ accessibility of Escherichia coli 16S rRNA for fluorescently labeled oligonucleotide probes. *Applied and Environmental Microbiology* **64,** 4973–4982 (12 1998).

140. Chatzimichail, S. *et al.* Rapid Identification of Bacterial isolates Using Microfluidic Adaptive Channels and Multiplexed Fluorescence Microscopy. *Lab on a Chip* **17** (2024).

141. Bakshi, S., Choi, H., Mondal, J. & Weisshaar, J. C. Time-dependent effects of transcription- and translation-halting drugs on the spatial distributions of the Escherichia coli chromosome and ribosomes. *Molecular microbiology* **94,** 871–887 (4 Nov. 2014).

142. Bakshi, S., Choi, H. & Weisshaar, J. C. The spatial biology of transcription and translation in rapidly growing Escherichia coli. *Frontiers in Microbiology* **6,** 636 (2015).

143. Farrar, A. *et al.* Infection Inspection: using the power of citizen science for image-based prediction of antibiotic resistance in Escherichia coli treated with ciprofloxacin. *Scientific Reports 2024 14:1* **14,** 1–14 (1 Aug. 2024).

144. Plochowietz, A., Crawford, R. & Kapanidis, A. N. Characterization of organic fluorophores for in vivo FRET studies based on electroporated molecules. *Physical chemistry chemical physics : PCCP* **16,** 12688–12694 (2014).

145. Plochowietz, A., Farrell, I., Smilansky, Z., Cooperman, B. S. & Kapanidis, A. N. In vivo single-RNA tracking shows that most tRNA diffuses freely in live bacteria. *Nucleic acids research,* under review (2015).

146. Crawford, R., Kelly, D. J. & Kapanidis, A. N. A protein biosensor that relies on bending of single DNA molecules. *ChemPhysChem* **13** (4 2012).

147. Crawford, R. *et al.* Long-lived intracellular single-molecule fluorescence using electroporated molecules. *Biophysical Journal* **105,** 2439–2450 (11 2013).

148. Plochowietz, A., Farrell, I., Smilansky, Z., Cooperman, B. S. & Kapanidis, A. N. In vivo single-RNA tracking shows that most tRNA diffuses freely in live bacteria. *Nucleic acids research* **45,** 926–937 (2017).

149. Bakshi, S. *et al.* Nonperturbative imaging of nucleoid morphology in live bacterial cells during an antimicrobial peptide attack. *Applied and Environmental Microbiology* **80,** 4977–4986 (16 2014).

150. Kapanidis, A. N. *et al.* Retention of transcription initiation factor σ70 in transcription elongation: Single-molecule analysis. *Molecular Cell* **20.** Reference for RPo formation protocol, 347–356 (3 Nov. 2005).

151. Kapanidis, A. N. *et al.* Initial transcription by RNA polymerase proceeds through a DNA-scrunching mechanism. *Science* **314,** 1144–1147 (5802 Nov. 2006).

152. Robb, N. C. *et al.* The transcription bubble of the RNA polymerase-promoter open complex exhibits conformational heterogeneity and millisecond-scale dynamics: Implications for transcription start-site selection. *Journal of Molecular Biology* **425,** 875–885 (5 Mar. 2013).

153. Cordes, T. *et al.* Sensing DNA opening in transcription using quenchable Förster resonance energy transfer. *Biochemistry* **49,** 9171–9180 (43 Nov. 2010).

154. Duchi, D. *et al.* RNA Polymerase Pausing during Initial Transcription. *Molecular Cell* **63,** 939–950 (6 2016).

155. Dulin, D. *et al.* Pausing controls branching between productive and non-productive pathways during initial transcription in bacteria. *Nature Communications* **9,** 1–12 (1 2018).

156. Mazumder, A., Lin, M., Kapanidis, A. N. & Ebright, R. H. Closing and opening of the RNA polymerase trigger loop. *Proceedings of the National Academy of Sciences* **117,** 15642–15649 (27 2020).

157. Duchi, D., Mazumder, A., Malinen, A. M., Ebright, R. H. & Kapanidis, A. N. The RNA polymerase clamp interconverts dynamically among three states and is stabilized in a partly closed state by ppGpp. *Nucleic Acids Research* **46,** 7284–7295 (14 2018).

158. Liu, B., Baskin, R. J. & Kowalczykowski, S. C. DNA unwinding heterogeneity by RecBCD results from static molecules able to equilibrate. *Nature* **500,** 482–485 (7463 2013).

159. Golding, I., Paulsson, J., Zawilski, S. M. & Cox, E. C. Real-time kinetics of gene activity in individual bacteria. *Cell* **123,** 1025–1036 (6 2005).

160. Jones, D. L., Brewster, R. C. & Phillips, R. Promoter architecture dictates cell-to-cell variability in gene expression. *Science* **346,** 1533–1536 (2014).

161. Chong, S., Chen, C., Ge, H. & Xie, X. S. Mechanism of transcriptional bursting in bacteria. *Cell* **158,** 314–326 (2 July 2014).

162. Stracy, M. *et al.* Live-cell superresolution microscopy reveals the organization of RNA polymerase in the bacterial nucleoid. *Proceedings of the National Academy of Sciences* **112,** E4390–E4399 (2015).

163. Benatto, L. *et al.* FRET–Calc: A free software and web server for Förster Resonance Energy Transfer Calculation. *Computer Physics Communications* **287,** 108715 (June 2023).

164. Etheridge, T. J., Carr, A. M. & Herbert, A. D. GDSC SMLM: Single-molecule localisation microscopy software for ImageJ. *Wellcome Open Research* **7,** 241 (Sept. 2022).

165. Ma, H., Chen, M., Nguyen, P. & Liu, Y. Toward drift-free high-throughput nanoscopy through adaptive intersection maximization. *Science Advances* **10** (21 May 2024).

166. Wang, Y., Gu, Y. & Shun, J. *Theoretically-Efficient and Practical Parallel DBSCAN* in *Proceedings of the 2020 ACM SIGMOD International Conference on Management of Data* **12** (ACM, June 2020), 2555–2571.

167. Verwer, B. *Improved metrics in image processing applied to the Hilditch skeleton* in *[1988 Proceedings] 9th International Conference on Pattern Recognition* (IEEE Comput. Soc. Press, 1998), 137–142.

168. Schindelin, J. *et al.* Fiji: an open-source platform for biological-image analysis. *Nature methods* **9,** 676–682 (7 July 2012).

169. Holden, S. J. *et al.* Defining the limits of single-molecule FRET resolution in TIRF microscopy. *Biophysical journal* **99,** 3102–3111 (9 Nov. 2010).

170. Uphoff, S. *et al.* Monitoring multiple distances within a single molecule using switchable FRET. *Nature Methods* **7,** 831–836 (10 Oct. 2010).

171. Van de Meent, J.-W., Bronson, J. E., Wiggins, C. H. & Gonzalez, R. L. Empirical Bayes Methods Enable Advanced Population-Level Analyses of Single-Molecule FRET Experiments. *Biophysical Journal* **106,** 1327–1337 (6 Mar. 2014).

List of Figures